COAXIAL PLASMONIC METAMATERIALS FOR VISIBLE LIGHT

Cover image: Science is like a mountain hike. When looking back on the mountain road, you realize how much effort was taken to get to this point. But also, it makes you realize the beauty of the hike itself. The road was made out of SEM images of three different stages of the fabrication process.

Ph.D. Thesis University of Amsterdam, January 2016
Coaxial plasmonic metamaterials for visible light
Marie Anne van de Haar

ISBN 978-90-77209-99-8

A digital version of this thesis can be downloaded from http://www.amolf.nl.

COAXIAL PLASMONIC METAMATERIALS FOR VISIBLE LIGHT

Coaxiale plasmonische metamaterialen voor zichtbaar licht

ACADEMISCH PROEFSCHRIFT

ter verkrijging van de graad van doctor
aan de Universiteit van Amsterdam
op gezag van de Rector Magnificus
prof. dr. D.C. van den Boom
ten overstaan van een door het college voor promoties
ingestelde commissie,
in het openbaar te verdedigen in de Agnietenkapel
op dinsdag 26 januari 2016 te 10:00 uur

door

Marie Anne van de Haar

geboren te Amsterdam

Promotiecommissie

Promotor:

Prof. dr. A. Polman	Universiteit van Amsterdam

Overige leden:

Prof. dr. A. Meijerink	Universiteit Utrecht
Prof. dr. J. Gómez Rivas	Technische Universiteit Eindhoven
Prof. dr. H. B. van Linden van den Heuvell	Universiteit van Amsterdam
Prof. dr. T. Gregorkiewicz	Universiteit van Amsterdam
Dr. K. Dohnalova	Universiteit van Amsterdam

Faculteit der Natuurwetenschappen, Wiskunde en Informatica

This work is part of the research program of the 'Stichting voor Fundamenteel Onderzoek der Materie' (FOM), which is financially supported by the 'Nederlandse organisatie voor Wetenschappelijk Onderzoek' (NWO). It is also funded by the European Research Council (ERC).

Contents

1

Introduction

Life as we know it would not be possible without light. Ever since the history of mankind began, people have been intrigued by the creation, and later on, manipulation of light. Already before the start of the first century people found out how to make simple lenses, which were mainly used to magnify small letters in a book or as primitive glasses. What started with simple improvements in daily life, extended soon in much more exotic and complex devices enabling the discovery of many phenomena which could have never been detected without the manipulation of light. It was the invention of the laser in 1960 [1] that boosted light research, leading to widely used applications in telecommunication, optical data storage and processors. Soon after this, the desire grew to observe and control light on the nanoscale, which would enable new possibilities such as imaging beyond the diffraction limit [2], the realization of small optical integrated circuits [3], light emitting diodes (LEDs) and high efficiency solar cells, to mention just a few examples.

The key towards controlling light inside a medium is harnessing of the refractive index n of the material, which describes how light interacts with a (bulk) material. Convential media have a positive value for the refractive index, which has the consequence that inside the medium light is always traveling slower than the speed of light in vacuum, and energy refracts in a positive direction at an interface between two materials, away from the surface normal. The refractive index of a material originates from the polarizability of the material, which describes the coupling strength of the electro-magnetic fields of light with the charge distribution of the atoms used to build the material. For visible wavelengths, λ =400–700 nm, the wavelength of light is much larger than the inter-atomic distances, which is typically several Angstroms. Because of this large length scale difference, a material is usually considered as a homogeneous slab with an effective refractive index.

The field of metamaterials explores the possibilities to build materials out of 'artificial atoms', which are sub-wavelength building blocks designed to have a particular electro-magnetic response. Proper design of these building blocks can lead to new effective material properties which are not found in naturally occurring materials. Because of the sub-wavelength size of the building blocks, metamaterials can still be effectively described as a bulk material with an effective refractive index. Interestingly, for metamaterials the index can be designed to have extreme values, like $n < 1$, in which case the wavelength of light is larger than in vacuum, including the special case of n approaching zero [4], where the wavelength inside the material diverges. Another interesting class of metamaterials are negative-index metamaterials, as already considered by Veselago in 1968 [5]. In such materials light refracts in 'the wrong' direction and phase fronts travel backwards inside the material. Negative index materials are predicted to find applications in polarization-independent flat lenses [6], novel (micro-)optical components, superradiant light sources, transformation optics, and optical cloaking [7, 8], to mention a few examples [9].

One important class of optical metamaterials is composed of noble-metal resonant structures with a magneto-electric response (e.g. split ring resonators), embedded in a dielectric material. The interplay between the magnetic and electric resonances can lead to an effective negative index. Negative refraction using such geometries was first experimentally demonstrated in the microwave spectral range [10], and more recently in the near-infrared [11, 12]. However, the realization of negative-index metamaterials in the ultraviolet and visible spectral range using this concept has proven impossible, because it requires scaling of the resonator geometry to dimensions that cannot reliably be reached using electron beam lithography techniques [13, 14]. Furthermore, these designs rely on localized resonances which strongly absorb light [15] and only show a negative index for a very narrow bandwidth.

To circumvent the fundamental fabrication and Ohmic dissipation problems associated with nano-resonator metamaterials operating in the UV/visible, a different approach is needed to control light on the nanoscale. The design discussed in this thesis is based on surface plasmon polaritons (SPPs), optical waves of coherent electron oscillations that travel along the interface between a dielectric and metal to which light can couple efficiently [16–23]. The mode index of the SPP can be designed by choosing the proper materials and system geometry. It can have values which are not found in naturally abundant bulk materials because part of the field of the SPPs overlaps with the metal regions, thereby interacting with the negative permittivity of the metal [24]. By creating SPP waveguides in a three-dimensional architecture a metamaterial can be realized in which the effective index is determined by the complex interplay of the plasmonic waveguide modes.

1.1 Single planar metal/dielectric interfaces

The simplest geometry in which an SPP can exist is a single planar metal/dielectric interface. The dispersion diagram of an SPP traveling on such an interface can be found by solving Maxwell's equations in each metal and dielectric slab separately and then connect the solutions by using continuity of the tangential $\vec{E}$ and normal $\vec{D}$ fields at the metal/dielectric interface as boundary conditions [25–28]. The result is given by

$$k_x = \frac{\omega}{c}\sqrt{\frac{\epsilon_m \epsilon_d}{\epsilon_m + \epsilon_d}}, \tag{1.1}$$

where k_x is the wavevector in the propagation direction of the SPP, ω the frequency, c the speed of light and $\epsilon_{m,d}$ the complex permittivities of the metal and dielectric material respectively. Because the solutions for k_x can be found in the absence of any incident field, SPP modes are the eigenmodes of a metal-dielectric interface in the case of a lossless system.

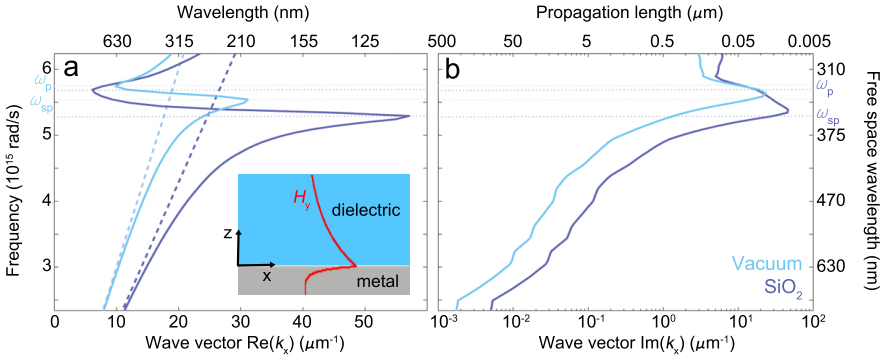

Figure 1.1: Dispersion diagram of a SPP traveling on a metal-dielectric interface. (a) Real and (b) imaginary part of k_x for a SPP on a single planar silver/air and silver/glass interface traveling in the x-direction. The light lines (dashed lines) of vacuum and glass are plotted as well. The inset shows the Re(H_y) dependence in the z-direction, perpendicular to the SPP propagation axis. The diagrams were calculated using experimentally measured values for the optical constants of silver.

The calculated dispersion diagrams for a SPP traveling on a planar silver/vacuum and a silver/silica interface are shown in Figure 1.1, together with the light line in glass and air ($k_x = \omega/(c\sqrt{\epsilon_d})$). We can distinguish three different regions in Figure 1.1(a): the bound mode, which is the region on the right side of the light line which asymptotes to the light line for small frequencies and to the surface plasmon resonant frequency ω_{sp} at large values of the wave vector. In this region the SPP wavelength is smaller than the corresponding free space wavelength. From this figure we observe that by approaching the surface plasmon

resonance frequency, the SPP mode index increasingly deviates from the free space wave vector indicated by the light line. However, the imaginary part of the wave vector, which indicates the energy losses, does increase significantly as well upon approaching the surface plasmon resonance.

The dispersion on the left side of the light line, above the bulk plasma frequency of the metal, is called the radiative mode, and asymptotes to the light line for large frequencies. Above the bulk plasma frequency the metal behaves as a dielectric causing the SPP mode to be not a truly bound eigenmode of the system in this region. The region in between the bound and the radiative mode is the quasi-bound mode. This region is also referred to as the stop gap, due to the absence of any modes in this region if the free electron gas model of Drude is used to describe the metal optical constants [27]. The inset in Figure 1.1 shows $\mathrm{Re}(H_y)$ near the metal/dielectric interface; it falls off exponentially in the direction transverse to the SPP propagation direction. In the example shown here, the field is mainly located in the dielectric, and only a small fraction is located in the metal.

Figure 1.1(a) shows that both the frequency and magnitude of the maximum wave vector are dependent on the used dielectric. The magnitude is determined by the losses in the metal which causes the dispersion diagram to bend back (the maximum wave vector goes to infinity in case of a lossless system) [29], and the SPP resonance frequency (ω_{sp}) is given by

$$\omega_{\mathrm{sp}} = \frac{\omega_{\mathrm{p}}}{\sqrt{1+\epsilon_{\mathrm{d}}}}, \tag{1.2}$$

with ω_{p} the bulk plasma frequency of the metal and ϵ_{d} the dielectric constant of the dielectric material. This equation shows that ω_{sp} can be tuned by the choice of metal and dielectric material.

The losses of the SPP in the direction of propagation determine the propagation length L_{SPP} of an SPP (where we only take into account dissipation losses, not the out coupling from the bound interface into free-space or other directions). L_{SPP} is defined as the distance which the SPP can travel until its intensity is decayed to $1/e$ of its original value and is given by

$$L_{\mathrm{SPP}} = \frac{1}{2\mathrm{Im}(k_x)}, \tag{1.3}$$

with $\mathrm{Im}(k_x)$ the imaginary part of the SPP wave vector in the direction of propagation. As seen in Figure 1.1(b), the SPP losses of the bound mode of a single dielectric/metal interface become significantly higher when approaching the surface plasmon resonance. The reason is that, in order to conserve momentum, k_x and k_z are connected through

$$\epsilon k_0 = k_x^2 + k_y^2 + k_z^2, \tag{1.4}$$

where ϵ is the dielectric constant of the bulk material, k_0 is the free space wave vector in vacuum and k_y is zero for an SPP traveling in the x-direction as in the geometry discussed in Figure 1.1. Then

$$k_{z(\mathrm{m,d})} = i\sqrt{k_x^2 - \frac{\omega^2}{c^2}\epsilon_{\mathrm{m,d}}} \tag{1.5}$$

follows, where m, d is the metal or dielectric, respectively. From Equation 1.5 it can be seen that an increase in k_x can only occur with an increase in k_z, and thus larger confinement in the z-direction [30]. The increase of the losses is the result of the fact that a larger fraction of the transverse field is located in the lossy metal.

1.2 Coupled SPPs in a planar metal-dielectric-metal geometry

The dispersion of SPPs can be controlled further by using geometries where different SPPs interact. In this section we will discuss the behavior of planar stacks of metal-dielectric-metal (MDM) layers in which the SPPs traveling on each metal-dielectric interface couple if the dielectric channel thickness is thin enough to get overlap of the fields of the different SPPs. This coupling gives rise to new modes: one which has a symmetric and one with an anti-symmetric mode profile of H_y and E_z in the transverse propagation direction [25, 28, 30], to which we will refer as the 'symmetric' and 'anti-symmetric' mode in the rest of this thesis.

Although the anti-symmetric mode can show very interesting dispersion behavior, such as a negative mode index, we will only discuss the symmetric mode in this section because this is the only propagating mode for the geometry and wavelength range discussed here [28].

The equations for the wave vector can be found using the same method as for a single metal/dielectric interface as discussed in Section 1.1. In this case, however, it is not possible to obtain a simple direct relation for k_x, but the dispersion for a three-layer MDM multilayer geometry with the structures centered at $z = 0$ and dielectric thickness t can be found by solving [28]

$$\epsilon_d k_{z,\mathrm{m}} + \epsilon_{\mathrm{m}} k_{z,\mathrm{d}} \coth\left(\frac{-i k_{z,\mathrm{d}} t}{2}\right) = 0 \tag{1.6}$$

with k_z following from momentum conservation (Equation 1.4):

$$k_{z(\mathrm{d,m})} = \epsilon_{\mathrm{d,m}}\left(\frac{\omega}{c}\right)^2 - k_x^2. \tag{1.7}$$

Equation 1.6 solves for the transverse magnetic (TM) mode with a symmetric field profile of H_y and E_z in the transverse direction as can be seen in the inset of Figure 1.2(a).

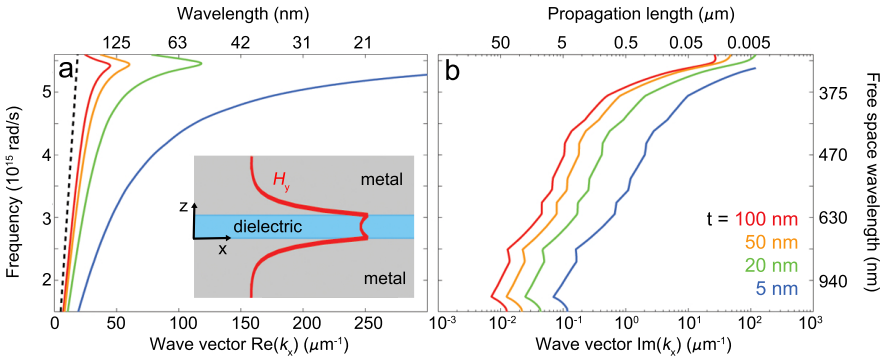

Figure 1.2: Dispersion diagram of a SPP traveling in a MDM structure. (a) Real and (b) imaginary part of k_x for silica waveguide channel thicknesses of 5, 20, 50 and 100 nm, surrounded by silver. The SPPs are traveling in the x-direction. The light line (black dashed line) of glass is plotted as well. The inset shows the H_y field in the z-direction, perpendicular to the SPP propagation direction. The diagrams were calculated using experimentally measured values for the optical constants of silver.

Figure 1.2 shows the dispersion diagrams of $Ag/SiO_2/Ag$ MDM waveguides with different dielectric thicknesses. Qualitatively, the same behavior is found for the symmetric mode as for the dispersion of a SPP traveling on a single metal-dielectric interface. However, with a MDM geometry much more extreme values of the wave vector are found, especially for small thicknesses of the dielectric channel. Although a higher value of the wave vector is accompanied by an increase of the losses, as for the single interface planar metal/dielectric structures, with the MDM waveguide geometry a more extreme mode index can be obtained with a larger propagation length. For example, a SPP with a $\mathrm{Re}(k_x)$ of 50 μm^{-1} has a propagation length of about 100 nm at a single Ag/SiO_2 interface, compared to 500 nm for a MDM geometry with a 20 nm channel. The reason is that for this MDM geometry the fields extend less into the lossy metal [28].

So far, we considered the optical behavior of SPPs traveling along the direction of the waveguides. However, these metal-dielectric building blocks can also be used to build three-dimensional metamaterials, in which light can propagate in al three directions. In order to do so the waveguides have to be stacked close enough to get coupling, and the coupling of adjacent waveguides needs to be designed carefully [31]. In this way a three-dimensional negative index of refraction can be realized for the transverse magnetic (TM) mode.

1.3 Coaxial plasmonic waveguides

A further advanced way to control the dispersion of SPPs is to fabricate coaxial MDM waveguides, in which the SPP dispersion is determined by the complex interaction of the electro-magnetic field in three dimensions. A sketch of an hexagonal array of coaxial MDM waveguides is shown in Figure 1.3, where dielectric coaxes are embedded in metal. In contrast to the planar waveguide geometry, the dispersion of a single coaxial waveguide is polarization independent for light incident from the top due to its cylindrical symmetry. Considering a cross-section of the proposed material along the coaxial channels (indicated as the xz and yz planes in Figure 1.3), it is clear that this material too consists of alternating layers of metal and dielectric material [32, 33].

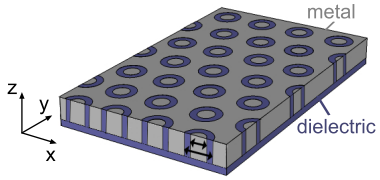

Figure 1.3: Sketch of the coaxial plasmonic metamaterial. The coaxial waveguides consist of thin (10–30 nm) cylindrical dielectric channels (purple) having a diameter of 150–200 nm embedded in metal (grey).

Like for the planar geometries, the dispersion diagrams can be calculated for individual cylindrical MDM structures, but now the equations need to be solved in cylindrical coordinates [32]. A double-periodic stacking needs to be taken into account since the SPPs on each interface can not only couple through the dielectric channel, but also through the metal core [31]. This double periodicity leads to a very interesting feature, namely that the mode which is anti-symmetric over the dielectric channel, can be designed to be the propagating mode for wavelengths above the plasmon resonance frequency [31]. This anti-symmetric mode can have very interesting dispersion properties, such as a negative index of refraction (see Chapter 3,4) and an index near zero [34].

The dispersion diagrams, together with a cross section of the mode profiles of the H_y fields in the transverse direction of both the symmetric and anti-symmetric modes in a single coaxial waveguide embedded in metal are shown in Figure 1.4. The symmetric, positive index, mode shows very large mode indices for frequencies below the plasmon resonance frequency. Above ω_{SP} the anti-symmetric mode shows lower losses than the symmetric mode, meaning that this is the dominant (propagating) mode in this frequency range. This anti-symmetric mode has a opposite sign of $\mathrm{Re}(k_z)$ and $\mathrm{Im}(k_z)$ in a frequency range for which the mode is dominant. Since an opposite sign of $\mathrm{Re}(k_z)$ and $\mathrm{Im}(k_z)$ is the requirement for a negative

mode index, it is noticed that the geometry in Figure 1.4 has a region where the dominant mode has a negative mode index.

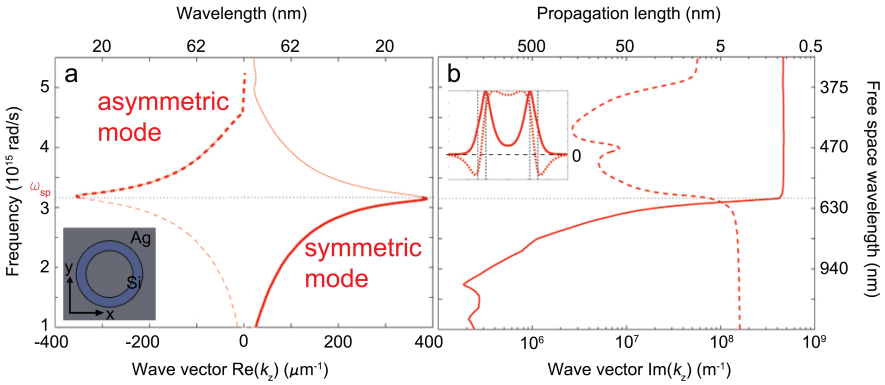

Figure 1.4: Dispersion diagram of a SPP traveling inside a single Ag/Si coaxial waveguide channel. (a) Real and (b) imaginary part of the SPP dispersion of a Si coaxial channel having an outer diameter of 150 nm and an inner diameter of 120 nm, embedded in silver. The solid lines represent the symmetric mode and the dashed lines the anti-symmetric mode, with the dominant regions denoted by a bold line. The inset in (a) shows a sketch of the top view of the considered coaxial geometry, the inset in (b) shows a cross section through the xy-plane of the H_y field through the center of the coaxial channel for the two modes.

The inset of Figure 1.4(b) shows the Re(H_y) fields inside the coax channel for a single, infinitely long coaxial channel for both the symmetric and anti-symmetric mode. We observe that the symmetric mode does not change sign across the coax channel, whereas the anti-symmetric mode does. The overall mode profile across both channels is symmetric for both modes.

A three-dimensional metamaterial can be built by careful designing an array of coaxial MDM building blocks [32, 33]. For this, it is important to design the ring-to-ring distance such that the coaxes are close enough to achieve coupling between the individual rings. Furthermore, the coupling of the individual coaxial waveguides gives an extra degree of freedom to control the dispersion of the metamaterial. In order to compare the performance of this plasmonic waveguide metamaterial to the geometries based on resonant antennas, we define a figure-of-merit (FOM) as $|\mathrm{Re}(n)/\mathrm{Im}(n)|$. A maximum FOM= 18 has been predicted for the negative-index mode of the plasmonic-waveguide based material [32], compared to FOM= 3 for negative-index split ring resonator based metamaterials [15].

1.4 Outline of this thesis

In this thesis we present the experimental realization of a three-dimensional coaxial, plasmonic metamaterial in the visible spectral range. The goal of this research is to successfully fabricate these metal/dielectric structures in order to get fundamental insight in the optical properties, supported by experiments. Furthermore, we use the plasmonic nanocoaxes as apertures to enhance optical trapping forces. The results of this research is presented in the following chapters.

Chapter 2 describes the many-step fabrication process of the coaxial metamaterial, consisting of Si or hydrogen silsesquioxane (HSQ) hollow cylinders with diameters down to 100 nm and channel thicknesses as small as 7 nm which are embedded in silver or gold. We present detailed description of all steps required for the fabrication process. We demonstrate the successful fabrication of these structures on a Si substrate, a 1 μm thick Si membrane and a SiO_2 substrate.

In Chapter 3 the optical properties of the plasmonic coaxial metamaterial are described in detail. We investigate the modal electric and magnetic fields and dispersion behavior of a single coaxial channel of different geometries and material choices. Furthermore, we study the coupling of coaxes arranged in a hexagonal array and investigate for which ring-to-ring distance interaction occurs. The Fabry-Pérot modes of a finite thickness slab are measured using cathodoluminescence spectroscopy, and explained by extracting the mode index from FDTD simulations.

In Chapter 4 we perform interferometry measurements in the visible spectral range to measure the mode indices of a Si/Ag plasmonic coaxial metamaterial. The data are consistent with a negative mode index in the range of λ =440–500 nm, and are in very good agreement with FDTD simulations. Furthermore, we experimentally demonstrate the polarization independence of the coaxial plasmonic metamaterial.

Chapter 5 describes how the exponentially decaying evanescent fields just outside the dielectric channels of coaxial plasmonic waveguides can be used to enhance optical trapping forces. The coaxial geometry has the capability to enhance the trapping force, and geometrically confines the optical force field. We perform FDTD simulations to calculate the trapping force for different coax dimensions and show atomic force measurements (AFM) of the optical force experienced by an AFM tip using HSQ/Au coaxial geometries.

In Chapter 6 we investigate the geometrical resonances in hollow Si cylinders. We show both numerically and experimentally that the magnetic dipole (MD) mode supported by high-index sub-wavelength scatterers is conserved inside cylinders with an air gap in the center. These MD modes are characterized by a displacement current loop which induces a high magnetic field intensity in the center of the gap. Furthermore, the trends upon changing the particle dimensions are investigated, paving the road towards experiments where a MD transition in a luminescent material inside the scatterer can be controlled by the cavity.

Overall, this thesis describes the fabrication process and optical properties of a three-dimensional coaxial plasmonic metamaterial. The coupling of alternating layers of metal and dielectric materials can lead to effective optical properties which are not found in natural materials. We experimentally demonstrate a negative mode index in the visible region using phase-sensitive measurements. The coaxial structures are used to enhance and spatially confine optical forces in the near field of the waveguides. Furthermore, the resonant behavior of hollow dielectric cylinders is described.

2

Fabrication process of a coaxial plasmonic metamaterial

We report, in full detail, the experimental fabrication process of a coaxial plasmonic metamaterial operating in the UV/visible part of the spectrum. This metamaterial is predicted to exhibit an effective negative index in the blue/UV spectral range or can be designed to optically trap sub-10-nm dielectric particles. The metamaterial consists of ultra-thin wall (13–15 nm) dielectric (Si or HSQ) coaxial cylinders with a well defined diameter (> 100 nm) embedded in silver or gold. We demonstrate the fabrication process on both a SiO_2 and Si substrate, where fabrication on a 1 μm thick Si membrane results in nearly freestanding structures. The process starts with creating an HSQ etch mask, using electron beam lithography. The structures are then transferred into the substrate with reactive ion etching, followed by metal infilling using a newly developed physical vapor deposition technique. Finally, the metamaterial surface is polished and made optically accessible with focused ion beam milling under grazing angles.

2.1 Introduction

Optical metamaterials are artificial materials composed of sub-wavelength building blocks which can be engineered to have optical properties which are

not found in nature, such as a negative index of refraction [5, 31] or an index near zero [4]. An important class of optical metamaterials is composed of sub-wavelength metal resonant structures with a magneto-electric response (e.g. split ring resonators), embedded in a dielectric material. These resonant-based metamaterials have been demonstrated experimentally in the infra-red and longer wavelength regime [10–12]. However, realizing these antenna-based metamaterials for shorter wavelengths has proven to be very difficult because the resonator size scales with the operating wavelength [13]. These fabrication difficulties, together with the narrow bandwidth and relatively high losses at the resonance frequency [15] can be circumvented by using plasmonic metamaterials. This class of metamaterials does not rely on localized resonances, but are built up from alternating metal/dielectric layers that support surface plasmon polaritons (SPPs) [35]. Properly designing the SPP coupling traveling on the metal/dielectric interfaces by tuning the dimensions of these metal/dielectric stacks can, as in case for the resonance-based metamaterials, also result in special optical properties as negative and near-zero refractive index [4, 31]. However, these planar geometries only work for TM polarized light and are thus highly polarization dependent.

Here, we present the fabrication process of a polarization independent geometry, consisting of hollow Si or hydrogen silsesquioxane (HSQ) cylinders embedded in metal. In order to obtain successful coupling of the SPPs on each metal/dielectric interface we need to realize extremely thin cylinder sidewalls, in the order of 15–30 nm and an outer diameter in the order of 100–180 nm. We show the succesful fabrication process of Si coaxes on a Si chip, almost freestanding structures on 1 μm thick membranes as well as the fabrication of HSQ coaxes, which has a refractive index very similar to glass [36], on a SiO_2 substrate. The silicon structures were infilled with Ag, the HSQ on glass samples both with Ag and Au.

Figure 2.1 shows a sketch of the total fabrication process. We start with electron beam lithography (EBL) using the negative high-resolution resist HSQ. The HSQ patterns can be used as etch mask to transfer the structures into the substrate using reactive ion etching (RIE). Next, we infill the structures with metal using a newly developed electron beam physical vapor deposition (EBPVD) method followed by a polishing step with a focused ion beam (FIB) to smoothen the surface and make the coaxes optically accessible. Each of these steps will be explained in detail in the next sections of this chapter.

2.1.1 Resolution in electron beam lithography

In order to obtain feature sizes as small as 10 nm, we need a very high resolution in the EBL process. The resolution of the EBL process is determined by the properties of the used resist, the lithographic system and processing conditions. An important aspect which limits the resolution is the scattering of electrons in the resist itself and the substrate underneath the resist. There are two types of elastic scattering: forward and back-scattering. Forward scattering is the small-angle deflection of

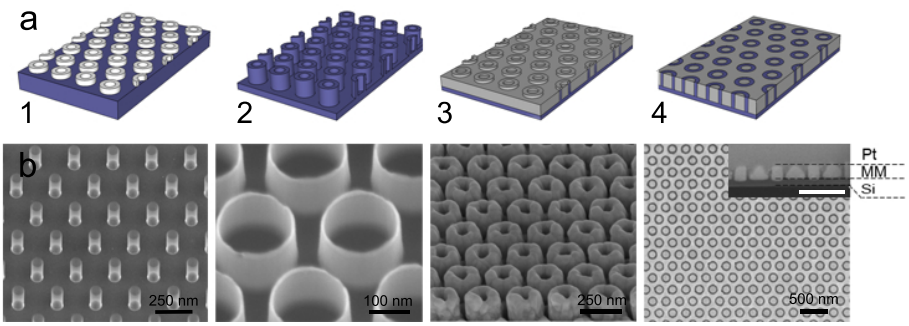

Figure 2.1: Fabrication process of the coaxial metamaterial. (a) Sketch and (b) SEM images of the individual steps: 1. EBL on Si, Si membrane or SiO_2 substrate, 2. RIE etching to transfer the structures into the substrate, 3. Metal deposition using a newly developed EBPVD method, and 4. Polishing the surface with the FIB under grazing incidence.

electrons that enter the resist. This leads to an overall increase of the beam diameter, resulting in the exposure of a larger area in the resist. This effect can be reduced by using thinner resist films, a resist with small atomic weights, or increasing the beam energy. In back-scattering the electrons are deflected at large angles, where areas far from the incoming beam can be exposed. This effect occurs mostly in the substrate. This phenomenon is also known as the proximity effect, which is especially a problem for dense arrays where certain areas of a resist receive a larger dose than intended due to backscattered electrons from neighboring areas. Back-scattering can be reduced by using a very thin substrate or a substrate with a low atomic weight, or using electrons with lower energy.

Since the majority of the resist is transformed by secondary electrons rather than the direct electron beam, it is important to consider these electrons as well in order to determine the optimal resolution of the EBL process. Secondary electrons originate from inelastic collisions with the electrons in the molecules of the resist or substrate and lead to an effective widening of the beam diameter. Secondary electrons do not contribute to the proximity effect since their range in the resist is only a few nanometers.

Interestingly, both increasing and decreasing the electron voltage can result in a higher resolution. As the electron energy is increased, less forward scattering results in more vertical wall profiles and thus better resolution. However, higher electron energy also results in more back-scattering which increases the proximity effect. For thin or low atomic weight resists and substrates, a high electron energy (>20 keV) will generally lead to the highest resolution. Using low energy electrons (<5 keV) can also result in higher resolution since the generation rate of back-scattered electrons is decreased [37]. Here, we use a 30 or 100 keV electron beam, where 100 keV results in the highest resolution EBL process.

High resolution resists typically have a small molecule size, small atomic weight and require a relatively high exposure dose (low sensitivity). The smaller size of the molecules allows cross-linking or chain scission to happen at a smaller scale, while the low atomic weight reduces the electron scattering in the resist. The lower sensitivity typically leads to less proximity effects, which increases the resolution especially for dense arrays. However, a lower sensitivity requires a larger exposure dose, which results in a more time consuming process.

The sensitivity of the resist depends on several factors. In general, a larger molecule requires a smaller exposure dose since it has a larger cross section and hence a higher probability of electron interaction. The sensitivity is also affected by the electron energy, where the sensitivity is increased for lower energy electrons (as long as the electron energy is still large enough such that the electrons can travel to the bottom of the resist layer). This is due to an increased probability of the electrons to interact with the resist rather than the underlying substrate. On the other hand, using a low atomic weight or thin membrane substrate results in a higher required dose due to the decreased generation rate of back-scattered electrons.

The inorganic negative high resolution resist hydrogen silsesquioxane (HSQ), meets the requirement of consisting of relatively small molecules. It requires a relatively high exposure dose compared to most (organic) resists and has a high etch resistance which is needed to transfer the patterns into the Si substrate [38]. HSQ consists of cubical-shaped molecules with the chemical formula $H_8Si_8O_{12}$. The Si atoms are positioned at each cubic corner, with the corners being linked via oxygen atoms. The hydrogen atoms are attached on the other sides of the Si atoms (Figure 2.2). The cages open and form into a linear network under influence of the electron beam.

A disadvantage of HSQ is its low contrast, defined as the sharpness of the transition between exposed and unexposed, as a function of electron dose. The contrast of HSQ can be changed by adjusting the development and baking procedure [38, 40–44]. This tunability is convenient, but it also reflects the extreme sensitivity of HSQ to environmental changes and pollution. A change of just 1 °C in the developing temperature leads to a variation of 11% in contrast, 5% in the saturation and 49% in the on-set dose [42]. Exposure to air for only 1 hour can increase the feature size by 66% [45].

2.1.2 Reactive ion etching

For the fabrication of coaxial Si cylinders, the HSQ pattern is transferred into the substrate using RIE. RIE is a dry-etching technique which is based on two principles: plasma, or radical, etching and physical sputtering of the substrate with ions provided by the plasma. The first is characterized by minimal ion bombardment and purely chemical etching, leading to very selective and fast, but isotropic etches. This process is usually dominant for very low bias and high gas pressure. However,

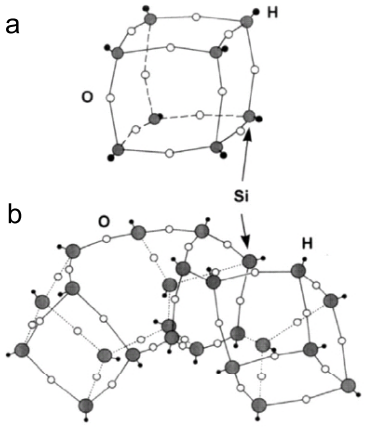

Figure 2.2: Schematic representation of the molecular structure of HSQ. (a) Cage-like structure before exposure, which appear as (b) partly formed cages of various sizes in solution. Image taken from Ref [39].

for many substrate materials there is no chemical etchant available. In these cases the sample can be etched using sputtering with a directed ion flow. The latter technique is usually very slow (1–30 nm/min), but can also be very anisotropic and is in principle applicable to any substrate. By combining both techniques by adding a few well-chosen reactive chemicals to the etch mixture while using a relatively large bias and/or low density, the etch rate, selectivity and isotropy of the etch can be controlled.

Although there are some general guidelines for the etching behavior, it is important to keep in mind that the interplay between chemical etching and physical sputtering of the substrate is very complex and not straightforward. To mention an example, the etch rate of Si exposed to both XeF_2 and Ar^+ ions is much greater than the sum of the etch rates for exposure to the Ar_2 and XeF_2 separately [46]. The reason is that the reactive XeF_2 does not only enhance the etch rate by reacting with the substrate to form volatile molecules, but adding Ar^+ ions also modifies the surface reactions in such a way that radicals can react stronger with the substrate. Adding reactive chemicals to the etching mixture can not only enhance the etch rate but can also inhibit the etching by forming a passivation layer with a high etch resistance. This technique is often used in etch mixtures containing both ions and reactive chemicals to make the etch more directional. Sidewalls that are not exposed to the ions are then covered by the resistive layer, while normal to the ion path this layer will be removed by ion bombardment.

Clearly, in order to develop an etch recipe we have several parameters to optimize, which have a complex interplay with each other [47, 48]. It is not straightforward to predict a priori which chemicals should be used in which (relative) con-

centrations and how changing the chemicals influences the etch rate, anisotropy and selectivity. However there are some general guidelines that can be used when developing an etch recipe. Increasing the radio frequency (RF) power generally leads to more sputtering and a higher etch rate, while increasing the inductively coupled plasma (ICP) power generally leads to more lateral etching and thus less anisotropy. Lastly, increasing the temperature promotes chemical reactions, but can also increase lateral etching because surface radicals become more mobile. Using cryogenic temperatures can enhance the forming of a passivation layer because the low temperature prevents compounds from escaping the surface.

For our fabrication process there are two main criteria which determine the succes of the etch recipe: selectivity and anisotropy. Due to the very thin side walls, our structures are very sensitive to slightly isotropic etching which results in holes in the side walls and collapsing of the rings. Therefore we cannot compromise on the anisotropy of the etch, which for most etch recipes results in a limited maximum height of the Si coaxes. To fabricate larger aspect ratios while maintaining the anisotropy, one could either use a thicker HSQ mask or switch to different etching chemicals. However, increasing the resist thickness will decrease the resolution of the EBL process, resulting in thicker side walls (Section 2.1.1).

In this chapter, we develop two anisotropic etch recipes which successfully transfer HSQ cylinders into the Si substrate. The first is based on CHF_3 and SF_6, the second on HBr. For both etch recipes we use a low pressure recipe and relatively high ion energies, such that the lateral movement of the ions is minimized.

2.2 Electron beam lithography using HSQ

2.2.1 Method

The first step in the many-step fabrication process is patterning the substrates with hollow cylinders of the negative high resolution resist HSQ. The metamaterial was fabricated on three different kinds of substrates: SiO_2 slides (1 mm thick borosilicate glass slides from Menzel), 500–550 μm thick Si(100) chips (WRS Materials) and 1 μm thick 1.3×1.3 μm^2 Si(100) membranes supported by a 300 μm thick 10×10 mm^2 Si frame (Norcada). Before the fabrication is started, the samples are first base-piranha cleaned (5:1:1 solution of dH_2O:NH_2OH:H_2O_2) at 75 °C for about 20 minutes. The samples are rinsed in demi-water and blow-dried with N_2. The silicon membranes were used fresh from the packaging without any cleaning. Before spin coating, all substrates were baked for 5 minutes at 200 °C to completely dry the surface. To be able to spin coat the membranes, we stuck them on top of a Si chip using copper tape or a thin layer of acetone dissoluble glue. After baking, the samples are cooled to room temperature with a N_2-flow for about 10 s. Then the samples were immediately spin coated with, depending on the desired resist thickness, (dilutions of) HSQ Fox-12, FOx-14 or FOx-15 (Dow Corning) for 45 seconds at 2000 rpm, with a closed lid. If thin resist layers were desired, the

standard HSQ solutions were diluted with MIBK. To obtain a higher resolution the samples were baked at 90 °C for 45 minutes, instead of the typical two-step baking procedure of 120 s at 150 °C followed by 120 s at 220 °C [43]. Baking at lower temperatures increases the resolution, but decreases the sensitivity, meaning that a higher dose is needed when exposing the HSQ to the electron beam [44]. In case of the SiO_2 substrates the samples were made conductive by spin coating a thin layer of an aqueous solution with a conducting polymer (Espacer 300Z, Showa Denko) for 45 s at 3000 rpm with a closed lit. After spin coating the samples were dried at room temperature for 2 minutes before a 5 minutes bake at 180 °C. The HSQ layer thickness was measured by scratching the sample and using a height profilometer. The resist thickness was typically 200 nm (using undiluted HSQ FOX-14 or FOX-15), but could be varied between 50–500 nm depending on the HSQ concentration and age, type and treatment of substrate and spinning conditions.

Depending on the desired resolution, either a 30 keV beam, using a Raith e-LINE EBL system, or a 100 keV from a Vistec EBPG5000Plus HR 100 system with a small aperture was used to write rings into the HSQ. Because the sensitivity of HSQ is very dependent on the exact spinning, storing and baking conditions (e.g. thickness of the resist, baking temperature and time [44], substrate, writing voltage, age of the HSQ, time between spin coating and baking, time between baking and writing [41]) the optimum exposure dose varies between different samples. Typically, for a resist thickness of 200 nm and a 1 μm thick Si membrane substrate, we used ~300 $\mu C/cm^2$ for 30 keV EBL, and ~14000 $\mu C/cm^2$ for the 100 keV e-beam writing. In general, membrane samples require a higher dose compared to thicker substrates, due to the reduced amount of back-scattered electrons in case of thinner substrates. Also, thicker resist layers require a higher dose. Longer waiting times between spin coating and exposure or exposure and developing will both lead to lower writing doses (higher sensitivity) but slightly lower resolution due to partly cross-linking of HSQ over time [41].

After writing, the structures are developed in tetramethylammonium hydroxide (TMAH) for 1 minute at 50 °C, rinsed in dH_2O for 30 s and dipped into isopropanol (IPA). The samples were dried in a critical point dryer to prevent collapsing or displacement of the structures. For the non-membrane samples we used a 25% TMAH solution, for the membranes we diluted this to a 5% solution to improve the adhesion of the structures onto the substrate, however, this results in a slightly lower resolution. Developing at 50 °C instead of room temperature increases the resolution and decreases the feature roughness [42, 43]. In Figure 2.5 we show SEM images of developed HSQ coaxes on different substrates, where (a,b) show structures on a SiO_2 substrate and (c-f) shows the successful fabrication on a Si substrate. As shown in Figure 2.3, the described process results in very conformal fabrication of larger areas (typically 20×20 μm^2 fields were written, but in principle the field size is limited by the write field area for which no stage movement is needed, which is typically a few mm). In Figure 2.7(e,f) we show that it is possible to fabricate very high aspect ratio coaxes having a height of over 400 nm, with a diameter of 80 nm

and a wall thickness of about 20 nm.

2.2.2 Critical point dryer

As described in Section 2.2.1, all samples were dried in a critical point dryer after development. Figure 2.4 shows a patterned sample after development that was dried in air instead, i.e. without critical point dryer. In this case, coaxes with relatively low aspect ratio (having a height of typically <150 nm for >100 nm diameter rings) are displaced over the sample surface (Figure 2.4(a,b), whereas longer coaxes (with a height of typically >150 nm for <300 nm diameter rings) collapse and cluster together by the pressure of the liquid droplet. The interfacial tension between the liquid/air interface of the drying solvent droplet can be prevented by using a critical point dryer which replaces the solvent (usually isopropanol) with liquid CO_2, after which the pressure and temperature inside the sample chamber is increased to go to the critical point of CO_2. Then, the CO_2 is vented out of the chamber, resulting in drying the sample without any liquid/air interface. For this reason, all samples described in this thesis are dried after development using a critical point dryer. However, a critical point dryer is not necessary after the HF dip later on in the fabrication process. The reason is that the adhesion of the rings is much stronger during this drying process because the rings are etched into the Si before the HF dip, resulting in more rigid structures which are stably attached to the surface.

2.2.3 HSQ adhesion on Si membranes

For both the silicon and SiO_2 substrates the samples were developed in a 25% TMAH solution in water at 50 °C. As can been seen in Figure 2.5, this results in structures with extremely thin side walls (<10 nm), with good adhesion on both Si and SiO_2. Clearly, the minimum feature size is increased if the resist thickness is increased.

However, developing the Si membrane samples with this high concentration of TMAH causes adhesion problems, as shown in Figure 2.6(a,b). Due to bad adhesion of the HSQ after development, the individual rings are washed away and the over-exposed fields, where the individual rings are all merged together due to proximity effects, are displaced over the substrate after development. The over-exposed fields release from the substrate during imaging with a 5 keV beam, demonstrating the bad adhesion.

Clearly, a 25% TMAH solution is too aggressive on Si membranes. Several surface treatments, such as charging the surface with an RIE oxygen descum or thermal annealing before applying the HSQ did not improve the adhesion sufficiently. Figure 2.6(d,e) shows the effect of spincoating HDMS primer underneath the HSQ for 1 min. at 4000 rpm and baking at 180 °C before applying the HSQ. Although it does improve the adhesion somewhat, the rings are still displaced over the substrate. The adhesion problems can be solved by using a 5% TMAH solution instead

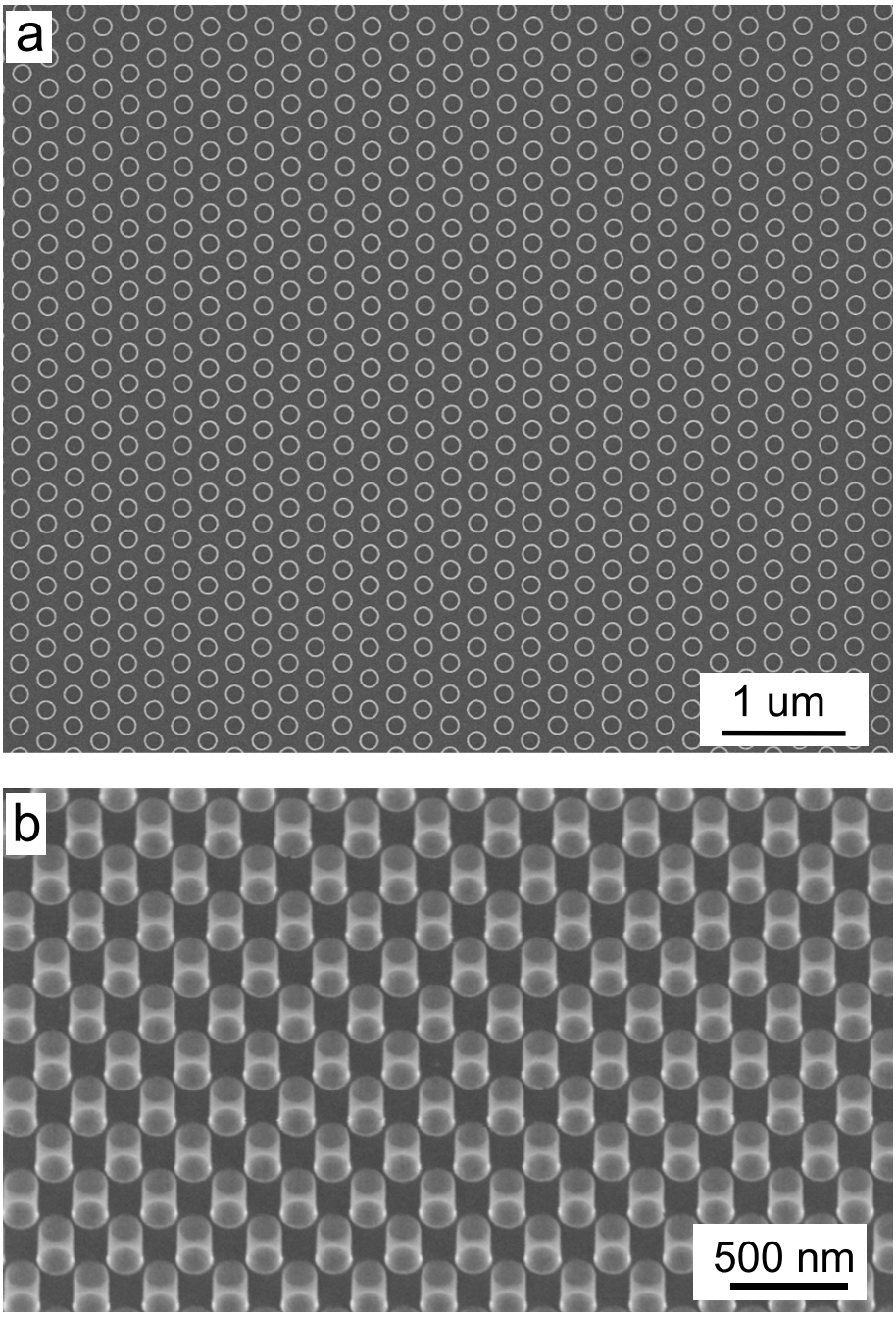

Figure 2.3: (a) Top and (b) tilted view of a hexagonal array of HSQ coaxes, having an outer diameter of 150 nm, a wall thickness of 5–10 nm and a height of 220 nm on a 1 μm thick Si membrane after exposure of a 100 keV electron beam and development in a 5% TMAH solution in water. SEM images are taken using a 5 keV electron beam.

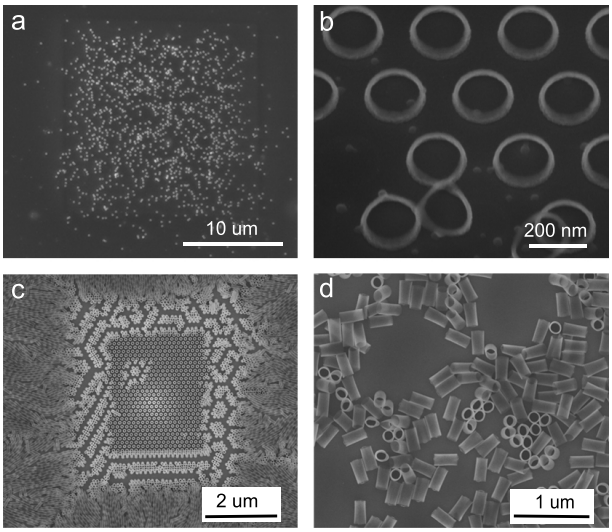

Figure 2.4: Examples of HSQ coaxes where the samples are dried in air after development instead of using the critical point dryer. Short coaxes (a,b) (typically <150 nm) are displaced over the sample, whereas long coaxes (c,d) (typically >150 nm) collapse and cluster together by the surface pressure of the drying liquid droplet. The HSQ coaxes in this Figure are 80 nm (a,b) and 335 nm (c,d) nm in height. All SEM images are taken using a 5 keV electron beam.

of the 25%. The result is shown in Figure 2.6(e,f). The resolution is slightly decreased by developing with lower concentrations, but this can be compensated by using 100 keV EBL instead of 30 keV. Figure 2.3 shows the result of HSQ coaxes on top of a 1 μm thick membrane after exposure with a 100 keV electron beam and development in 5% TMAH solution in water at 50°C. Using 100 keV EBL on 200–250 nm thick HSQ on a Si membrane results in a wall thickness as small as 10–15 nm is achieved. This resolution is similar to the results we obtained in Figure 2.5(b,c), where a 30 keV beam was used to write structures in a 50–80 nm thick HSQ layer on a thick Si substrate.

2.2.4 Limits of EBL using HSQ

The optimized procedure as discussed in Section 2.2.3, using 100 keV EBL, leads to HSQ rings with a wall thickness of 10 nm and a height up to 250 nm on a Si membrane. Figure 2.7 summarizes some other limiting factors that we found in writing HSQ rings on Si, Si membranes and SiO_2 substrates using thick HSQ layers of 200–250 nm.

Basically, there are no limits on the maximum ring diameter as long as they fit within one write field of the EBL system which is 2 mm for the Raith system used to

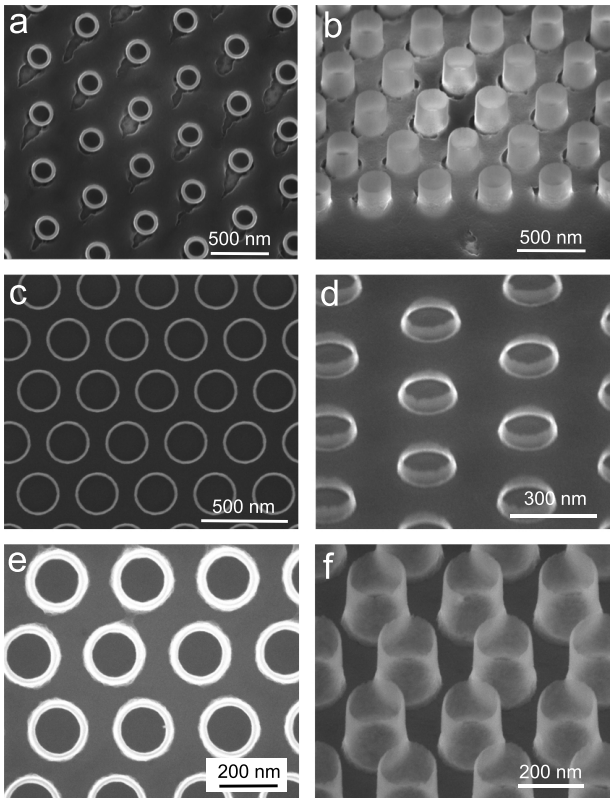

Figure 2.5: HSQ coaxes after exposure to a 30 keV electron beam and development in a 25% TMAH solution in water on a (a,b) SiO_2 and (c-f) Si substrate. (a,c,e) show a top view, whereas (b,d,f) show a tilted view. The structures in (c,d) are ~80nm in height, the structures in (b,f) are ~200 nm tall. SEM images are taken using a 5 keV electron beam.

write the 20 and 30 keV samples. We have successfully fabricated rings with a 1 μm diameter (Figure 2.7(a)). The minimum outer ring diameter is defined by proximity effects and the sensitivity and resolution of the resist, the first being determined by the voltage of the electron beam, the latter by the aging and handling of the HSQ before writing (see Section 2.1). We found a minimum outer diameter of 100 nm (see Figure 2.7(b)). Decreasing the diameter further results in solid rings where the gap in the center is completely filled.

Limitations in the closest ring-to-ring distance are also determined by proximity effects and sensitivity and resolution of the resist. We successfully fabricated a ring-to-ring distance of about 30 nm (Figure 2.7(c)). Decreasing this distance further results in bridges between the rings at their closest spacing position. (Fig-

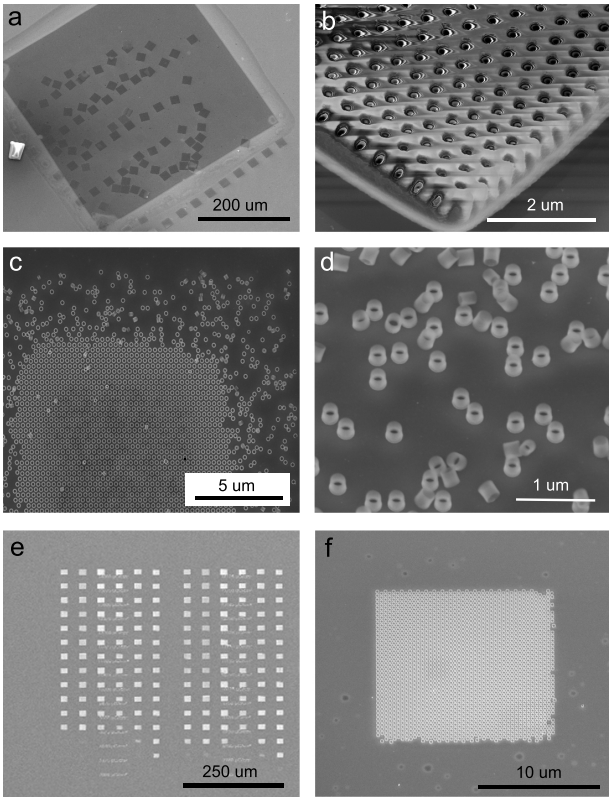

Figure 2.6: Adhesion problems of HSQ on Si membranes. (a-d) Development with 25% and (e,f) 5% TMAH solution in water at 50 °C. The darker area in (a) is a 500×500 μm Si membrane, surrounded by thick Si (lighter grey) to support the membrane. The smaller squares are 20×20 μm fields of exposed and developed HSQ. A zoom of one of these fields is shown in (b), where the bottom left corner is lifted from the substrate under influence of the electron beam during imaging with the SEM. In the experiments shown in (c,d) a HDMS primer was spincoated underneath the HSQ, where (c) shows an 20×20 μm field of exposed and developed HSQ rings, and (d) is a zoom where the individual rings can be seen. The squares in (e) are fields of exposed and developed HSQ rings developed using a 5% TMAH solution. In these fields the dose is increasing from top to bottom, while from left to right different geometries are written. A close up of a hexagonal array of coaxes is shown in (f). SEM images are taken using a 5 keV electron beam.

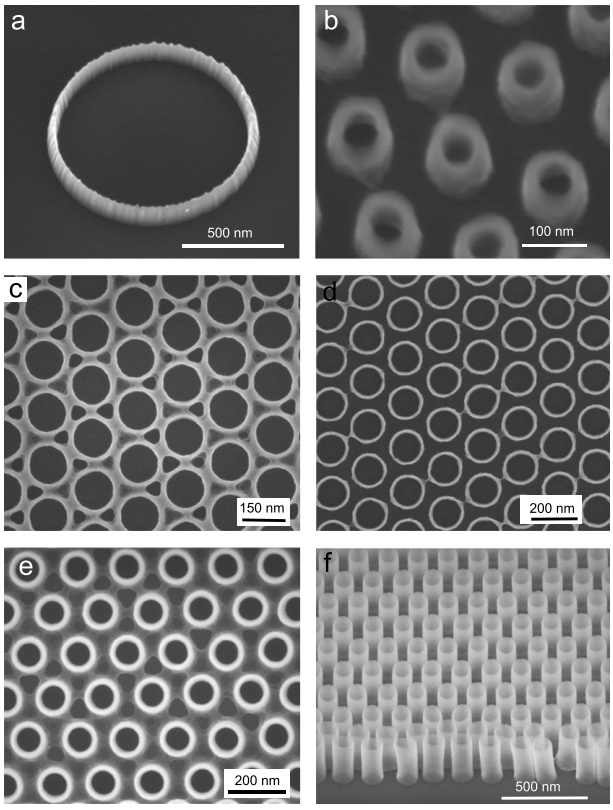

Figure 2.7: Limitations in resolution of EBL with HSQ. (a) There are basically no limits on the maximum diameter. This ring is 1 μm in diameter. (b) The minimum ring diameter is about 85 nm for 100 nm tall rings. Decreasing the radius further results in completely filled rings. (c) If the ring-to-ring distance is smaller than ~30 nm the coaxes start to merge. The ring-to-ring distance was designed here to be 20 nm. In (d) the ring-to-ring distance is 30 nm. (e,f) Top and tilted view of 410 nm tall coaxes on a Si membrane (100 keV). The ring diameter is 130 nm and the wall thickness is 16 nm. SEM images are taken using a 5 keV electron beam.

ure 2.7(d)).

The maximum height of the coaxes is not well defined, but a trade off between resolution and height. We fabricated 410 nm tall HSQ coaxes with a wall thickness of 16 nm.

2.3 Reactive ion etching

2.3.1 Reactive ion etching of Si using SF_6 and CHF_3

For the next step in the fabrication process of Si coaxes, the HSQ structures are used as etch mask to etch the Si substrate with a very anisotropic reactive ion etch. In this section we discuss the RIE etching of Si using SF_6 and CHF_3, which is a well known mixture to anisoptropically etch Si [49–51]. Both chemicals form radicals in the plasma (F^*, SF_5^* and CF_2^*) which can etch Si by forming the volatile products SiF_4, HF and SiF_4, or form the etching inhibitors $Si_xS_yF_z$ (only if cryogenic cooling is used) and $Si_xC_yF_6$, which protect the side walls of the structures during the etching process [52]. At room temperature SF_6 is used as etchant, whereas CHF_3 mainly acts as inhibitor to enhance the anisotropy by forming a polymer layer on the surfaces. The ion bombardment need to be optimized such, that it is efficient enough to be able to break through the protective layer on the substrate without damaging the polymer on the side walls of the structures. The relative efficiencies of the chemical etching, protecting and ion bombardment processes can be tuned by changing the plasma conditions, as explained in Section 2.1.2.

Small amounts of O_2 (<5%) in the plasma are known to increase the etch rate by reacting with CF_x^* radicals to form CO_2 and COF_2, which increases the reactive F-ion concentration [53]. We found that for our recipe the addition of O_2 also increases the Si:HSQ selectivity, which increases the maximum height of the Si structures that can be achieved. However, due to consumption of the CF_x^*, the formation of the protective polymer layer is suppressed which leads to a more isotropic etch. Increasing the O_2 concentration (>7.5%) results in the formation of an inorganic passivating $Si_xO_yF_z$ film on the surface. In this regime the etch rate is not longer determined by the concentration of the reactive F-ions, but is limited by the thickness of the passivation layer which needs to be etched through with ion bombardment in order to acces the Si surface [52]. In this regime the etch rate is highly dependent on the ion energy. Increasing the O_2 concentration even further (>15 %) results in dilution of the F-ion density and thus a lower etch rate. The anisotropy usually increases in the latter regime due to fast formation of the protective oxide layer but decreased side-wall attack from the F-ions [48].

As explained before, not only the pressure and the presence of O_2 determines the selectively and anisotropy of the etch. We observed that the CHF_3:SF_6 ratio turned out to be very critical as well, and can be tuned to make the etch recipe more selective for Si. However, we found that this, for all cases we tried, always results in a more anisotropic etch. The reason is that the highest selectivity can be reached if there is no protecting layer formed on the surface, increasing the Si etch rate (and thus the selectivity) and making it unnecessary to use high energy ions to remove this protective layer which also etches the SiO_x mask. Decreasing the bias generally also increases the selectivity since the etching of SiO_x is ion induced, and thus dependent on the bias. However, changing the bias will also change the Si and protective oxide layer etching, resulting in a change of anisotropy.

The optimum anisotropic etch recipe we found consists of 35 sccm CHF_3, 5 sccm SF_6, a pressure of 7 mTorr and 125 W forward power. This results in a DC-bias of about 400 V and an etch rate of ~18 nm/min. Because the plasma becomes more difficult to ignite with such low pressures and no ICP power, a strike pressure of 20 mTorr was used during the first 70 s of the etching procedure. In general, we found that a lower pressure results in more anisotropic etching, but using a too low pressure results in an unstable plasma.

Figure 2.8 shows the results of the RIE etching process after different etching times. It can clearly be observed that the etch depth into the Si increases, while the HSQ mask is decreasing in height if the etching time increases (Figure 2.8(a,b)). The disappearance of HSQ is a result of the limited selectively, which is about 1:1. Therefore the mask will be completely gone after a certain etching time (typically after 7–10 min. of etching, depending on the HSQ thickness). This is shown in Figure 2.8(c). With the 200–250 nm HSQ layers as described in Section 2.2, we typically obtain Si coaxes of 150–200 nm in height. Etching further when the HSQ mask has disappeared results in etching of the Si rings, resulting in crown-like structures as can be seen in Figure 2.8(d).

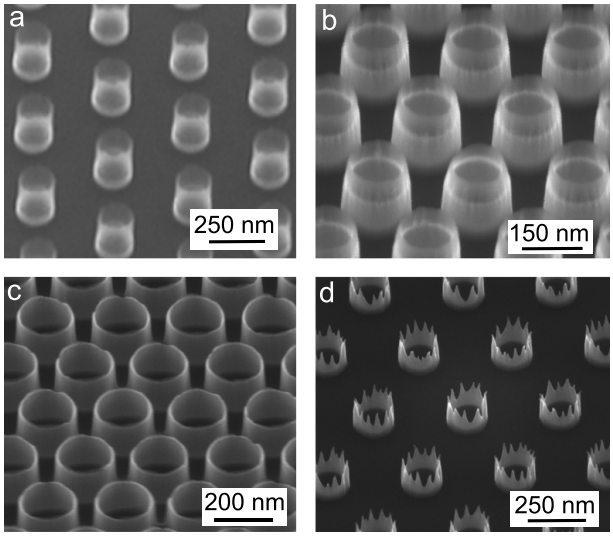

Figure 2.8: RIE using SF_6 and CHF_3 after different etching times. (a) After 1 minute etching time: very short rings of Si can be distinguished underneath the HSQ mask. (b) After 5 minutes etching time: the etch depth in Si is increased, while the HSQ mask thickness is decreasing. (c) After 8 minutes etching time: the Si coaxes are 150 nm tall, there is almost no HSQ left on top of the structures. (d) After 10 minutes etching time: the Si coaxes are transformed into crown-like structures and there is no HSQ left on top of the structures. SEM images are taken using a 5 keV electron beam.

The etch is usually stopped before all the HSQ has disappeared to prevent the crown-like structures as shown in Figure 2.8(d). This has the consequence that there is still a thin remaining layer of HSQ on top of the Si structures. To remove these remainders of the resist, the RIE was followed by a 1% HF dip of 10 minutes. Figure 2.9 shows SEM images of the structures after the HF dip. After etching, the coaxes have a wall thickness of 20–30 nm, depending on the wall thickness of the HSQ mask, as shown in Figure 2.9(a,b). Figure 2.9(c) shows that the etch is very uniform over larger areas. Typically we etch fields of 20×20 μm.

Although the minimum wall thickness obtained with the above described procedure is about 20 nm, it can be decreased further by thermally oxidizing the samples at 950 °C for a short time (1–3 minutes) in the presence of an O_2 flow of 1 L/min. After the oxidation the oxide is removed with an HF dip. Using this method, we obtained rings of about 6 nm in thickness, as shown in Figure 2.10.

2.3.2 Reactive ion etching of Si using HBr

Although we obtained very smooth and anisotropic results with SF_6 and CHF_3 RIE etching, the maximum etch heights are limited due to the limited etch selectivity for HSQ. To increase the maximum etch depth in Si, we explored etch recipes using HBr, which is known to selectively and very anisotropically etch Si [54, 55]. The Si reaction rate with HBr to form the volatile $SiBr_4$ and H_2 is very small compared to other Si etchants [56], which implies that ion bombardment is necessary to obtain acceptable etch rates. The low reaction rate results in almost no side-wall etching and thus no undercutting, allowing highly anisotropic profiles to be etched without protecting the sidewalls with a passivant [57].

Because ion bombardment plays a major role in HBr etching of Si, the choice of ion flux is very important, which is not only determined by the used etched parameters, but also by the shape and material of the mask and the etched structures itself. The ion flux is dependent on the mask and etched structures since ions can scatter from the features. Furthermore, the ion flow and ion-sidewall interaction can be altered due to charging of the mask if a non-conductive mask is used. These effects can cause different results for different coax dimensions and pitches. The only way to eliminate these effects completely is to use a more radical-based etching recipe (as described in Section 2.3.1). However, the impact of these effects can be minimized by optimizing the etching parameters.

We found an optimized three-step recipe, where the first step is a 15 s 50 sccm Cl_2 etch at 60 °C, a pressure of 7 mTorr, 30 W FP and 750 W ICP power. This results in a bias of ~110 V. This step is less selective than the HBr etch and removes the native oxide on the Si surface. The second step is a 2 minutes waiting time to pump out the Cl_2 gas. Then the actual HBr etch is started, using 48 sccm HBr, a low (2.6 mTorr) pressure and 100 W forward power. The resulting DC bias is ~310 V. Images of the resulting structures can be seen in Figure 2.11. The deeper areas surrounding the structures in (a) are the result of ions which are scattered off the structures, hitting

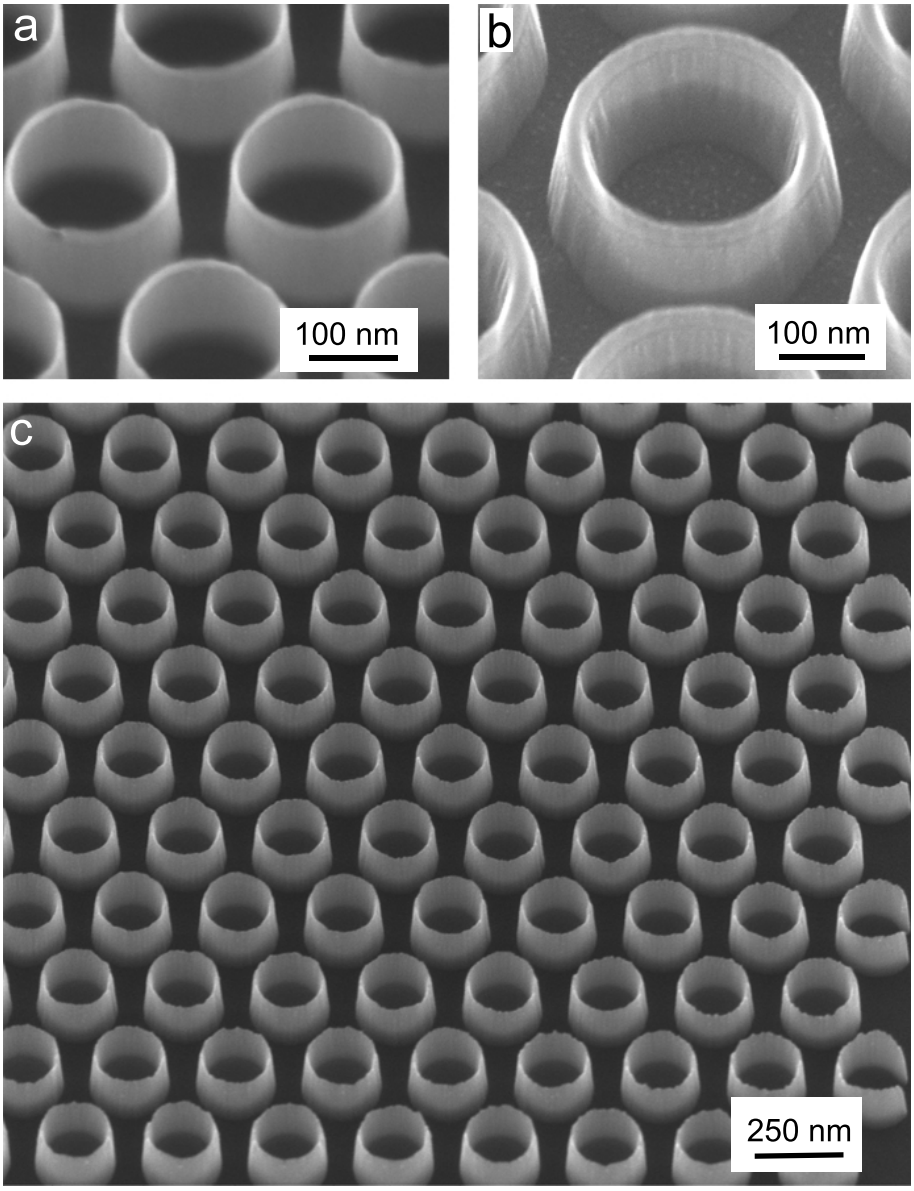

Figure 2.9: SEM images of Si rings after RIE using SF_6 and CHF_3, followed by a 10 min. 1% HF dip. (a) Using an HSQ etch mask with a small and (b) a larger wall thickness. The obtained wall thicknesses after etching are 20 and 40 nm respectively. (c) The etch is uniform over the entire 20×20 μm^2 coax field. SEM images are taken using a 5 keV electron beam.

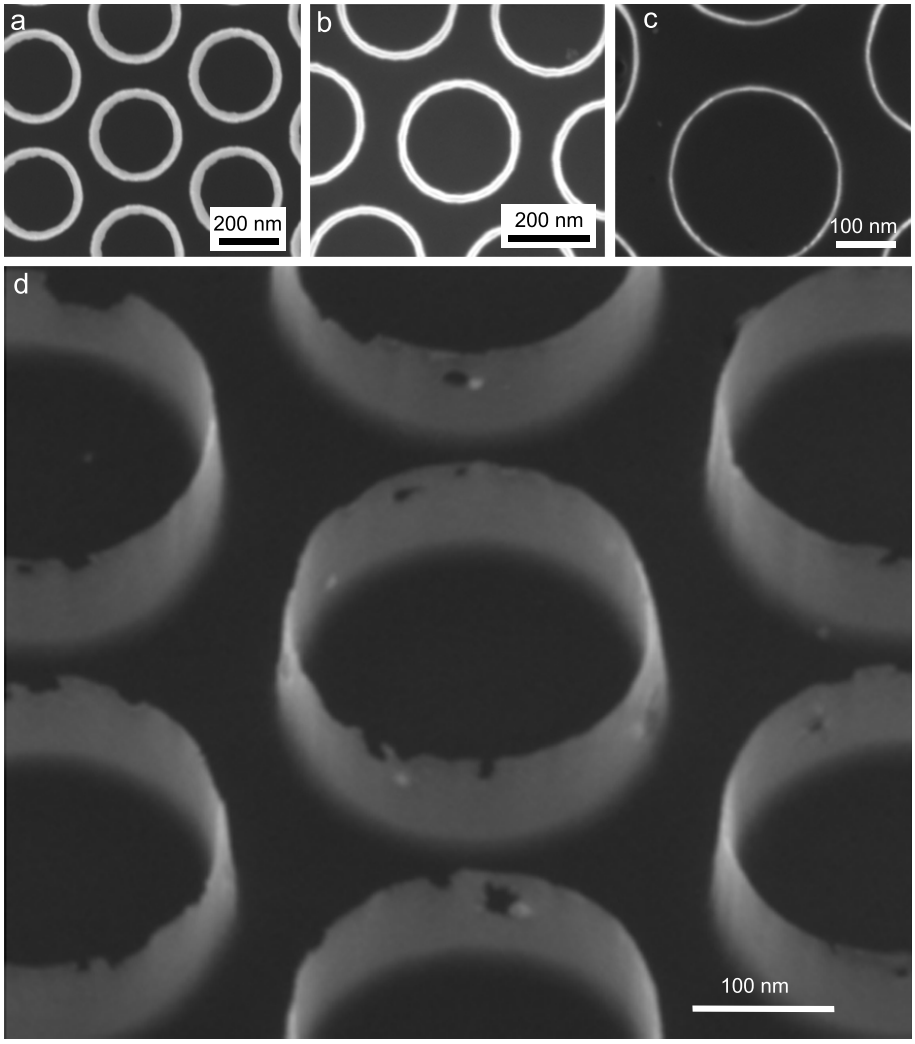

Figure 2.10: Ultra-thin Si coaxes. (a) Top view SEM image of Si rings after RIE etching, having a height of 140 nm. Wall thickness is 35 nm. (b) After first oxidation, 1 minute 950 °C 1 L/min O_2 and a 5 min. 5% HF dip. The wall thickness is reduced to 15 nm. (c) Top and (d) tilted view of the Si coaxes after second oxidation for 30 s at 950 °C 1 L/min O_2 and HF (10 min. 1%) dip. The remaining wall thickness is 6 nm. SEM images are taken using a 5 keV electron beam.

the substrate just next to the coaxes. We etched structures as deep as 500 nm by using a mask of 80 nm, resulting in wall thicknesses of only 10–20 nm. The HBr etch rate of Si is about 1 nm/s, while the mask etch rate is about 0.1 nm/s. However, the Cl_2 etch removes about 25 nm of HSQ in the first 15 s of the etching process, resulting in a lower overall selectivity, which is determined by the relative etch times of the two etching steps.

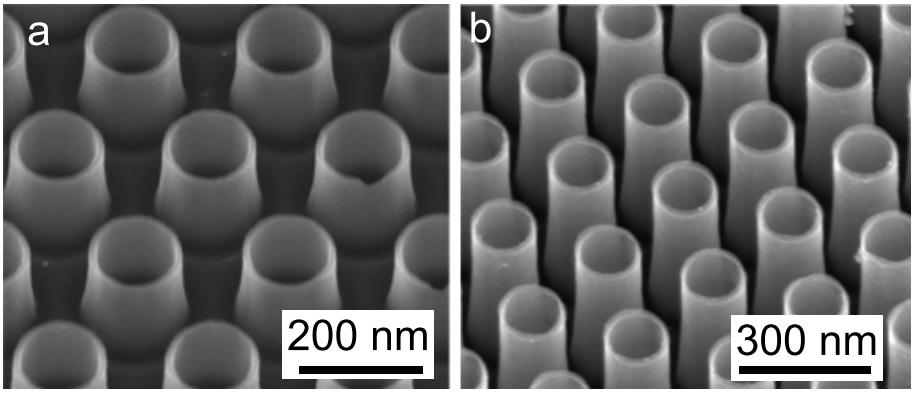

Figure 2.11: SEM images of reactive ion etched Si using HBr after a 10 minutes 1% HF dip to remove the HSQ mask. (a) 250 nm tall and (b) 500 nm tall cylinders, having a wall thickness of 10–20 nm. SEM images are taken using a 5 keV electron beam.

In general, the ion impact power increases with increasing RF power and decreasing pressure. Furthermore, increasing the pressure results in a higher angular distribution of the ion flow, resulting in less anisotropy [55]. For these reasons we chose a recipe with low pressure and relatively low RF power. This agrees with our results as shown in Figure 2.12, where an increase in pressure indeed leads to more isotropic etch profiles. Changing the RF power to either smaller or larger values both results in less anisotropy. This result is more difficult to predict a priori since the effect of the RF power is a balance between an enhanced etch rate by backscattered ions upon increasing the RF power, and an increased sensitivity of the ions to charged surfaces for lower RF powers. Both effects lead to lateral etching, and thus less anisotropy.

As explained before, a sidewall passivant is not always needed using an HBr-based etch, since the etch is dominated by ion bombardment. However, especially in the case of closely packed structures, the sidewalls of the structures can be attacked by ions which are scattered off neighboring structures [57]. To protect the sidewalls from the bombardment with these off-axis ions, O_2 can be added to form a protective SiO_2 layer on the side walls [54]. However, O_2 also increases the halogen atom density by reacting with HBr to form water and Br^* radicals.

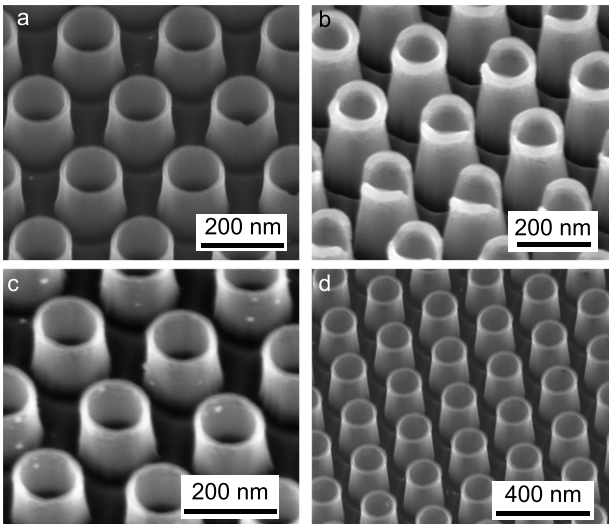

Figure 2.12: Influence of changing the pressure (a,b) and the RF power (c,d) compared to the standard etch recipe for which the lowest pressure possible (2.7 mTorr) and a RF power of 100 mTorr was used. (a) P=7 mTorr, (b) P=8 mTorr. For both cases the etch was more isotropic compared to the standard etch, where the deeper etched regions surrounding the coaxes are more pronounced in the case of higher pressures. This is due to increased ion scattering from the structures. The RF power was decreased to (c) 80 W and increased (d) to 125 W. Both results in a more isotropic etch. All SEM images where taken using a 5 keV electron beam, after a 10 minutes 1% HF dip.

These radicals can enhance lateral etching by attacking the sidewalls. We found increased isotropic etching for small O_2 concentrations, resulting in holes in the coax sidewalls as can be seen in Figure 2.13. Thicker sidewalls are observed for higher O_2 concentrations, due to the formation of a protective SiO_2 layer. Increasing the O_2 concentration even more can lead to the formation of grassy surfaces, as observed in [58]. This effect is the result of micro-masking by HSQ particles which are scattered on the substrate.

Not only the anisotropy can be altered by adding O_2, the selectivity can be changed as well. O_2 binds to C-atoms which are often present as contamination in the chamber. The selectivity is altered by adding O_2 since carbon contamination leads to enhanced SiO_2 etching, by forming CO_2, which results in a less selective etch if a SiO_x containing resist is used.

Changing the temperature changes the relative ion/radical induced etching rates. Increasing the temperature increases the surface mobility of desorbed Br-atoms and lowers the activation energy needed for the reaction of Si with Br. Both effects change the etch rate and anisotropy. Figure 2.14 shows the effect of

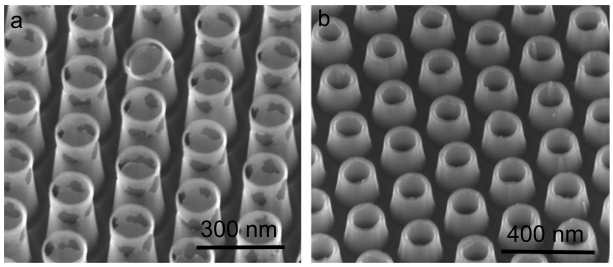

Figure 2.13: The effect of adding (a) 1 sccm and (b) 10 sccm O_2 to the standard HBr etching recipe. For small O_2 concentrations the anisotropy is decreased due to increased halogen atom density, whereas for larger concentrations the sidewalls are protected with SiO_2, resulting in thicker sidewalls. The SEM images are taken after a 1% 10 minutes HF dip to remove the HSQ mask and protective oxide layer. SEM images are taken using a 5 keV electron beam.

changing the temperature by 10 °C compared to the optimized recipe.

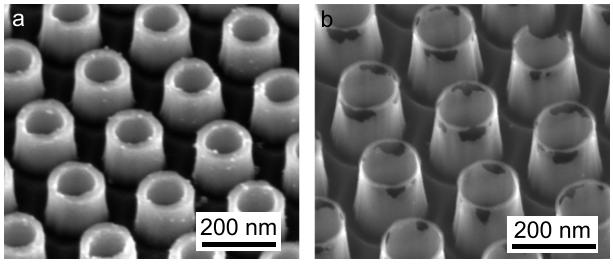

Figure 2.14: The effect of (a) decreasing and (b) increasing the temperature with 10 degrees compared to the standard HBr etching recipe at 60 °C. Both SEM images show increased isotropy compared to the standard recipe. The SEM images are taken after a 1% 10 minutes HF dip to remove the HSQ mask. SEM images are taken using a 5 keV electron beam.

Lastly, we consider the influence of adding ICP power during the etching process. Generally, using ICP power results in a higher plasma density and more lateral movement of the ions. Both results in higher isotropy as can be seen in Figure 2.15.

2.4 Metal infilling

The next step in the fabrication process is to infill the samples with metal. We demonstrate the infilling of HSQ coaxes with Ag and Au, but we successfully used the same procedure to infill Si coaxes with Ag as well.

Figure 2.16(a,b) shows SEM images of a sample composed of HSQ cylinders on

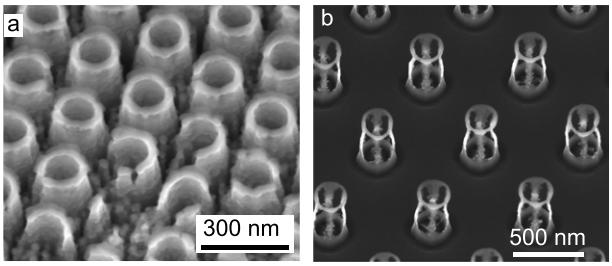

Figure 2.15: SEM images of etched coaxial structures with both RF and ICP power. In (a) the standard 100 W RF power is used together with 400 W ICP power. As observed, this combination leads to micro-masking which is probably the result of HSQ sputtering in between the coaxes. In (b) the micro-masking is prevented by lowering the RF power to 30 W, in combination with an increased ICP power of 750 W. Etching with almost only ICP power results in side wall etching and thus less anisotropy. Image (a) was taken before, and (b) after an HF dip to remove the oxide. SEM images are taken using a 5 keV electron beam.

top of a silica substrate, where the silver was thermally evaporated. The sample was aligned to be straight above the metal crucible and a metal evaporation rate of 5 Å/s was used. As can be seen from this image, there is a metal layer growing on top of the coaxes during the evaporation. This metal mushroom shadows the near surroundings of the rings, resulting in air gaps inside the metamaterial layer. Evaporation of a thin Ge wetting layer before Ag deposition to improve the metal/dielectric adhesion does not improve the infilling sufficiently (Figure 2.16(c,d)).

In order to obtain fully infilled structures, we developed a new electron beam physical vapor deposition (EBPVD) method (Figure 2.17). The sample is mounted at the center of a rotation stage, with the sample surface tilted slightly off-normal with respect to the silver crucible and an Ar^+ ion beam tilted 15° with respect to the sample surface. After every 15 nm of metal deposition the evaporation is stopped and a 2 mA 300 eV Ar^+ ion beam is switched on for 200 s to shave off the excess of metal growing on top of the coaxes. The sample is rotated during the entire process with 30 rpm. To reduce the grain size, which gives better infilling, but slightly worse optical properties of the metal, we used relatively high evaporation rates of 1–5 Å/s.

Figure 2.18 demonstrates the effect of the new method. Clearly, a significant reduction of air gaps surrounding the coaxes is observed using this new technique compared to Figure 2.16. The better infilling is due to minimization of shadowing effects from metal deposited on top of the semiconductor cylinders during the metal deposition. There is still some excess of metal on top of the structures. This could be avoided by further tuning of the evaporation:milling rates.

Although this evaporation method works well, it is not straightforward to align the sample correctly with respect to the metal vapor and the argon beam. Figure 2.19 shows SEM images of samples which were aligned differently during the

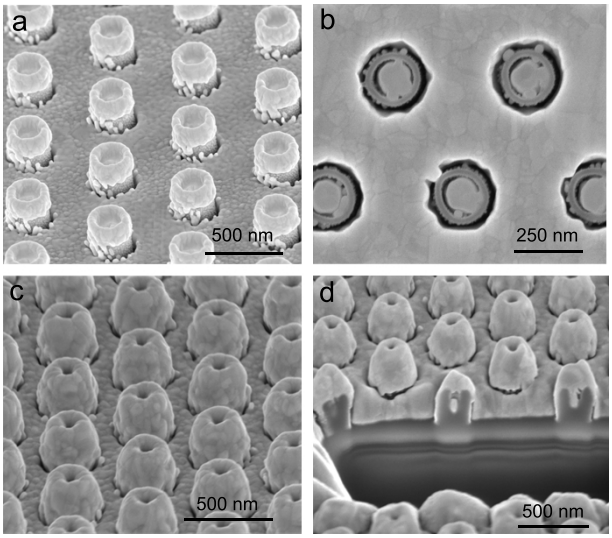

Figure 2.16: Thermally evaporated silver on top of dielectric coaxial structures. (a) The Ag grows as mushrooms on top of the coaxes, shadowing the near surroundings of the rings. (b) After polishing the surface using the FIB, clear air gaps surrounding the dielectric rings are found. (c,d) A 2 nm layer of germanium was evaporated before the metal was deposited. Sample before (c) and after (d) polishing the surface with the FIB. SEM images are taken using a 5 keV electron beam.

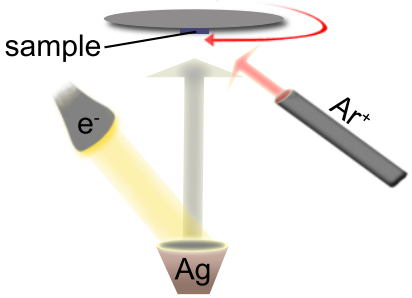

Figure 2.17: Sketch of the EBPVD setup used for the metal infilling: the sample is mounted on a rotation stage above the metal crucible, with the sample surface a few degrees off-normal with respect to the metal crucible. An argon ion gun is mounted with an angle of 15° with respect to the sample surface.

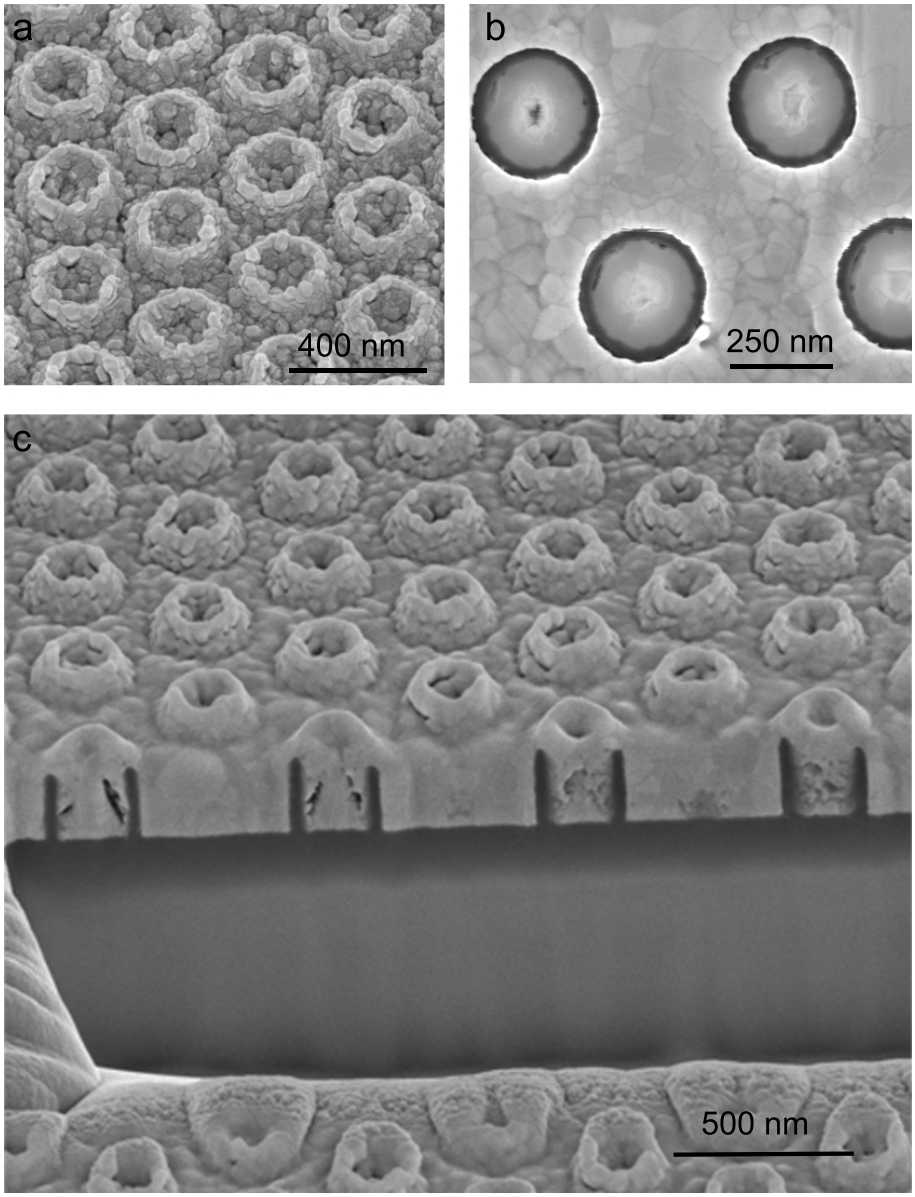

Figure 2.18: Results of the newly developed EBPVD method. SEM images of dielectric coaxes embedded in metal before (a) and after (b) polishing the surface with the FIB. (c) Cross section of the same sample shown in (a). These samples show a significant reduction of air voids compared to the SEM images shown in Figure 2.16. SEM images are taken using a 5 keV electron beam

metal infilling process. The infilling is optimal if the metal vapor is slightly tilted off-normal with respect to the sample surface. This means that it is important to rotate the sample during evaporation as otherwise the resulting samples show asymmetric infilling, as can be seen in Figure 2.19(a,b). Figure 2.19(c,d) shows the result if the sample surface was normal to the metal vapor. In between the rings (for larger pitches), the structures are nicely infilled. However, an air ring is seen between the coax center and the inner side of the dielectric ring. This can be explained by considering the non-polished image, where can be seen that the metal grows on top of the rings and thereby shadows the core.

In Figure 2.19(e,f) the sample was tilted to the other direction, such that the angle between the sample surface and the metal crucible was increased. In this configuration the coaxes shadow each other, resulting in metal accumulations in between the coaxes, at the positions where the shadowing is minimal. The infilling of the center of the coaxes show the opposite behavior as in Figure 2.19(c,d). In this case the rings are completely covered with metal, but an air gap appears in the center of the rings on the bottom of the coaxes. This is the result of the oblique evaporation, the metal deposits on the cylinder walls, thereby covering and closing the gap. In this case careful investigation of the result is required, because after a shallow polish of the cylinder the infilling seems to be very conformal. However, if the polishing is continued an air gap underneath the completely infilled center is revealed. Figure 2.19(g) shows the effect of changing the angle of the argon ion gun with respect to the metal vapor. Lastly, Figure 2.19(h) shows that there is an upper limit on the evaporation rate. Evaporating too fast results in metal sputtering, where large spheres of metal are deposited all over the sample surface.

As explained above, the alignment of the sample with respect to the ion beam and metal crucible is crucial in order to get metal infilling without any air voids. It is essential to slightly tilt the sample surface with respect to the metal crucible, which limits the maximum aspect ratio of the coaxes that we can infill. A SEM image of a high aspect ratio coax is shown in Figure 2.20(a). We found similar trends as in Figure 2.19(c,d); the side walls are completely covered with metal, but air gaps are found inside the center of the cylinders due to the excess metal on top of the coaxes which close the gap. In order to investigate this in a more controlled way, the metal infilling of cylinders with slightly different aspect ratios is considered (Figure 2.20(b-d)). In case of the smallest aspect ratio (largest ring diameter), both the walls are covered with metal and the center areas are infilled. Increasing the aspect ratio results in air gaps underneath filled coaxes, whereas decreasing the ring diameter further results in filled coaxes again. In case of the latter, the coaxes are too small in order to evaporate metal on the inner side walls of the cylinders. However, due to the rotation of the sample during the evaporation process, there is metal deposition in the center of the coax. Due to the small inner diameter, the metal in the center does reach the inner walls, resulting in full infilling of the sample. The latter process only works successfully in case of shallow coaxes, since the center of the coax will be shadowed after a while by the excess of metal growing

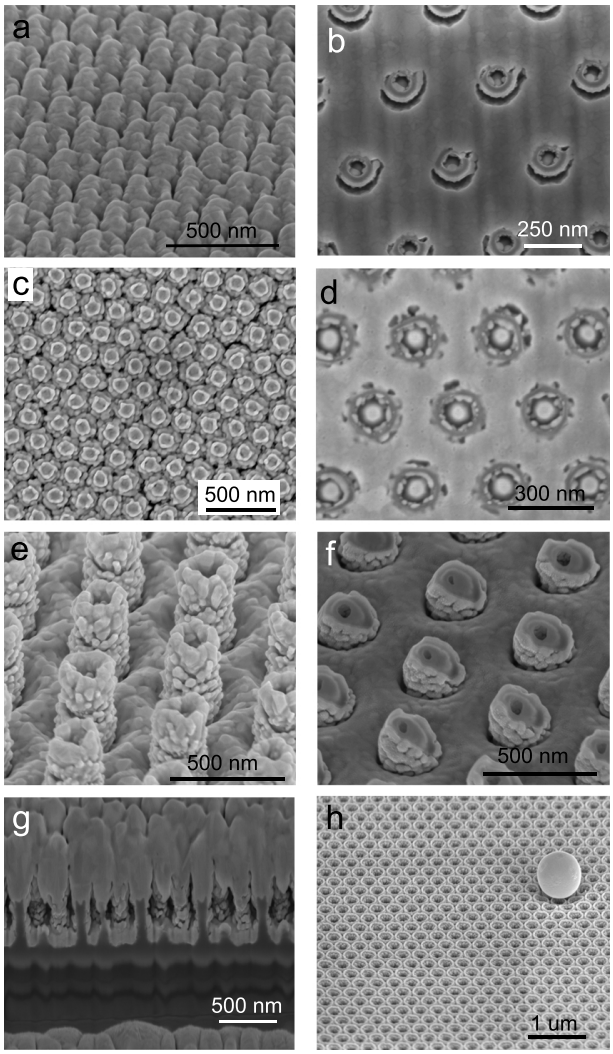

Figure 2.19: Alignment issues during the metal infilling process. (a,c,e,g,h) Are taken before and (b,d,f) after polishing with the FIB. (a,b) The gold infilling is performed without rotating the sample during the evaporation process. (c,d) The sample was rotated during the infilling process, with the sample surface tilted normal with respect to the gold crucible. (e,f) The sample as rotated, but tilted too far with respect to the metal crucible, such that the angle between the sample surface and the metal vapor was larger then in the optimal case. (g) Ion gun was mounted under 45° instead of 15° with respect to the sample surface. (h) The evaporation rate was too high (>5 Å/s), resulting in large metal spheres which are sputtered over the sample surface. SEM images are taken using a 5 keV electron beam.

on top of the coaxes.

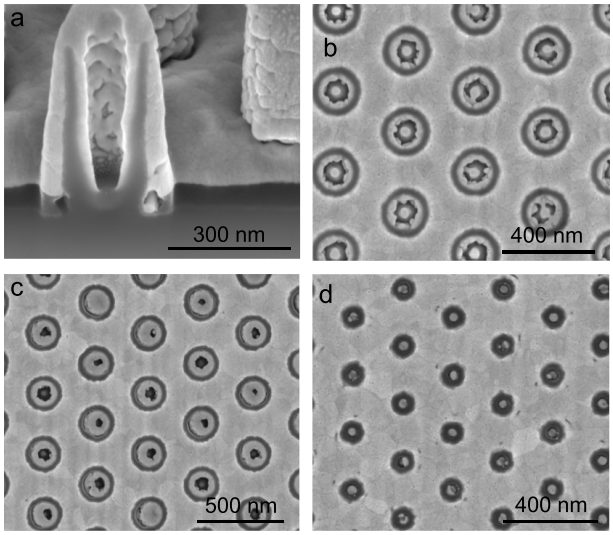

Figure 2.20: Sample limitations for the metal infilling process. (a) Cross section of a 350 nm tall coax having a diameter of 180 nm. The ring itself is covered with gold, but the inner core is completely empty. (b-d) 260 nm tall coaxes with a diameter of 200, 150 and 100 nm respectively. Images of (b-d) taken after polishing the surface with the FIB. SEM images are taken using a 5 keV electron beam.

2.5 FIB polishing

Although we do mill the excess of metal growing on top of the coaxes during the metal deposition process, the sample surface is still fully covered with metal after the deposition, as discussed in Section 2.4. To smoothen the surface and make the samples optically accessible we use the gallium ion beam of the FIB as shown in Figure 2.21(a): we come in with the ion beam under very grazing angles (4–5° with respect to the sample surface) and ideally only mill the excess of metal. For the Si membrane samples, determination of the exact angle with respect to the ion beam is difficult, due to the bending of the stressed silicon which varies with position on the sample.

To align, we tilted the stub to the point where the sample surface could just be seen with the ion beam and the square coax arrays (20×20 μm^2 typically) appear as thin lines (the side walls of the fields). Then, a rectangular box was drawn of typically $x = 20$ μm^2 (which was usually the length of the coax field), $y = 200$ nm. Here, we defined x as the horizontal axis, along the base of the coax field, and y will now define how much the beam will scan in height over the sample. The voltage

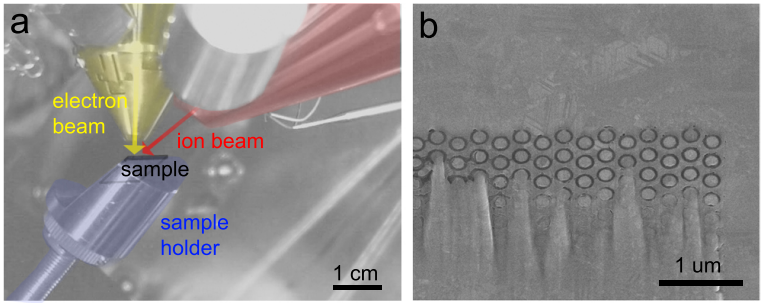

Figure 2.21: FIB polishing process. (a) Sketch of the setup inside the SEM: a special stub was used to be able to mount the sample such that is is tilted with respect to the ion beam such that the ions come in under an angle of a few degrees. (b) Top view SEM image halfway the polishing process: the dark rings are the Si coaxes which are revealed as the silver is milled away. SEM images are taken using a 5 keV electron beam.

was 30 kV, and typically we used a current of 48 pA. In this way, we succeeded in making smooth surfaces of about $20 \times 20\ \mu m^2$ within several minutes. SEM images of the resulting samples can be seen in Figure 2.22. Figure 2.21(b) shows a SEM image halfway during the shaving process: the top half of the coax field is exposed, whereas the lower half in the image is still fully covered with metal.

For this procedure the right alignment of the sample with respect to the ion beam is crucial. Firstly, we consider the shaving angle. If the angle is too steep, the resulting fields show a large gradient in thickness, as can be seen in Figure 2.23(a). The dark grey area on the top of the SEM image is Si, meaning that all the silver is removed, while on the bottom side there is almost no Si visible, meaning that we did not polish deep enough. In order to get the gradient as small as possible, we need to tilt the sample to more grazing incidence angles. However, if the angle is too small, we find sharp grooves in between the coaxes (see Figure 2.23(a)). These grooves are the result of shadowing effects. Coaxes in the path of the ion beam shadow the coaxes in front of them. As expected, this effect becomes more pronounced the further away we polish from the first row in the field, which can be seen in Figure 2.23(b). Also other objects in the ion path can give this problems, like dust or sputtered metal in front of the coax fields.

The y-size of the box is an important parameter to consider. If it is too small only a small stroke is polished, if it is too big we find again the pronounced grooves due to shadowing of other parts of the sample. The y-value defines the height of the ion beam compared to the sample surface, if the range for this value is too big, we start scanning at low positions of the ion beam, meaning that the beam is not grazing over the surface, but hits the side wall of the field. The rings are more resistant to the ion beam than the metal in between, resulting in grooves in between the rings, as can be seen in Figure 2.23(c).

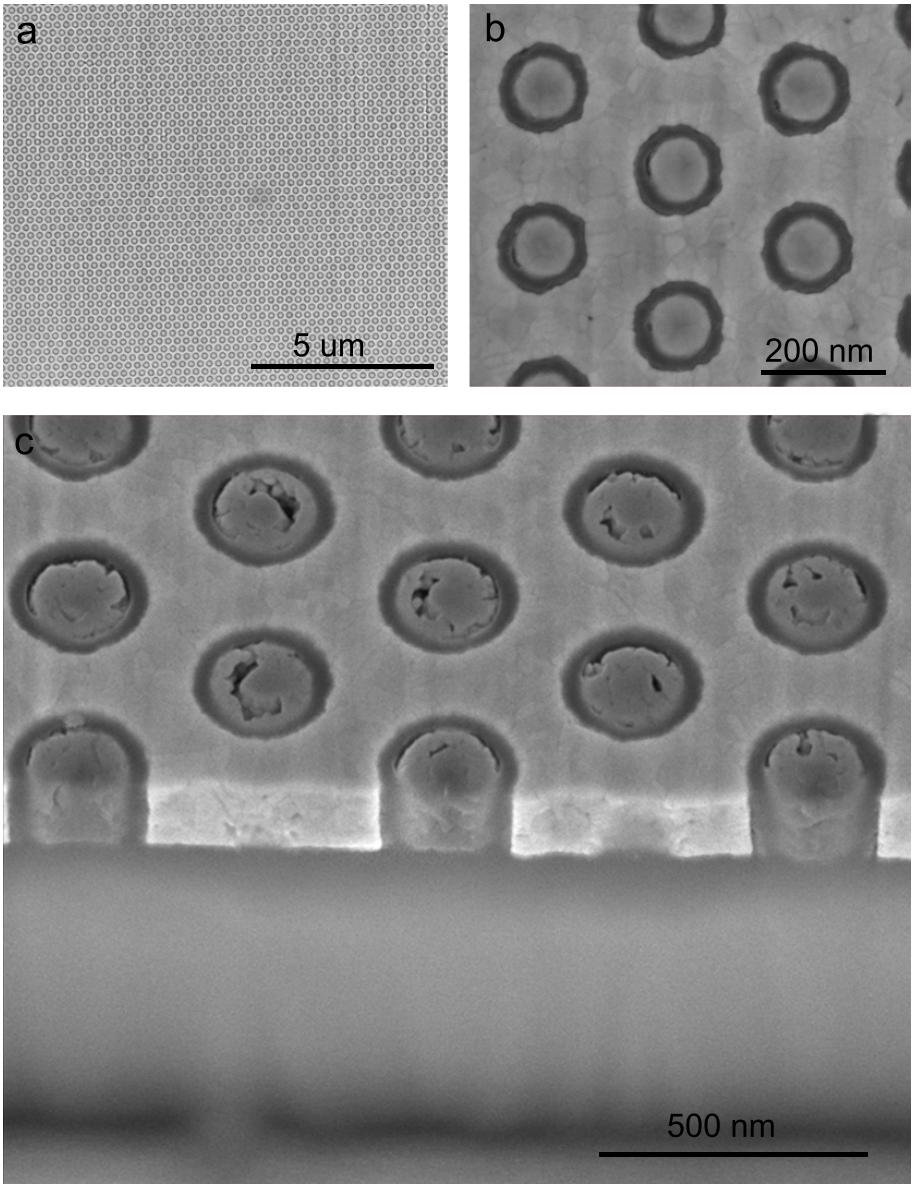

Figure 2.22: SEM images of the final metamaterial sample: the dielectric coaxes appear as dark lines embedded in the lighter colored metal. (a) Top view of a 15×15 μm^2 area, (b) top view of a small area and (c) cross section. SEM images are taken using a 5 keV electron beam.

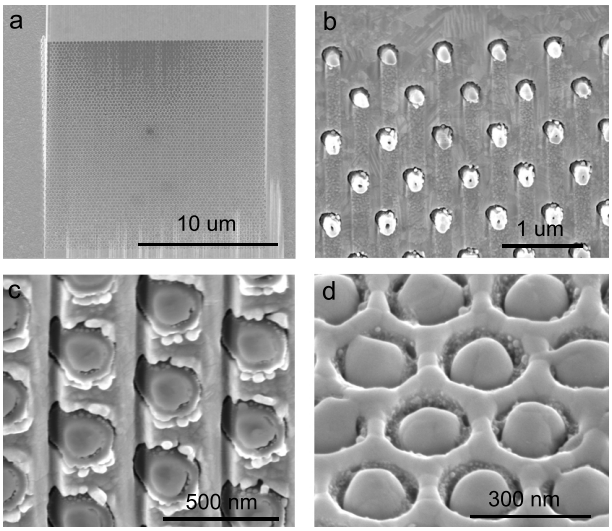

Figure 2.23: FIB polishing alignment problems. (a) Top view of a 20×20 μm^2 coax field after FIB polishing. The dark area on the top side is bare Si, where all coaxes have been shaven away. On the bottom fully metal covered coaxes are observed. (b,c) Shadowing of the coaxes: pronounced grooves appear during the polishing process. The ions come in from the top side. (d) Very short (<2 s) exposure of the ion beam under normal incidence. SEM images are taken using a 5 keV electron beam.

Milling under normal incidence results in a very rough surface and doesl not selectively etch the excessive metal. Figure 2.23(d) shows a SEM image of a field which was very shortly exposed to the ion beam under normal incidence. The metal immediately deforms, resulting in very rough surfaces.

2.6 RIE backside etch

Finally, in case of the Si membrane samples, we perform a backside etch to thin the substrate, using the same etch recipe as for etching the silicon coaxes into the silicon substrate. Figure 2.24(a,b) shows the result if the etch was too long. As can been seen in Figure 2.24(c), the metamaterial was not made completely free-standing, since the etch rate, and therefore the Si thickness, varies over the sample due to the bending of the membrane. Furthermore, we cannot measure the thickness while etching, making it very difficult to stop precisely at the back-surface of the metamaterial; all Si is etched away and only the metal remained. The coaxes have fallen out of the metal template. Typically 50–100 nm of the Si membrane remains to support the metamaterial.

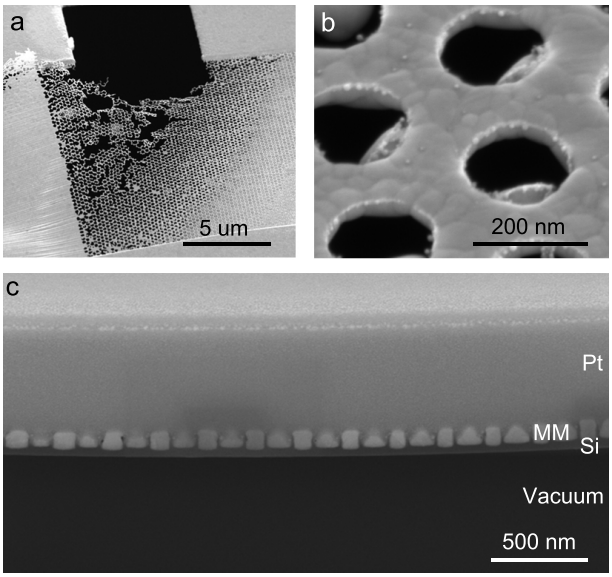

Figure 2.24: Back side etching of the Si membrane samples. (a,b) The Si was etched for too long, only the metal remained. The black square on (a) is a reference hole for the measurements. (c) Cross section of a finished 91 nm thick metamaterial sample on a Si membrane of only 17 nm. Pt was deposited to make a better cross section. SEM images are taken using a 5 keV electron beam.

2.7 Conclusions

In conclusion, we have described the fabrication process of a coaxial plasmonic metamaterial using a combination of electron beam lithography, reactive ion etching, electron beam physical vapor deposition and focused ion beam milling. Using this process we successfully fabricated the metamaterial both on glass and silicon and infilled the waveguides with either silver or gold. Freestanding structures were fabricated starting with a 1 μm thick silicon membrane. In the next chapters we will discuss the optical properties of this coaxial metamaterial and discuss its applications as negative index metamaterial in the UV/visible part of the spectrum and the usage of the plasmonic waveguides to enhance optical trapping forces.

3

Surface plasmon polariton modes in coaxial metal-dielectric-metal waveguides

In this chapter, we explore the optical properties of a coaxial plasmonic metamaterial consisting of hollow dielectric cylinders with a diameter of 100–250 nm and a ring wall width of 10–50 nm, embedded in metal. We investigate the modal electric and magnetic fields and dispersion relation for different geometries and material choices of a single coaxial channel by using realistic values for all design parameters. The Fabry-Pérot modes of a finite thickness slab are investigated with cathodoluminescence spectroscopy, and explained by extracting the mode index from FDTD simulations. Furthermore, we investigate the coupling behavior of adjacent coaxes inside an hexagonal array. We find a change from the single-ring dispersion relation for coaxes with a smaller ring-to-ring distance than 20 nm.

3.1 Introduction

The refractive index n of a material determines how an electromagnetic wave interacts with the material. Conventional media always slow down the light, and consequently shrink the wavelength, with a factor determined by the refractive index. In the field of metamaterials, where materials are designed by using sub-wavelength building blocks, materials can be realized with effective optical properties beyond what is possible with natural materials. One important class of optical metamaterials is composed of noble-metal resonant structures with a magneto-electric response (e.g. split ring resonators), embedded in a dielectric material. The

interplay between the magnetic and electric resonances can lead to an effective refractive index that is negative [5], which implies that the phase velocity of light is negative and light shows negative refraction at an interface [10–12]. However, using small resonant building blocks has several major limitations. These designs suffer from high Ohmic dissipation losses [15] and work for a limited bandwidth. Furthermore, in order for them to operate in the visible spectral range, the structures must be scaled down [13] to length scales where fabrication is hardly possible using current available nano-fabrication techniques.

An alternative way to modify the wavelength of a traveling electromagnetic wave is to couple the light into a bound mode on a metal-dielectric interface. The mode index of such a traveling surface plasmon polariton (SPP) can have a value much larger than found in naturally homogeneous materials, enabling high confinement and hence a very high local field intensity [16–23, 27]. Proper design of these plasmonic waveguides can even result in extreme cases, for instance a negative index of refraction [31] or an index near zero [4]. This would enable new application such as a flat lens [6], novel (micro-)optical components, superradiant light sources, transformation optics, and optical cloaking [7, 8].

The electromagnetic fields of an SPP decay exponentially in the direction perpendicular to the propagation direction, with a typical tail of several hundreds of nanometers in the surrounding dielectric, and a few tens of nanometer in the metal [27]. As a result, if we bring a second metal-dielectric interface within this range, thereby creating a metal-dielectric-metal (MDM) geometry, the fields of both SPPs will overlap. The coupling of the two SPPs leads to two new modes: a mode with a symmetric mode profile, and one with an anti-symmetric mode profile where fields change sign inside the dielectric waveguide channel. The latter mode can be designed to have a negative mode index, with backwards propagating phase fronts, by tuning the distance between the interfaces and the employed materials [25, 28, 30]. Interestingly, properly designing the geometry of a double periodic stacked metamaterial leads to a mode with backwards propagating phase fronts, and, due to the overall symmetric profile of this coupled mode, negative refraction behavior of the plane of the waveguides [31, 59].

Using this coupled SPP principle, a coaxial design was proposed where the double periodically stacked MDM SPP waveguides are wrapped into a coaxial geometry [32, 33]. This design is predicted to have the same properties as the planar geometry, but its response will be polarization independent. A sketch of the design is shown in Figure 3.1, where the coaxial waveguides are placed in a hexagonal array. If we consider a cross section of the structure we notice the double periodically stacked waveguide channels as discussed in [31]. Placing the cylinders in an array leads to an enhanced transmission over larger areas, compared to a single coax in a metal slab. Furthermore, the coupling of adjacent cylinders gives an extra degree of freedom to tune the SPP mode profiles, and thus the optical properties of the metamaterial. Interestingly, the coaxial design show a non-zero field overlap with a

plane wave for the negative index mode, enabling coupling to this mode from free space without the use of special gratings or wavefront shaping.

Here, we explore the optical properties of a coaxial plasmonic metamaterial. We use realistic values for all design parameters, paving the road towards experimental realization and characterization of such a metamaterial. We show the trends in wavelength for different material and geometry choices and investigate the coupling behavior between adjacent coaxial channels. Our theoretical and numerical work is supported by high resolution cathodoluminescence measurements on experimentally fabricated coaxial waveguides.

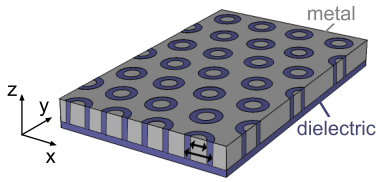

Figure 3.1: Sketch of the coaxial plasmonic metamaterial. The coaxial waveguides consist of thin (10–30 nm) dielectric channels (purple) having an outer diameter of 100–200 nm embedded in metal (grey) and supported by a dielectric bulk material.

3.2 Waveguide dispersion inside plasmonic coaxial channels

The mode dispersion of coupled SPP waveguides is the result of a complex field overlap between the different SPPs on each interface, where only small changes in the coax geometry or used material properties can significantly change this overlap, and subsequently the modal dispersion. Therefore it is difficult to intuitively predict the dispersion behavior of the modes present in the coaxial waveguides. Instead, we explore some general trends for using different materials and coax geometries by calculating the mode dispersion diagrams of single plasmonic coaxial waveguides with different geometries and material choices. For this we use the method described in [32, 33], where Maxwell's equations are solved in cylindrical coordinates for a single infinitely long coax embedded in an infinitely large metal slab. Only the first azimuthal mode number is considered, since these are the lowest order modes that can couple to free space radiation.

Figure 3.2 shows a cross section and top view of the H_y fields (where the coordinates are defined as in Figure 3.1) of the two modes which have the lowest loss, in a single coax (with azimuthal mode order 1). These are the two modes we will consider in the rest of this chapter. Figure 3.2(a,b) shows a symmetric mode, where

the H_y field does not change sign across the dielectric channel. The mode shown in Figure 3.2(c,d), represents the field of an anti-symmetric mode, of which the H_y field does change sign across the waveguide. If we consider the time dependence of both fields, we find that the symmetric mode is characterized by a positive phase velocity, and thus a positive mode index, and the antisymmetric mode shows a negative phase velocity, which is characteristic for a negative mode index.

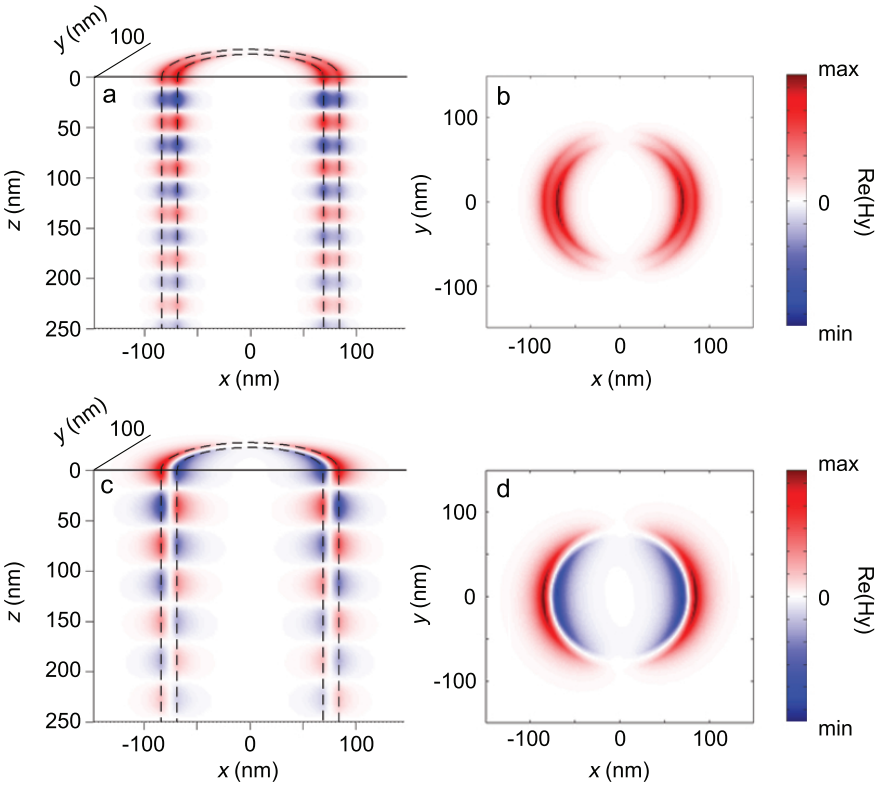

Figure 3.2: Plots of the H_y fields of the two modes with the lowest losses inside an infinitely long, single Si coax channel embedded in Ag, having an outer diameter of 150 nm and a channel thickness of 20 nm. (a) Cross section through the xz and (b) xy plane of the H_y fields of the symmetric and (c,d) the anti-symmetric coupled SPP mode. The dashed lines represent the contours of the coaxial channels. Both modes are calculated at a wavelength where the depicted mode is dominant, (a,b) at a wavelength of $\lambda = 673$ nm and (c,d) at $\lambda = 524$ nm.

3.2.1 Dielectric material and metal choice

Next, we explore how the dispersion behavior of the two modes shown in Figure 3.2 depends on the used metallic and dielectric materials. Figure 3.3 shows the dispersion of an infinitely long, 20 nm wide coaxial channel of vacuum ($n = 1$), SiO_2 ($\mathrm{Re}(n) \sim 1.5$) and Si ($\mathrm{Re}(n)$ ~3.5–6.5) embedded in either silver or gold. For the calculations we used the complex optical constants as determined by Palik [60] and Johnson and Christy [61] for the dielectric and metal, respectively. Both the real and the imaginary part of the wave vectors in the direction of traveling (z) are plotted, where the absolute value of the real part determines the SPP wavelength and the imaginary part represents the losses from which the propagation length $L_{\mathrm{SPP}} = 1/(2\mathrm{Im}(k_z))$ can be easily calculated. In order to have a negative index, the direction of the Poynting vector $\mathbf{S}$ must be opposite to the wave vector $\mathbf{k}$ ($\mathbf{k} \cdot \mathbf{S} < 0$) [31, 35, 62]. Since we only consider modes with a positive energy velocity, which corresponds to a positive imaginary part of the wave vector, the positive or negative nature of the mode is determined by the sign of the real part of the wave vector. In the rest of this chapter we use the term 'negative index mode' for the lowest loss mode which is described by a negative mode index in a part of the investigated frequency regime.

Figure 3.3 shows the existence of both a positive and negative index mode in the UV/visible regime for all material combinations explored in the figure. However, not all material combinations show a dominant region of the negative index mode in the considered wavelength regime, where the dominant mode is defined as the mode with the lowest imaginary part of k_z. From (a) we notice that the material choice of both the dielectric and the metal determine the spectral position and the magnitude of the maximum absolute value of k_z. The frequency at which k_z has its maximum is defined as the SP resonance frequency (ω_{SP}). For a single metal/dielectric interface, the SP resonance frequency is proportional to the plasma frequency (ω_{P}) of the metal and the dielectric permittivity of the dielectric material via

$$\omega_{\mathrm{sp}} \sim \frac{\omega_{\mathrm{p}}}{\sqrt{1+\epsilon_{\mathrm{d}}}}, \tag{3.1}$$

Considering the different dielectrics, the waveguides built from the high index material Si show the highest confinement, lowest losses and largest negative index frequency region of the considered materials, which is in agreement with [32]. Furthermore, we find that, in accordance with Equation 3.1, the dielectrics with the smallest real values of their refractive indices have their SP resonance at higher frequencies. Interestingly, if we consider the losses of the different waveguide materials we conclude that for the positive-index mode SiO_2 has the lowest losses, while for the negative-index modes Si, of which the refractive index intrinsically has the highest losses, results in the lowest SPP losses. This indicates that in the case of SiO_2 the field profile of the negative-index mode is relatively more localized inside the metal, which results in increased dissipation losses.

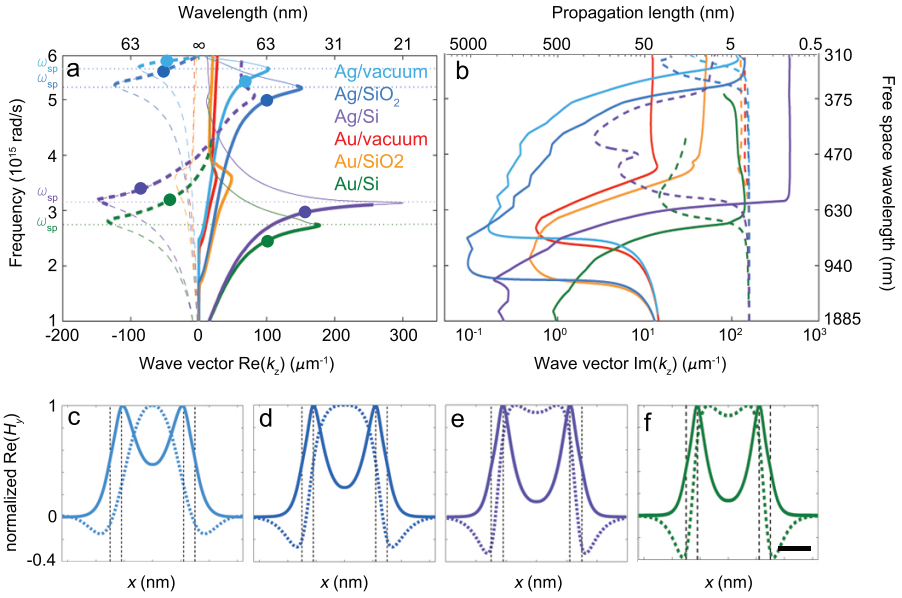

Figure 3.3: Mode dispersion diagrams of coaxial waveguide channels in the visible spectral range. The outer coax diameter is 150 nm with a 20 nm wide dielectric channel. The dispersion is calculated for three different dielectric materials (air, SiO_2 and Si) and two different metals (Ag and Au) for SPPs traveling in the positive z-direction. Both the real (a) and imaginary (b) part of the wave vector k_z are shown. The negative index modes are indicated with a dotted line, the positive index modes with a solid line. The regions in which the modes are dominant (determined by the lowest losses) are represented as bold lines. (c-f) Show the real part of the normalized H_y fields on a cross section through the center of the cylinders. Again, the solid lines represent the positive index mode and the dashed lines the negative index mode. The frequency of the plotted figures is represented by the dot in Figure (a). The scale bar represents 50 nm.

For the metals we find similar trends for the SP resonance frequencies as for the dielectrics, where the geometries with the plasma frequency at the shortest wavelength, Ag, result in the most blue shifted SP resonances. The absolute value of $\mathrm{Re}(k_z)$ at the SP resonance frequency, however, is larger for the lowest permittivity metal Ag. If we consider the losses we find lower losses for the Ag containing structures, in line with the lower losses of bulk Ag compared to Au in the considered spectral regime.

Figure 3.3 (c-f) shows the H_y fields on a cross section through the center of the cylinders. We find that for all positive modes (solid lines) the H_y field does not change sign, and the overall mode profile across the channels is symmetric. The negative index mode changes sign across the waveguide channel, but shows an

overall symmetric profile over both waveguide channels. The sign change across the dielectric channel results in a relatively large part of the field being localized inside the metal. As a result, this mode can have a negative mode index, where both the phase fronts propagate backwards and refraction is negative.

In the rest of this chapter, we will consider Ag/Si coaxes because of their large negative index frequency region, the possibility to obtain the most extreme mode index and the relatively low losses. However, depending on the applications of interest, in other parts of this thesis we occasionally use Au/Si or Au/SiO_2 for practical reasons.

3.2.2 Tuning the cylinder outer diameter

Next, we investigate the influence of changing the diameter and channel width of the coaxial waveguide channels. Figure 3.4 shows the dispersion diagrams of Si/Ag coaxes with a fixed channel width of 20 nm and a varying outer diameter. Firstly we notice that all considered geometries show strong confinement around the SP resonance frequency, with values above 400 μm^{-1} for the real part of k_z. However, for the geometry in this figure, an increase of the absolute value of k_z always results in increased losses as well. The SP resonance is at the same wavelength for all considered geometries, since it is determined by the optical constants of the materials (Equation 3.1) rather than by the geometry. Interestingly, the waveguides all show a negative-index mode which is dominant for wavelengths shorter than ~630 nm. We note, however, that there exists a third, positive-index mode which is dominant above 4×10^{15} rad/s (corresponding to wavelengths smaller than $\lambda = 470$ nm) in case of the 100 nm and 300 nm diameter coaxes (not shown here).

Considering the positive-index waveguide modes in Figure 3.4(a), we observe an increase of Re(k_z) at frequencies near the SP resonance frequency, which is most pronounced for the coax with the smallest diameter. The change in k_z is due to a different mode coupling through the metal cladding, as seen from the H_y field plots in Figure 3.4(c-f). For the largest two considered diameters, the H_y field goes to zero in the center for the positive index mode, resulting in an almost unaffected relative field distribution inside the dielectric channels, and very similar dispersion behavior of these two modes. For smaller diameters, however, the fields on both sides of the channels do overlap in the coax core, giving rise to a change in the dispersion. The negative-index mode on the contrary, does show non-zero field intensity in the center region of the metal for all diameters. The relative field distributions inside the dielectric channels however, are almost unaffected which results in an almost equal k_z for the negative-index mode for all shown diameters.

The losses show small variations for the different investigated diameters. In general the losses of the positive mode index are slightly larger for smaller diameters. In case of the negative mode index all shown coax dimensions show similar losses up to ~470 nm. For shorter wavelengths, however, the modes inside the

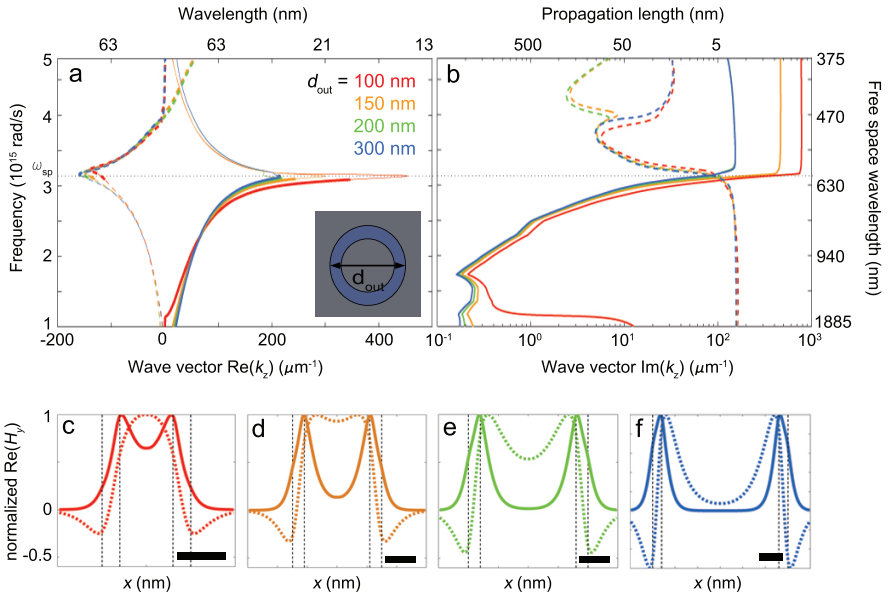

Figure 3.4: (a) Real and (b) imaginary part of the dispersion diagrams of Ag/Si coaxial waveguides with a 20 nm wide channel and varying diameter. The negative-index modes are indicated with a dashed line, the positive-index modes with a solid line. The dominant regions of the modes are emphasized with a bold line. In case of the smallest and largest outer diameters there is another, positive index, dominant mode above 4×10^{15} rad/s (not shown here). (c-f) Show the H_y field profiles for the different coax geometries, where again the positive-index mode is represented by the solid line and the negative-index mode with a dashed line. The positive-index mode was plotted at $\lambda = 673$ nm, the negative-index mode at $\lambda = 524$ nm. The colors corresponds to the same material combinations as indicated in (a). The scale bars in (c-f) represent 50 nm.

largest and smallest diameter coaxes show significantly higher losses than the 150 and 200 nm diameter coaxes.

We conclude that within the outer diameter range of 150-200 nm, while keeping the channel width and materials unchanged, the waveguide modes in the plasmonic coaxes are very similar over the investigated wavelength range. Within this range both the trends and the absolute values of the real and imaginary parts of the wave vectors are the same within a few percent. Although a smaller diameter, of 100 nm, does result in a more extreme mode index near the SP resonance frequency, this geometry shows higher losses and a smaller wavelength range for which the negative index mode is negative. Therefore we study the 150-200 nm diameter coaxes in the remainder of this chapter.

3.2.3 Tuning the dielectric waveguide width

Lastly, we explore the influence of the channel width on the dispersion of the coaxial waveguides, as shown in Figure 3.5(a,b). We observe a large difference in both the real and the imaginary parts of the wavevector for changing channel widths in the range $5-50$ nm. Using very thin channels on the order of < 10 nm, extremely high absolute values of both the positive and the negative mode indices can be obtained. However, as for the other considered SPP designs, increasing the absolute value of the mode index goes together with a decreased propagation length.

In order to understand the trends observed in Figure 3.5(a,b), we consider the H_y fields on a cross section of the waveguide channels in Figure 3.5(c-f). We observe that the field profile inside the metal, indicating the coupling between the SPPs in both dielectric channels, changes for different channel thicknesses. Furthermore, the field profiles inside the channels also change for different channel thicknesses. For small channel thicknesses, relatively more field is confined inside the metal. This enhanced interaction with the negative permittivity of the metal explains the more negative values of the mode index for smaller waveguide thicknesses. Furthermore, the increase in losses for thinner coax channels is also due to increased dissipation losses as result of the field localization in the metal.

In conclusion, an optimum geometry to obtain coaxial waveguides with a clear negative mode index and relatively low losses, has a channel width of $10-30$ nm and an outer diameter of $150-200$ nm.

In the previous sections we investigated the optical response of the plasmonic cylindrical metamaterial by considering a single, infinitely long coax. In the next sections, we will consider a hexagonal array of coaxes. We investigate if a single, infinitely long coax is indeed a valid approximation for a finite-thickness hexagonal array of coaxes, both experimentally using cathodoluminescence (CL) imaging spectroscopy, and numerically using Finite-Difference Time-Domain (FDTD) simulations.

3.3 Cathodoluminescence spectroscopy on a plasmonic coaxial metamaterial

In this section we perform cathodoluminescence (CL) spectroscopy measurements on a hexagonal array of coaxial waveguides. From the measured spectra we deduce the mode indices by matching the peaks in measured intensity to Fabry-Pérot oscillations inside the metamaterial slab.

3.3.1 Cathodoluminescence spectroscopy method

In CL spectroscopy an electron beam of a scanning electron microscope (SEM) is used to locally excite the sample with very high spatial resolution. The electric field

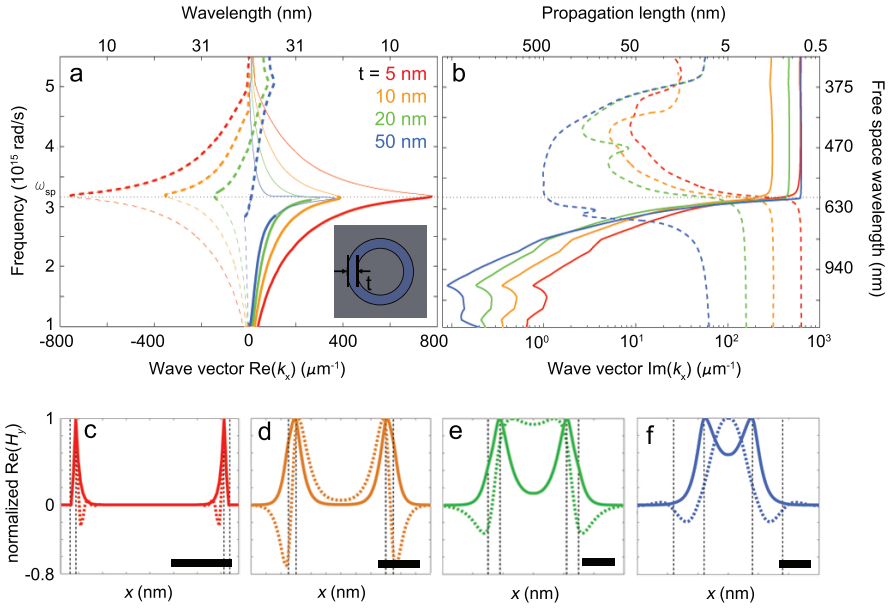

Figure 3.5: (a) Real and (b) imaginary part of the dispersion diagrams of Si/Ag coaxial waveguides with an average diameter of $r_{out} - r_{in}$ = 130 nm and varying channel width. The negative-index modes are indicated with a dashed line, the positive-index modes with a solid line. The dominant regions of the modes are emphasized with a bold line. In case of the smallest and largest outer diameters there is a second positive dominant mode above $4 \cdot 10^{15}$ rad/s. (c-f) Shows the H_y field profile for the different channel geometries, where again the positive-mode is represented by the solid line and the negative-mode with a dashed line. The positive-mode was plotted at λ = 673 nm, the negative-mode at λ = 524 nm. The scale bars in (c-f) represent 50 nm.

generated by the electron beam coherently excites resonant modes supported by the coaxial waveguides with an excitation efficiency dependent on the out-of-plane component of the local density of optical states [63, 64]. The light emitted from excited modes radiating in the far field is collected by a parabolic mirror placed between the sample and the electron column and is directed onto a spectrometer. A sketch of the setup is shown in Figure 6.3.

We laterally raster scan the electron beam in steps of 5 nm over a single coax and collect the spectrum for each excitation position. At the same time the secondary electron signal is collected, such that we can match the obtained radiation spectrum with the excitation position on the sample. After correcting for the system response we spatially average the spectrum over all positions of a single ring (including the center area) and normalize to its maximum intensity.

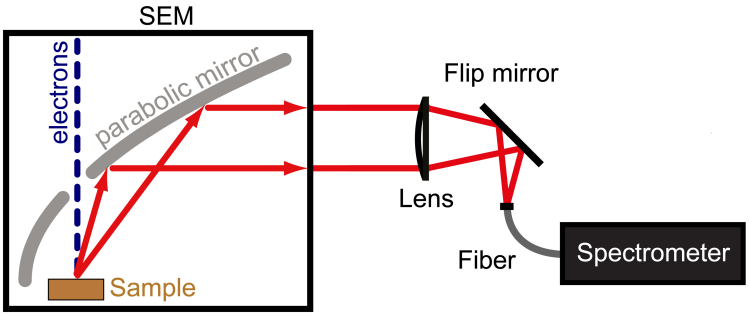

Figure 3.6: Sketch of the setup used for the CL measurements. The sample is excited using a 30 keV electron beam inside a conventional SEM. The emitted light is collected by a parabolic mirror placed between the sample and the electron column and focused to an optical fiber which guides the signal to a spectrometer.

3.3.2 Sample fabrication

The sample for the CL experiment was fabricated using the fabrication method as described in Chapter 2, where rings are written into the negative high resolution resist hydrogen silsesquioxane (HSQ) on a Si substrate, with a 30 keV electron beam. The HSQ is developed by two 30 s dips into a 25% solution of tetramethyl ammonium hydroxide (TMAH) solution in water at 50°C. Then, the hollow cylinders are transferred into the substrate using an HBr reactive ion etch (RIE). After etching the sample was dipped in a 1% HF solution for 10 minutes to remove the resist remainders. Next, the metal was evaporated using a technique where the excess of metal was shaved off using an argon ion beam after every 10-15 nm of metal deposition. Lastly, the sample surface was polished and the rings were made optically accessible using focused ion beam (FIB) milling under grazing angles. Figure 3.7(a) shows an SEM image of the sample fabricated for the CL experiment, where the inset shows a cross section of the measured sample. The rings have an outer diameter of 175 nm and a dielectric channel width of 30 nm, which is in the optimum range for having a negative-index mode as defined in Section 3.2. The pitch, defined as the center-to-center distance, is 230 nm.

3.3.3 Cathodoluminescence spectroscopy results

Figure 3.7(b) shows the normalized measured CL spectrum averaged over a single coax of the array shown in (a). We observe a clear, large peak at a wavelength of $\lambda = 856$ nm, and several smaller peaks which overlap in the wavelength region of 400-700 nm, with peak values at $\lambda = 461, 541$ and 603 nm. At $\lambda = 706$ nm there is a dip in the spectrum.

The large peak at $\lambda = 856$ nm in the CL spectrum shown in Figure 3.7 can be

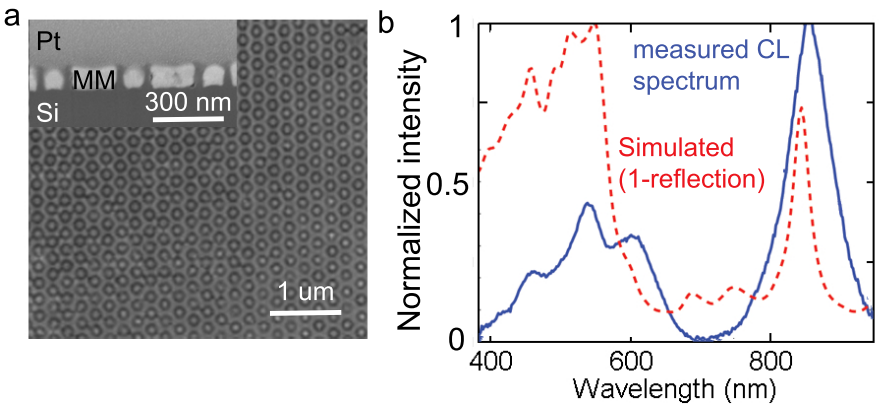

Figure 3.7: (a) SEM top view image of the 20×20 μm^2 Ag/Si coaxial array on a Si substrate used to measure the CL spectrum, where the dark rings represent the Si which is embedded in Ag. The rings have an outer diameter of 175 nm and a dielectric channel width of 30 nm. The pitch is 230 nm. The inset shows a SEM image of a cross section of the sample, where Pt was deposited in order to make a clean cross section. The measured CL spectrum is shown as the blue solid line in (b), corresponding to the normalized averaged spectrum over a single ring. The red dashed line shows the simulated 1-reflection spectrum, for a 100 nm thick metamaterial on a $n = 4$ substrate and experimentally measured coax dimensions.

understood by considering the finite thickness of the metamaterial, giving rise to Fabry-Pérot oscillations inside the metamaterial slab. Therefore, cross sections were made at different positions on the 20×20 μm^2 metamaterial field. We found a thickness in the range of 73–140 nm, where the gradient in slab thickness originates from the FIB polishing step in the fabrication process, since the sample is milled under grazing angles. Since this uncertainty in thickness is too large to determine the wavelength of the expected Fabry-Pérot resonances based on the dispersion diagram (Figure 3.8), we simulated the transmission and reflection spectra for a range of thicknesses (70–150 nm) using Lumerical [65]. For the simulations a plane wave is used to excite the metamaterial sample under normal incidence. The metamaterial dimensions were as measured from the SEM image and we used values for the optical constants from Palik [60] for Si and Johnson and Christy [61] for Ag. Since the phase shift upon reflection depends on the refractive index of the supporting material, we included a dielectric slab with index 4 as substrate, approximating the Si substrate used in the experiment.

The simulated results are shown in Figure 3.8(a). We observe a dip at $\lambda \sim 800$ nm for the smallest thickness, which shifts to larger wavelengths for increasing slab thickness. This thickness dependence of the dip position indicates that the dip in reflection reflects coupling of light into a Fabry-Pérot resonance, a standing wave inside the material which is the result of interference with the incoupled light

and waves reflected from both interfaces. Another indication that the peak at the red side of the spectrum represents a Fabry-Pérot oscillation is that the peak is absent in case the same simulations are performed without a substrate (not shown here). As in case of the measured spectrum, we observe multiple features on the blue side of the spectrum in the simulated spectra shown in Figure 3.8(a), in the range of λ =400–600 nm. These features, however, do not show a significant shift for a different slab thickness, which indicates that these dips are not Fabry-Pérot oscillations.

We observe that for a slab thickness of 100 nm the simulated spectrum matches the experimental spectrum best. We plotted the simulated data of 1-reflection for a 100 nm thick slab in Figure 3.7(b), together with the experimentally measured spectrum. The simulated reflection data was subtracted from 1 in order to make a better comparison with the CL data. We observe good agreement for both spectra in Figure 3.7(b), in both peak position and spectral shape. However, the peak intensities are different, which can be explained by the different excitation mechanisms used in the experiment (electron beam) and simulations (plane wave).

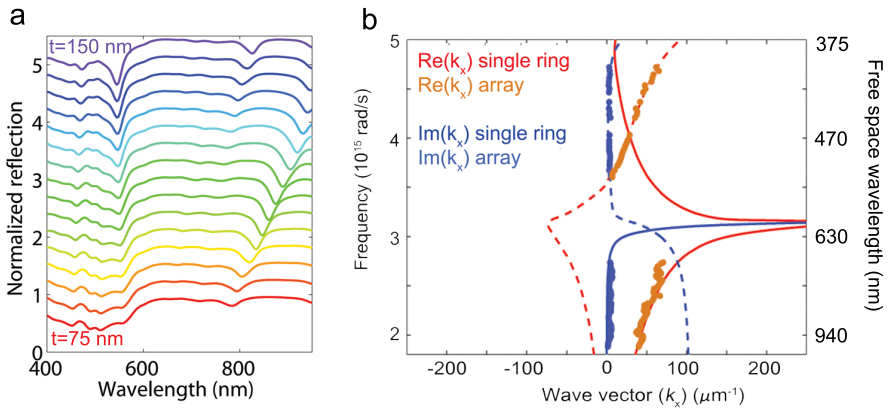

Figure 3.8: (a) Simulated reflection spectra for a coaxial metamaterial slab with rings with an outer diameter of 175 nm, a ring width of 30 nm and a 230 nm pitch for varying slab thicknesses from 75–150 nm. The spectra are offset for clarity. In (b) the dispersion diagram of a single, infinitely long coax (red and blue lines) is shown, where the real part is represented in red and the imaginary part in blue. The dashed lines are the negative-index mode, whereas the solid lines represent the positive-index mode. The data points on the dispersion diagram are the fitted wave vectors from FDTD simulations of a 5 μm thick metamaterial slab.

The simulated and experimentally measured spectra can be further understood by considering the dispersion diagram, as shown in Figure 3.8(b), where both the real and imaginary part of the mode dispersion is calculated for an infinitely long

single coax. The dots in the figure represent dispersion data extracted from FDTD simulations of a coaxial array with the experimentally measured dimensions (except for the thickness, which was 5 μm for these simulations to avoid Fabry-Pérot oscillations). The wave vector is extracted by fitting a wave of the form $A\exp(ik_z z)$ to the simulated field inside the coaxes along the propagation direction. Here, A is the complex amplitude, k_z the wave vector in the propagation direction, and z the propagation distance along the z axis. From the good agreement we conclude that the dispersion of a single coax does coincide with that of a coaxial array. Due to the high losses in the region near the SP resonance frequency, no reliable fits could be made in this region. The fit can only be performed on the propagating mode in the system, which explains the jump from the positive to the negative mode for higher frequencies. This is in agreement with the mode with the lowest losses.

From Figure 3.8 we find very high losses in the spectral range λ=600–750 nm, which explains why the CL spectrum shows a dip in the signal at λ = 700 nm. From the dispersion diagram (calculated for azimuthal mode number 1) we find a mode index of n~7 at λ = 856 nm, corresponding to a wavelength inside the material of 123 nm, close to the 100 nm thickness of the slab as assumed from the simulations of the Fabry=Pérot resonance spectra. This difference can be due to the phase shift introduced at reflection and transmission at each interface. In the simulations this phase shift is inherently accounted for. This phase shift, however, is difficult to calculate due to the multimode nature of the system which is not accounted for in using for example the transfer matrix method [66]. Another explanation for the mismatch of the SPP wavelength and the slab thickness is a (small) error in the measured cylinder dimensions, as the mode index is especially sensitive to the width of the dielectric channels. The mode we observe here is very similar to a $n = 0$, $m = 1$ whispering gallery mode, where n is the number of field antinodes in the z-direction and m the azimuthal mode number, as reported earlier in literature for larger plasmonic rings [67, 68].

Next, we consider the smaller peaks at λ = 461, 541, 603 nm in the measurements shown in Figure 3.7. The dispersion diagram in Figure 3.8(b) shows that these peaks are in the highly dispersive regime of the spectrum. Since the peak positions do not shift with changing the thickness of the metamaterial (Figure 3.8(a)), it suggests that these modes are not Fabry-Pérot resonances. However, it is difficult to prove this with certainty, due to the complicated dispersion behavior of the metamaterial. It also seems unlikely that these peaks represent coupling to surface modes in the lateral direction, which was verified by repeating the simulations with a pitch of 300 nm instead of 230 nm (not shown here). The results of these simulations show dips in the reflection spectrum at the same wavelengths as the simulations with a 230 nm pitch, indicating that the shorter-wavelength peaks are not sensitive to the coax spacing. The nature of these peaks in the spectra is subject for further research.

3.4 Coupling of adjacent cylinders

Figure 3.8(b) already showed that the dispersion calculated for a single waveguide matches the dispersion extracted from FDTD simulations well for the considered metamaterial dimensions in this figure. This indicates that the coupling of adjacent waveguide channels is not sufficient to alter the mode index significantly. However, when the coaxial channels are brought closer to each other, we expect to find a distance for which the modal fields of the adjacent channels start to overlap which will result in a change of the mode index. In this section, we explore at which ring-to-ring distances the coaxes start to couple by investigating coaxial arrays with different coax spacings.

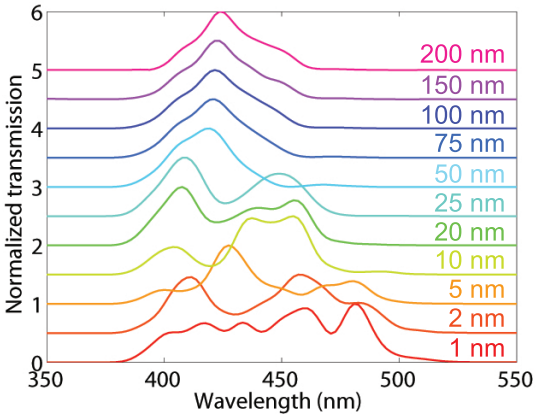

Figure 3.9: Transmission spectra of Si coaxes embedded in Ag, with an outer diameter of 168 nm and a dielectric channel width of 15 nm, where the ring-to-ring distance is systematically varied from 1 nm to 200 nm. The spectra were obtained from FDTD simulations, where a 200 nm thick free-standing metamaterial was illuminated by a plane wave under normal incidence.

Figure 3.9 shows the simulated transmission spectra for coaxial hexagonal arrays where the ring-to-ring distance is systematically varied from 1 nm to 200 nm. Here, the ring-to-ring distance is defined as the closest distance between the nearest neighbor. We used the coax dimensions for the geometry discussed in Chapter 4, with an outer diameter of 168 nm and a dielectric channel width of 15 nm. We observe identical spectra for ring-to-ring distances of 75–200 nm. For closer spacings the spectrum clearly changes; new peaks arise over a broader spectral range.

This behavior is further investigated by considering the field profiles inside the metamaterial, along the waveguide channels. Figure 3.10(a) shows the H_y field intensities inside the waveguide channel along z, the propagation axis. For intermediate propagation distances (~150–500 nm from the metamaterial surface), an

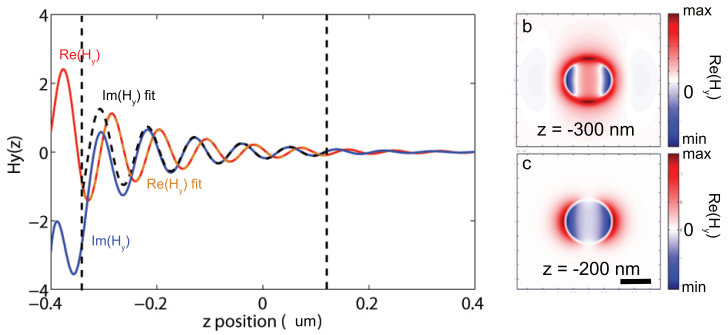

Figure 3.10: (a) Real (red) and imaginary (blue) H_y fields inside a Si waveguide channel in the propagation direction z, of coaxes with an outer diameter of 168 nm, a dielectric channel width of 15 nm and a ring-to-ring distance of 100 nm, embedded in Ag at $\lambda = 500$ nm. The interface of the metamaterial is positioned at $z = -400$ nm. The dashed orange and black lines represent the fits of the real and imaginary field respectively. The vertical black dashed lines indicate the region where the fit is performed, for smaller z-values multiple modes are present, and for larger propagation distances the field has decayed to very small values. (b,c) Show the H_y fields perpendicular to the propagation direction inside the waveguide channel at (b) $z = -300$ nm (100 nm from the metamaterial surface) and (c) -200 nm (200 nm from the metamaterial surface). The scale bar represents 100 nm.

oscillating behavior is observed from which a single wavelength can be derived. At longer propagation distances (> 500 nm) the field has decayed to very small intensities, and near the surface (< 150 nm) we find a different behavior of the field as function of propagation distance. The latter observation is explained by multi-modal behavior, resulting in interference and thus alternated field profiles. Therefore, we obtain k_z by fitting the fields for z-values large enough that only the dominant mode was present, but small enough that the fields are not decayed to such small values that no accurate fit could be made. In Figure 3.10(a) we show both the H_y intensity as function of propagation distance z and the fitted curves. We observe very good agreement between the simulated and fitted curves. Figure 3.10(b,c) show plots in the xy plane, perpendicular to the propagation direction, of Re(H_y) at different heights in the coax. The field profile in (b) is at 100 nm underneath the interface, showing a profile which is different than the expected field profile for the anti-symmetric mode as shown in Figure 3.2. The plot in Figure 3.10(c), however, shows the field profile of the propagating negative index mode. These results shows that indeed multiple modes compete with each other near the metamaterial surface, resulting in a field profile which is the result of interference of multiple modes, whereas after a certain distance only the propagating mode survives, resulting in the characteristic mode profile of only the anti-symmetric mode.

Figure 3.11(a-f) show the dispersion calculated for a single coax, together with the dispersion extracted from fits to the H_y field inside the waveguide channel of

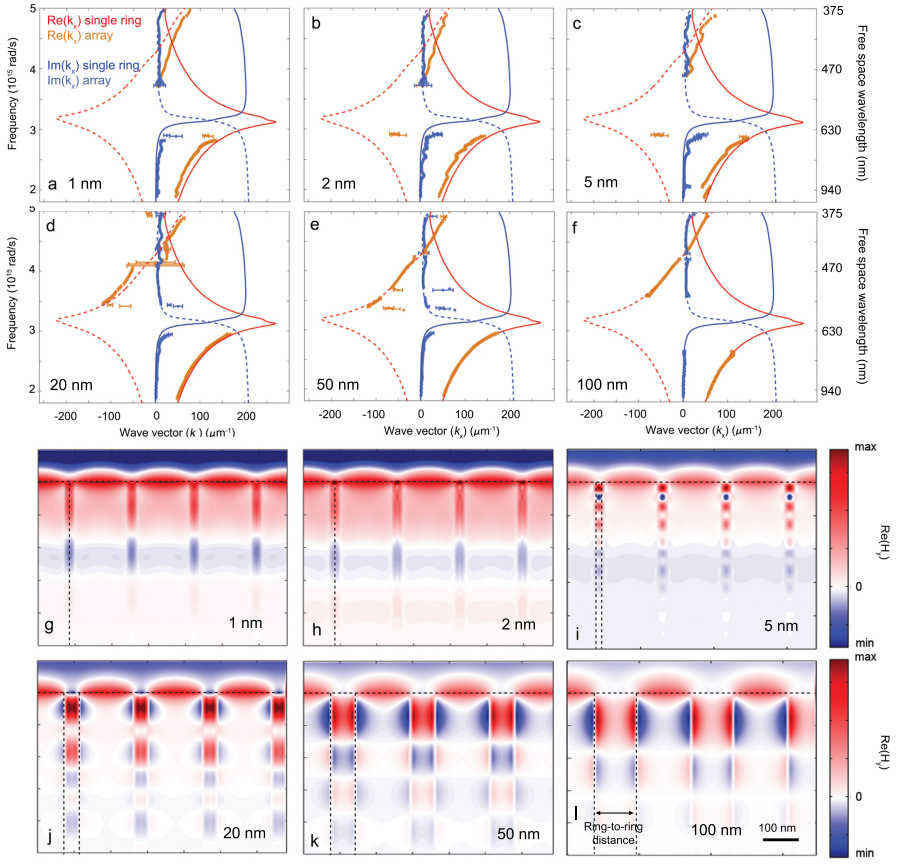

Figure 3.11: (a-f) Dispersion diagram of a single, infinitely long coaxes (red and blue lines) with an outer diameter of 168 nm and a dielectric channel width of 15 nm, where the real part is represented in red and the imaginary part in blue. The dashed lines are the negative-index mode, the solid lines represent the positive-index mode. The ring-to-ring distance is 1, 2, 5, 20, 50 and 100 nm for (a-f). The data points on the dispersion diagrams are the fitted wave vectors on field plots from FDTD simulations of a 800 nm thick metamaterial slab, which was thick enough to prevent back reflection interference. The error bars on the data points show the 95% confidence intervals obtained from the fitting procedure. Around the SP resonance frequency the error was so large due to strong absorption, that no reliable data could be derived. (g-l) Show the H_y fields for a cross section of the metamaterial at $\lambda = 460$ nm. The distance between the black dashed lines represent the ring-to-ring distance.

a coaxial array, as shown in (g-l) for ring-to-ring-distances of 1–100 nm. We find almost perfect agreement with the single coax case for 50 and 100 nm ring-to-ring distance. Decreasing the distance to 20 nm, however, does result in a small deviation of the dispersion diagrams as calculated for the single coax (d). Further decreasing the ring-to-ring distance leads to a more distinct deviation from the single coax dispersion, where for the 1, 2 and 5 nm distance (a-c) the negative index mode has disappeared. This observation agrees well with the H_y mode profiles plotted in (g-l). At a ring-to-ring distance of 50 and 100 nm, we observe a typical mode profile of the anti-symmetric mode, where the field changes sign across the dielectric channel. At smaller ring-to-ring distances, however, we find that the field does not change sign across the channel.

Comparing the results observed from Figure 3.11 with the simulated transmission spectra in Figure 3.9, we conclude that there exists a range where we observe deviations in the transmission spectra, indicating coupling of the coaxes, but the dispersion is still similar to the single-coax dispersion. This is the case for ring-to-ring distances of 50–75 nm. For ring-to-ring distances of 20–50 nm we observe indications for coupling in both the transmission spectra and the dispersion diagrams, but in this region a negative index mode can still exist. These observations are important if the coaxial building-blocks are used to design a three-dimensional metamaterial, since this can only be achieved if the coaxes are coupled with each other.

3.5 Conclusions

We investigated a coaxial plasmonic metamaterial consisting of dielectric rings embedded in metal. We show that the dispersion is very sensitive to the choice of material and geometry, and find that Si rings embedded in Ag with a diameter of 150–200 nm and a dielectric channel width of 10–30 nm have a negative-mode index with relatively low loss in the visible spectral range. Furthermore, we investigate the coupling behavior of adjacent coaxes inside an hexagonal array. We show that the transmission spectrum deviates from the spectrum of a single-coax embedded in metal for ring-to-ring distances smaller than 50–75 nm, while the dispersion changes significantly for distances smaller than 20–50 nm. In very dense arrays (ring-to-ring distance <5 nm), we observe that the negative index mode can no longer exist. These findings are important for designing a metamaterial with a three-dimensional response. Our work is supported by cathodoluminescence measurements on a experimentally fabricated coaxial array with a channel width and diameter of 30 and 175 nm, respectively. The measurements show that we are able to excite Fabry-Pérot resonances inside a 100 nm thick metamaterial slab.

4

Experimental realization of a polarization-independent ultraviolet/visible coaxial plasmonic metamaterial

We report the experimental realization of an optical metamaterial composed of a hexagonal array of coaxial plasmonic metal/insulator/metal waveguides that shows strong polarization-independent optical mode index dispersion in the ultraviolet/blue. The metamaterial is composed of silicon coaxes with a well defined diameter in the range of 150–168 nm with extremely thin sidewalls (13–15 nm), embedded in a silver film, fabricated using a combination of electron beam lithography, physical vapor deposition, reactive ion etching and focused ion beam polishing. Using a Mach-Zehnder interferometer the phase advance is measured on several metamaterial samples with different dimensions in the UV/visible part of the spectrum. For all geometries the spectral features as well as the geometry dependence of the data correspond well with numerical finite-difference time domain simulations and the calculated waveguide dispersion diagram, showing a negative mode index between λ =440–500 nm.

4.1 Introduction

Optical metamaterials are materials built from sub-wavelength-scale dielectric, semiconductor and/or metal building blocks that, together, lead to effective optical properties that do not exist in natural materials. One important class of optical metamaterials is composed of noble-metal resonant structures with a magneto-electric response (e.g. split ring resonators), embedded in a dielectric material. The interplay between the magnetic and electric resonances can lead to an effective refractive index that is negative [5], implying that the phase velocity of light is negative and light shows negative refraction at an interface. Negative refraction using such geometries was first experimentally demonstrated in the microwave spectral range [10], and more recently in the near-infrared [11, 12]. However, the realization of negative-index metamaterials in the ultraviolet and visible spectral range using this concept has proven impossible, because it requires scaling of the resonator geometry [13] to dimensions that cannot reliably be reached using electron beam lithography techniques. Furthermore, these designs relying on localized resonances strongly absorb light [15] and only work for a very narrow bandwidth. Yet, the realization of a UV/visible metamaterial with a refractive index designed by geometry is of great interest, because it may enable the realization of a polarization-independent flat lens [6] and would find applications in novel (micro-)optical components, superradiant light sources, transformation optics, and optical cloaking [7, 8], to mention a few examples [9].

To circumvent the fundamental fabrication and Ohmic dissipation problems associated with nano-resonator metamaterials operating in the UV/visible, we have proposed an alternative metamaterials architecture [31], in which the metamaterial is built up from arrays of metal/insulator/metal waveguides that support surface plasmon polaritons (SPP). The dispersion of these coupled plasmonic waveguides is tunable by the dimensions of the metamaterial, and as shown before, two-dimensional SPP waveguides can show a negative mode index, over a relatively large wavelength range, for the asymmetric in-plane plasmonic waveguide mode [35]. As we have subsequently shown, a specially designed three-dimensional array of SPP waveguides can act as a three-dimensional metamaterial with an isotropic negative index for the fundamental harmonic, due to out-of-plane coupling between the parallel planar metal/insulator/metal waveguides [31, 34]. Negative refraction of energy has recently been demonstrated experimentally in such structures [69]. However, this geometry only works for TM-polarized light. To create a polarization-independent metamaterial, we have proposed that SPP waveguides can be 'rolled-up' to form an array of coupled coaxial plasmonic waveguides (see Figure 4.1) [33]. This geometry is composed of Si cylinders with a wall thickness of 10–20 nm, which are embedded in a metal film. The asymmetric SPP mode that results from coupling of SPPs across the Si cylinders is tuned by geometry to have a negative mode index. Coupling between the cylinders will then lead to a negative index out of the plane of the waveguides, which is the

result of the key fact that the asymmetric modes are coupled [31]. As we have shown by numerical simulations [33], the propagation of light in these rolled-up structures is still described by the coupling of plasmonic waveguides with an effective mode index that is negative, but due to the symmetry the effective index is nearly independent of angle and polarization. This coaxial plasmonic waveguide (CPW) design thus provides another advantage over the split-ring geometry for which the index depends on the polarization of the incoming light. Moreover, the loss figure-of-merit of the CPW design, describing the propagation length in the material relative to the free-space wavelength, is higher than that for the split-ring design (FOM<3 for split ring resonators [15], compared to a FOM<18 for the CPW design [32]). The figure of merit for the metamaterial discussed in this paper is shown in Figure 4.5(b). Furthermore, the CPW isotropic metamaterial design can be tuned to possess a broad variety of refractive indices n, including very large negative or positive values of n including the special cases of $n = 0$ and $n = -1$.

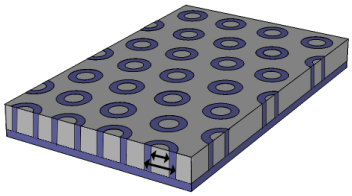

Figure 4.1: Coaxial plasmonic metamaterial geometry. Coaxial plasmonic hexagonal metal (grey)/insulator(purple)/metal waveguide array. The smallest arrow defines the inner diameter (d_a), the largest arrow the outer diameter (d_b). The coaxial Si wall thickness is defined as $(d_b - d_a)/2$.

While the CPW design has thus been theoretically and numerically predicted to show the desired negative-index behavior, its experimental realization so far has remained elusive. Here, we present the experimental demonstration of a hexagonal Ag/Si CPW geometry fabricated using a combination of electron-beam lithography (EBL), reactive ion etching (RIE), metal infiltration using electron beam physical vapor deposition (EBPVD) and focused ion beam (FIB) polishing. We perform optical interferometry to measure the phase evolution of light inside the coaxial metamaterial in the ultraviolet/blue/green spectral range (λ=351–515 nm). The measured phase is highly dispersive, and in agreement with numerical simulations and the calculated waveguide mode dispersion diagram, showing a negative mode index for λ=440–500 nm.

4.2 Sample fabrication

The fabrication process is described in full detail in Chapter 2, but we will shortly describe the fabrication process for these particular samples. The fabrication of

the hexagonal coaxial metamaterial (see Figure 4.2(a)) starts with patterning a 1 μm thick Si(100) membrane with 100 keV EBL, using the high-resolution resist hydrogen silsesquioxane (HSQ). After development in a 5% tetramethylammonium hydroxide (TMAH) solution at 50 °C we obtain hollow pillars of HSQ with a height up to 250 nm and wall thickness as small as 7 nm. Using these rings as etch mask, the coaxial structure is transferred into the Si membrane with anisotropic RIE (SF_6/CHF_3). After an HF dip to remove the remains of the resist we infill the structures with Ag, using a newly developed EBPVD method in which the sample is mounted at the center of a rotation stage, with the sample normal to the silver vapor and tilted 60 °C with respect to an Ar^+ ion beam. The sample is rotated with 30 rpm during the entire process. After every 15 nm of metal depositing we shave off the excess of Ag growing on top of the Si coaxes with a 2 mA 300 eV Ar^+ ion beam for 200 s. During the ion shaving the evaporation is stopped. This new technique leads to fully conformal infiltration of Ag, minimizing shadowing effects of Ag deposited on top of the Si cylinders. The sample surface is then polished and made optically accessible with 30 keV Ga^+ FIB milling under grazing incidence. Finally, a RIE back etch is performed to reduce the thickness of the supporting Si layer.
SEM images of the metamaterial after different steps of the fabrication process are shown in Figure 4.2(b). The final metamaterial samples, with dimensions of 20*20 μm, consist of Si rings with a well-defined diameter in the range of 150–168 nm and a wall thickness of <15 nm, embedded in Ag (Figure 4.2(b-4)). Table 4.1 lists the dimensions of each of the different CPW metamaterials that was made, measured using SEM. Both top-view SEM images and cross-sections using focused-ion beam milling were made. The outer diameter of the Si cylinders is varied from 150–168 nm while the pitch ranges from 200–300 nm in steps of 50 nm. The key feature, and the experimentally most challenging one to realize, is the Si cylinder wall thickness; it ranges from 13–15 nm. It is this small thickness that leads to strong SPP coupling across the wall thickness of the Si cylinder, and hence a negative mode index for SPPs propagating along the cylinders.

Table 4.1: Dimensions of the fabricated metamaterial fields as measured from SEM images. Layer thicknesses were measured with SEM after making a FIB cross-section. The corresponding SEM images of Samples 1–5 are shown in Figure 4.4(b), a cross-section of Sample 6 is shown in the inset of Figure 4.6.

Sample #	Coaxial outer diameter (nm)	Coax pitch (nm)	Coaxial wall thickness (nm)	Metamaterial thickness (nm)	Silicon support thickness (nm)
1	168	250	15	91	49
2	168	250	13	43	88
3	163	200	13	40	105
4	166	300	13	52	74
5	168	250	15	66	66
6	150	300	15	137	40

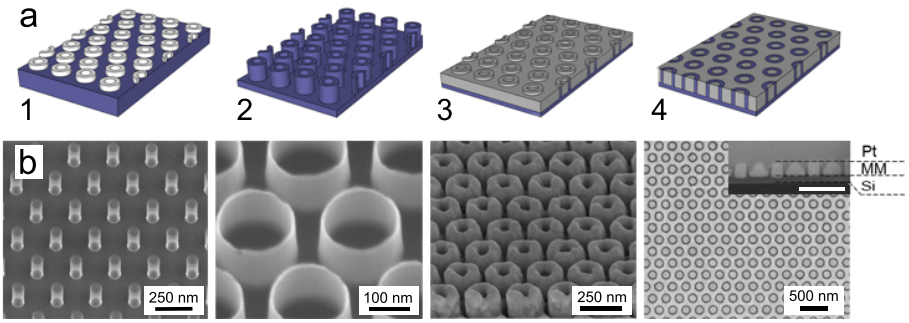

Figure 4.2: Coaxial metamaterials fabrication. (a) Schematic overview of the fabrication process: 1. EBL of HSQ on Si membrane, 2. Transfer structures into Si substrate with RIE, 3. Evaporate silver using a combination of EBPVD and Ar^+ irradiance, 4. Polish the surface with FIB. (b) SEM images taken after different steps in the fabrication process. 1. Hollow pillars of HSQ after the EBL process. The walls are almost transparent for 5 keV electrons which were used to take this image. 2. Si rings after RIE and HF dip. 3. Conformal deposition of evaporated silver. 4. Top view SEM image of the final metamaterial: Si appears as dark rings and is surrounded by silver. The inset shows a cross-section of the final metamaterial. The Si ring walls appear as very narrow dark lines in between the silver. Platinum was deposited in order to make the cross-section. The scale bar represents 500 nm.

4.3 Interferometry at visible/UV wavelengths

The effective optical properties of the fabricated metamaterial are investigated by measuring its optical path length with a Mach-Zehnder interferometer. A schematic of the setup is shown in Figure 4.3(a). Monochromatic laser light from an Argon ion laser (λ=351, 364, 458, 477, 488, 496, 515 nm), is split into a sample beam and a reference beam. The light in the sample beam is focused on the sample with a 0.45 NA objective. The transmitted light is collected by a second 0.45 NA objective and let to interfere with the reference beam on a photo diode. A piezo-electrically driven mirror in the reference arm is continuously moving back and forth over time using a saw tooth driving function. The intensity at the photodiode is then measured as function of time. The inset of Figure 4.3(a) schematically shows the measurement procedure: first a measurement is done without the sample and the absolute phase is deduced by fitting a sine function through the interference signal. Next, the metamaterial sample is placed in the sample arm and the absolute phase is determined again by fitting a sine function through the interference signal. The relative phase shift is then deduced by subtracting the absolute phase of the metamaterial sample from the absolute phase of the reference measurement. For every sample this procedure is repeated 300 times for each of the different wavelengths. Figure 4.3(b) shows histograms of the measured relative phase shift for all measured wavelengths for the sample with 168 nm outer diameter, pitch 250 nm and Si wall thickness 15 nm (Table 4.1, Sample 1). Since

all measured data points are degenerate over 2π, all data is plotted within a phase range of 0–360 degrees, which results in the discontinuities in Figure 4.3(b). The width of the histograms is mainly due to a ~25 nm uncertainty in the position of the piezoelectric mirror, consistent with the fact that the phase histograms are broader at shorter wavelengths.

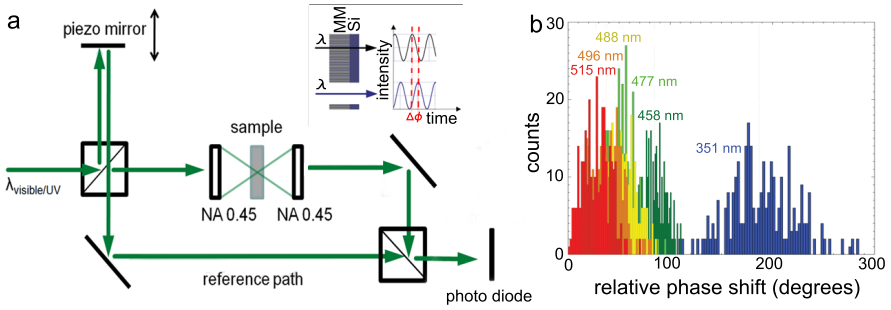

Figure 4.3: UV/VIS Mach-Zehnder interferometry on coaxial metamaterial. (a) Schematic representation of the Mach-Zehnder interferometer used to determine the optical properties of the coaxial metamaterial. (b) Histograms built up from the collection of 300 measurements, for 6 different wavelengths for the sample with 168 nm Si cylinder outer diameter, pitch 250 nm and Si wall thickness 15 nm (Table 4.1, Sample 1).

Figure 4.4(a) (red dots) shows the measured average phase shifts for 5 different coaxial metamaterial samples (Table 4.1, Samples 1–5). The error bars in the data represent the standard deviation of the collection of 300 consecutive phase measurements. Top-view and cross-section SEM images of the 5 samples are shown in Figure 4.4(b,c). Figure 4.4(a) shows several notable trends. First, for all five samples the measured phase shift strongly depends on wavelength, demonstrating the highly dispersive nature of the metamaterial. Secondly, small variations in the sample geometry lead to distinctly different phase shifts.

Next, we compare the measured phase shifts with numerical Finite-Difference Time-Domain (FDTD) simulations, performed with the experimentally measured dimensions of the different metamaterial samples as input. In the simulations the samples were illuminated with a plane wave pulse of linearly polarized broad band (λ =300–700 nm) light under normal incidence. We extracted the relative phase shifts by taking the argument of the complex transmitted electric field and subtracting the phase of the reference ($n = 1$). The results are shown as solid lines in Figure 4.4(a). Comparing the simulations with the experimental data we find very good agreement for all measured metamaterial samples. The trends of phase shift with wavelength are clearly reproduced in the simulations. Also, the different behavior measured for different sample geometries is clearly represented by the simulations. The slight differences between experiment and simulations can originate from a difference in the optical constants of the silicon and silver of the

fabricated metamaterials and those used as input for the simulations. Also, errors in the determination of the thickness of the metamaterial or in the metamaterial dimensions would give rise to a difference between simulations and experiment, as does the fact that there is a small thickness gradient (~10 nm) over the fields, originating from the final FIB polishing step. Simulations show that a thickness difference of about 10 nm in either the metamaterial thickness or the supporting Si layer thickness leads to a difference of 5–20 degrees in the relative phase shift in the measured wavelength range. Finally we note that the measurements were performed using a numerical aperture of 0.45, causing an angular distribution of the incoming light, whereas the simulations are for normal incidence.

]

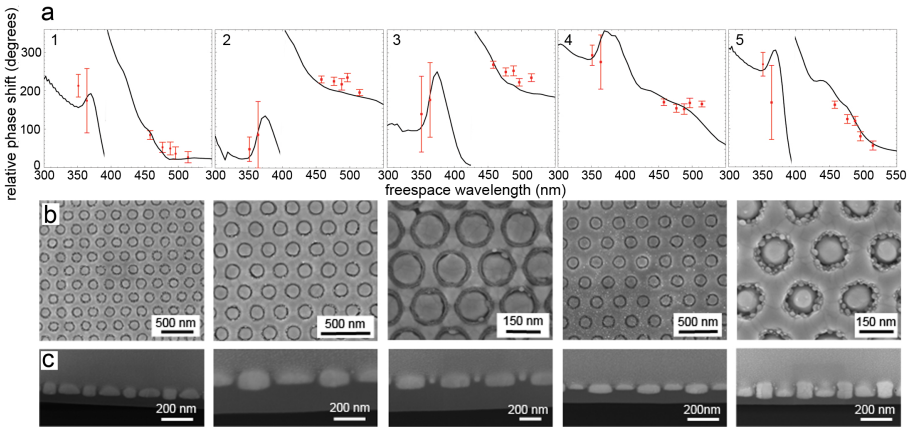

Figure 4.4: Coaxial metamaterial phase measurements and geometries. (a) Experimentally measured phase shifts for different wavelengths on 5 metamaterial samples (Table 4.1, Samples 1–5, red dots), derived from phase histograms as in 4.3. Phase shifts obtained from FDTD simulations for the corresponding geometries are shown as solid lines. (b) top-view SEM, and (c) cross-section SEM images of the sample. A layer of Pt is deposited on the metamaterial samples to make the cross-sections in (c).

4.4 Mode dispersion of coaxial waveguides

To further investigate the light propagation in the metamaterial we calculated the dispersion diagram for a single coaxial waveguide and compare it to FDTD simulations of a hexagonal array of coaxes. The dispersion diagram calculations were performed by solving Maxwell's equations in cylindrical coordinates for a single, infinitely-long coaxial silicon waveguide embedded in silver and are shown in Figure 4.5(a). As expected, the cylinder exhibits both positive and negative mode indices; for both modes the real and imaginary values of the wave vector are plotted

as drawn and dashed lines, respectively. As can be seen, the negative-index mode (blue curves) shows lowest loss for wavelengths below 580 nm; the positive mode (red line) has lowest loss above 580 nm. From Figure 4.5(a) we conclude that the negative-index mode for individual coaxial waveguide is dominant in the wavelength range 440–600 nm. For the hexagonal array of coaxes we fitted a function of the form $A \cdot \exp(i k_z z)$ to the time-averaged real part of the H_y field distribution for 6 different wavelengths (400, 440, 460, 500 and 700 nm), obtained from FDTD simulations under normal incidence. This allowed us to extract the wave vector (k_z) of the light inside the metamaterial. The refractive index is then calculated by the ratio of the free space wave vector (k_0) and the wave vector inside the metamaterial (k_{MM}) derived from the field profiles. Table 4.2 shows the refractive indices deduced from the FDTD simulations together with the effective indices calculated from the dispersion diagram for single coaxial waveguide using the geometry of Sample 1 (Table 4.2). As the analytical calculations and the numerical simulations use the same optical constants as input values, we ascribe the difference between the indices to the coupling between the waveguides. Using FDTD we also studied the time-dependence of the H_y-field and observed a negative phase advance of light in the metamaterial at λ = 460 and 500 nm, again confirming the negative-index behavior of the metamaterial in this spectral range.

Table 4.2: Refractive indices of coaxial metamaterial (Table 4.1, Sample 1) for 6 different wavelengths. Data are derived from calculated single-coax dispersion and H_y-field plots obtained with FDTD simulations. At λ = 600 nm the index is undefined since there is no propagating mode at this wavelength, making it impossible to extract the index using the method described above.

Wavelength (nm)	**Waveguide mode index from**	
	single-coax dispersion	**hexagonal array of coaxes**
400	2.35	2.17
440	0.11	−0.12
460	−1.63	−1.49
500	−4.67	−4.74
600	-	-
700	10.54	13.61

FDTD simulations were also used to simulate the transmission spectrum of the fabricated hexagonal coaxial metamaterial geometry (Sample 1). Figure 4.5(c) shows simulated spectra for the experimental metamaterial geometry (red line), as well as simulations for the silicon supporting layer only (black), and the metamaterial film only (blue). The metamaterial-only simulation shows a transmission maximum around λ = 430 nm which is consistent with the fact that the lowest losses are expected in this spectral range and that impedance matching between air and sample (with $n \sim 1$) is optimal (see Figure 4.5(a)). At the transmission maximum the calculated propagation length is 1.6 μm. For the metamaterial/Si-support geom-

etry (red curve) a sharp drop in transmission is observed for shorter wavelengths; this is mainly due to absorption in the Si support layer (black curve). For longer wavelengths the transmission decreases, even though the losses of the positive-index mode are small in this wavelength region. The low transmission in this spectral range is attributed to very inefficient coupling to the positive-index mode due to the poor field overlap of the (symmetric) modal field distribution of the positive-index mode with the incoming plane wave.

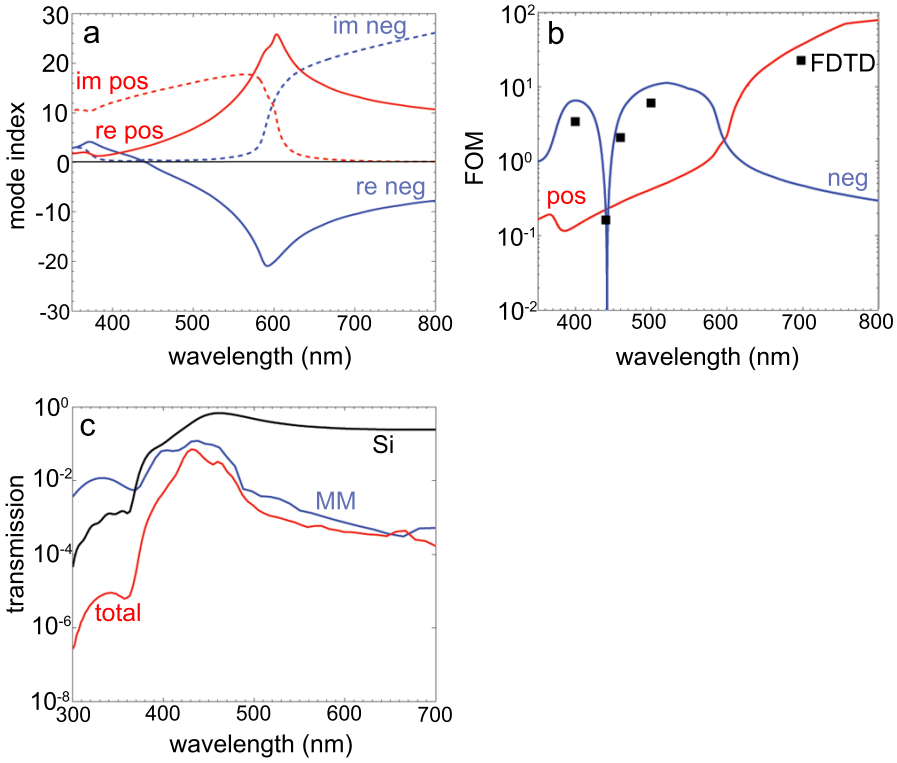

Figure 4.5: Single-coax SPP dispersion. (a) Calculated SPP dispersion diagram of an infinitely long, single Si cylinder embedded in silver, with outer diameter 168 nm, and cylinder wall thickness 15 nm (as in Sample 1). Both the real (solid line) and imaginary (dotted line) parts of the positive (red) and negative (blue) index mode are plotted. (b) Figure-of-merit (FOM) of the positive (red) and negative (blue) index mode. The FOM is defined as $|n'/n''|$, with n' and n'' the real and imaginary part of the mode index shown in (a) respectively. The black dots show the FOM calculated from the refractive index extracted from FDTD simulations (Table 4.2) (c) FDTD simulation of the transmission spectrum of the experimental metamaterial Sample 1 (red), the 49-nm-thick silicon membrane only (black), and the 91-nm-thick metamaterial only (blue).

4.5 Polarization insensitivity

Finally, we measured the polarization dependence of the metamaterial index. We used interferometry as described above and used a half-wave plate to rotate the polarization of the incoming light in 10 steps over a range of 0–60°, where the 0° orientation corresponds to along the y-axis in the SEM image of Figure 4.2(c). Measurements were done on Sample 6, with dimensions as given in Table 4.1. Figure 4.6 shows the measured phase shift at $\lambda = 488$ nm for each polarization. As above, the error bars correspond to the standard deviation of the collection of 300 consecutive phase measurements. Within the error bars we find no dependence of the phase shift on input polarization.

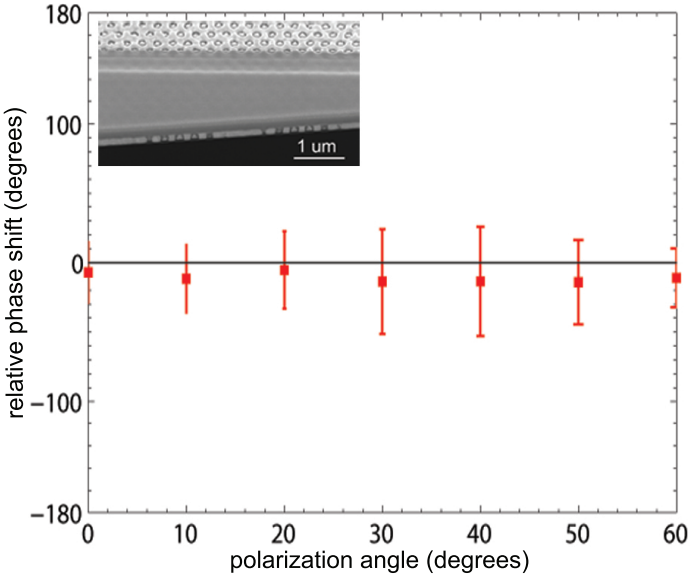

Figure 4.6: Phase shift as function of polarization. Experimentally measured phase shift for different incident polarization angles at $\lambda = 488$nm for Sample 6 (see Table 4.1). Error bars correspond to the standard deviation of the collection of 300 consecutive phase measurements. Inset: cross-section SEM image of the metamaterial sample.

4.6 Conclusions

In conclusion, we have experimentally demonstrated a polarization-independent optical metamaterial composed of coaxial plasmonic waveguides. Using interferometry, the phase evolution of light inside the metamaterial was measured in the

351–515 nm spectral range. The data are in good agreement with numerical simulations showing a negative phase advance in the 440–500 nm spectral range.

5

Enhancing optical forces using plasmonic coaxial apertures

Micrometer scale particles and molecules can be investigated non-vasively by using optical traps consisting of focused laser beams. For smaller particles, however, stable trapping in a nano-sized potential well is much more challenging. Plasmonic structures can be used to overcome the limitations for small particles, where the high confinement and exponential decay away from the surface of SPPs are used to enhance the trapping force. Here, we investigate plasmonic coaxial apertures consisting of dielectric rings embedded in metal. We numerically investigate the effects of changing the aperture geometry and arranging the apertures in a hexagonal array. After designing the optimum aperture geometry we show the first steps towards experimentally measuring optical trapping forces on both single apertures and hexagonal arrays.

5.1 Introduction

Optical trapping is a very powerful tool to investigate small particles and their interactions. Conventional optical traps consists of a focused laser beam, where the particle is pulled towards the high intensity region of the laser spot [70]. In this way, the particles can be held in place without physically attaching them to a substrate or support. This method has proven to work very well to trap and manipulate particles nonvasively in the micrometer range, such as dielectric particles [71], bacteria [72], semiconductor nanowires [73] and graphene flakes [74]. However,

since the needed trapping potential scales with the particle size to the third for small particles in the Rayleigh limit [75], trapping of sub-wavelength sized particles remains challenging. In order to stably trap a ~10 nm diameter dielectric particle a laser beam of more than 1 W is needed [70]. Such high laser powers quickly damage the particle. Furthermore, conventional traps are limited by the diffraction limit, resulting in nanoparticles being trapped in a potential well which is much larger then their own size. One solution is to connect the small particles to micrometer sized colloids which can be stably trapped [76], but this will greatly influence the dynamics of the nanoparticle.

A different solution to overcome the limitations of trapping sub-wavelength particles using optical forces is using plasmonic traps, where surface plasmon polaritons (SPPs) are used to confine light to the nanometer scale. SPPs are characterized by exponentially decaying fields away from the surface. Since optical trapping forces scale with the gradient of the fields, plasmonic traps can have very high trapping potentials. Recently a variety of plasmonic structures has been proposed for enhancing optical trapping forces, such as single and double nanoholes in a metal slab [77, 78], nanoparticle clusters [79] and bowtie antennas [80] to mention a few expamples.

Here, we consider a coaxial plasmonic geometry to enhance optical trapping forces, as sketched in Figure 5.1. The structure consists of dielectric cylinders embedded in metal. A laser is used to illuminate the structure from the bottom side, exciting surface plasmon polaritons (SPPs) in the coaxial channel. The gradient of the decaying fields on the top side of the structure leads to strong optical forces. This geometry was first proposed by Saleh et al in 2012 [81]. Numerical data show that only ~ 15 mW of transmitted power per aperture is needed to stably trap 10 nm diameter dielectric particles.

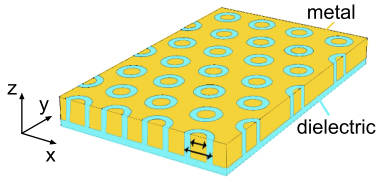

Figure 5.1: Sketch of the geometry used to enhance optical trapping forces, composed of dielectric coaxial apertures embedded in metal. The apertures are illuminated from the bottom, creating strong optical forces on the top side of the apertures.

In this chapter we investigate the trapping forces and potentials for different aperture dimensions. We show that arranging the apertures in a hexagonal array does not significantly disturb the optical trapping forces. This enables possibilities

to design surfaces with a force gradient, that can direct particles to a certain position on the surface. Furthermore, we show the first steps towards experimentally measuring the optical trapping force using coaxial apertures.

5.2 Simulating optical forces on a 10 nm diameter dielectric particle

The optical forces acting on an object can be determined by calculating the momentum transfer to the object by the local electromagnetic fields. A well known method to do so is using the Maxwell stress tensor formalism [82, 83]. In this method the time averaged flux momentum across an area containing the particle is first calculated, as given by the Maxwell stress tensor $\langle T \rangle$,

$$\langle T \rangle = \frac{1}{2}\mathrm{Re}\Big[\epsilon \mathbf{E}\mathbf{E}^* + \mu \mathbf{H}\mathbf{H}^* - \frac{1}{2}\big(\epsilon|\mathbf{E}|^2 + \mu|\mathbf{H}|^2\big)I\Big]. \tag{5.1}$$

Here, ϵ and μ are the permittivity and permeability of the medium, $\mathbf{E}$ and $\mathbf{H}$ the electric and magnetic fields, respectively, and I the identity matrix. The total optical force exerted on the object can be found by integrating the momentum flux flow over a closed surface that encloses the particle:

$$\mathbf{F} = \oint_S \langle T \rangle d\mathbf{S}, \tag{5.2}$$

where $\langle T \rangle$ is the time averaged stress tensor as given by 5.2. From these equations we find that the optical force on a particle is fully determined by the electric and magnetic fields over a closed surface that encloses the particle. Here, we use Finite-Difference Time-Domain (FDTD) simulations [65] to numerically find these fields, by placing a box of field monitors surrounding the particle of interest.

Figure 5.2(a,b) shows the transverse components (F_x and F_y) of the optical forces on a 10 nm diameter dielectric particle with refractive index $n = 2$, placed 25 nm away from a coaxial aperture. The aperture consists of 150 nm long, 30 nm wide SiO_2 channels with an outer diameter of 170 nm embedded in Ag. The particle was scanned over the xy plane, where a complete simulation was performed for each particle position.

Considering F_x (Figure 5.2(a)), we find non-zero forces on both the inner and outer side of the SiO_2 channel, which change sign across the channel. At the position of the sign change the nett force is zero, which is where the electric field intensity has its maximum (not shown here). The forces are localized around a horizontal line through the center of the coax, which is the result of the horizontally polarized plane wave used to excite the apertures. Since a positive or negative force indicates that the particle is pulled to the right or left, respectively, we observe that the particle will find an equilibrium position above the aperture where the net force

is zero. From F_y in Figure 5.2(b) we find again regions with positive and negative forces close to each other, where the force changes sign above the dielectric channel. Here, a negative force indicates pulling downwards, and a positive sign upwards (in the xy plane). The magnitude of F_y, however, is generally slightly lower than F_x. This is due to weaker confinement, and thus a smaller gradient, of the fields in the y-direction. Since we observe a position above the dielectric channel where both F_x and F_y change sign and are thus zero, this will be the equilibrium position of the particle. This is the position where the electric field intensity has its maximum. These results are in agreement with [81].

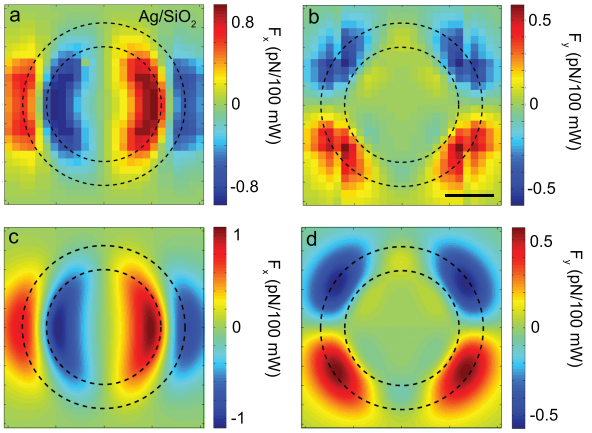

Figure 5.2: Simulated transverse components of optical forces exerted on a 10 nm dielectric particle with $n = 2$, at a distance 25 nm away from the coaxial aperture. The aperture consists of a 150 nm long SiO_2 channel embedded in Ag, and has an inner and outer diameter of 120 nm and 170 nm respectively. (a,b) F_x and F_y Forces extracted from Maxwell's stress tensor, where the particle was scanned over the xy plane in steps of 8 nm. (c,d) Optical forces calculated from the gradient of the electric and magnetic field in the absence of a particle. All simulations are performed at the transmission peak wavelength ($\lambda = 692$ nm), and the forces are normalized to 100 mW of transmitted power. We used a plane wave under normal incidence, linearly polarized along the horizontal axis.

Although the Maxwell stress tensor formalism can be used for a variety of particle dimensions and refractive indices, it is very computationally time consuming to perform a full simulation for each particle position. Therefore, we explore an alternative approach where the optical forces are calculated directly from the electromagnetic field in the absence of a particle. This method is not based on determining the flux across the particle boundary, but by calculating the local Lorentz force density by considering the particle as a point dipole. Therefore, this method is valid for small particles in the Rayleigh regime (with $d \lesssim \lambda/20$), where the particles are assumed to be sufficient small such that the field is constant over the entire

particle, and the field is not distorted by the particles. In the Rayleigh limit the time averaged gradient force is given by

$$F_{\text{grad}} = \pi n_2^2 \epsilon_0 a^3 \left(\frac{m^2 - 1}{m^2 + 2} \right) \nabla |E(r)|^2, \tag{5.3}$$

where n_2 is the index of the medium surrounding the particle, ϵ_0 the vacuum permitivity, a the radius of the particle and m the refractive index ratio of the particle n_1 / n_2 with n_1 the index of the particle [82, 84]. We note that the total force exists of the gradient force and the scattering force. However, for the case of a particle with a 10 nm diameter, the transverse scattering forces are negligibly small for the geometry considered here.

Figure 5.2(c,d) shows the transverse components of the optical forces 25 nm away from the aperture, calculated with Equation 5.3. The particle and aperture geometry is the same as considered in (a,b), and the electric field used in the calculation was extracted from FDTD simulations. Clearly, both methods agree very well with each other in both shape and magnitudes of the force fields.

Next, we investigate the potential of the optical forces in the xy plane, which is a measure of the stability of the trap. The potential can be found by simply integrating the trapping force from infinity to the point of interest ($\mathbf{r}_0$) [81, 85]:

$$U(\mathbf{r}_0) = \int_{\infty}^{\mathbf{r}_0} \mathbf{F}(\mathbf{r}) d\mathbf{r}. \tag{5.4}$$

Figure 5.3 shows the potential in the xy plane, for the same particle and aperture as considered in Figure 5.2. The potential was calculated at different distances from the aperture and normalized to kT, where k is the Boltzmann's constant and T the temperature. We define a stable trap as having a potential of more than 10 kT, which is enough to overcome the thermal energy and Brownian motion of the particle [70, 81, 86].

In Figure 5.3(a) we observe two potential wells per aperture, for all shown distances from the aperture. Figure 5.3(a) shows that with a transmitted power of 100 mW through a single ring, the particle can be trapped at a distance 30 nm from the aperture. Decreasing the distance results in exponentially increasing trapping forces, with a potential of -180 kT/100 mW for a particle at the surface. Since we need 10 kT for a stable trap, this means that we only need 5.6 mW transmitted power to trap a particle at the surface. Not only the magnitude of the potential well changes for changing distances, also the full-width at half maximum (FWHM) of the potential well decreases if the particle approaches the aperture.

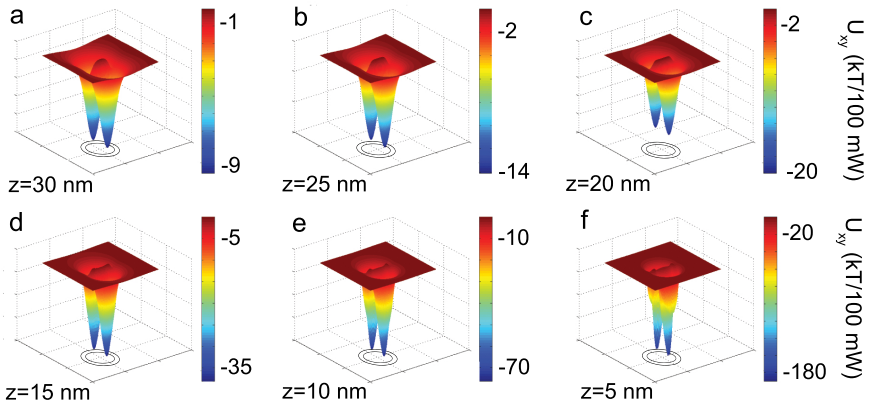

Figure 5.3: Simulated transverse component of the optical trapping potential for a 10 nm dielectric particle with $n = 2$. The potentials are calculated for different distances between the particle and the coaxial aperture, at the transmission peak wavelength ($\lambda = 692$ nm). The aperture consists of a 150 nm long SiO_2 channel embedded in Ag, and has an inner and outer diameter of 120 nm and 170 nm respectively. The potentials are normalized to kT/100 mW of transmitted power.

5.3 Trends in optical forces for different aperture geometries

In the section above we showed that we can calculate the optical forces acting on a small particle directly from the electric field in the absence of the particle. In this section we use this method to investigate the behavior of the optical forces for a different metal choice and aperture geometry and investigate the effect of placing the apertures in a hexagonal array.

First, we investigate the forces in case we replace the Ag, as used in Figure 5.2, with Au. Using Au would be preferable for experimental work since Au is much more stable upon oxidation than Ag. Figure 5.4(a,b) show the optical forces 25 nm away from a coaxial aperture in Au. The aperture has the same dimensions as considered in Figure 5.2. From the force maps we observe that the force does not change significantly upon changing the metal from Ag to Au. However considering the simulated transmission spectra of both apertures (Figure 5.5), we find that the transmission spectrum of the apertures in gold is about half that of the apertures in Ag. This is due to the higher losses of the SiO_2/Au SPP as shown in Chapter 3. As a result of the lower transmission in case of gold, the input laser power needs to be almost twice as high for the gold apertures to reach the same trapping force.

Next, we consider a hexagonal array of apertures with a pitch, defined as the center-to-center distance, of 300 nm (Figure 5.4(c,d)). Placing the coaxes in an

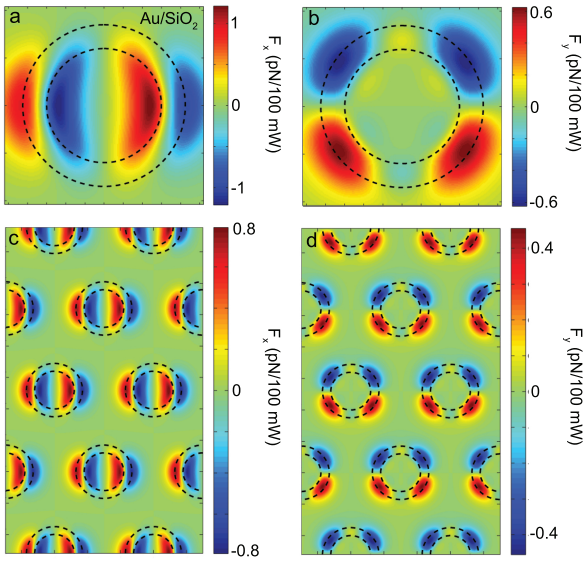

Figure 5.4: Simulated transverse components of optical forces exerted on a 10 nm dielectric particle with $n = 2$, at a distance 25 nm away from the coaxial aperture. The aperture consists of a 150 nm long SiO_2 channel embedded in Au, and has an inner and outer diameter of 120 nm and 170 nm respectively. (a,b) Forces for a single aperture in a metal slab; (c,d) results for a hexagonal array of apertures with a 300 nm pitch. All simulations are performed at the transmission peak wavelength ($\lambda = 733$ and 724 nm for (a,b) and (c,d) respectively), and the forces are normalized to 100 mW of transmitted power. We used a plane wave under normal incidence, linearly polarized along the horizontal axis.

array has several advantages over the single apertures. Practically, it is easier to fabricate an array of apertures. Furthermore, it is difficult to find a single nano-coax in the AFM measurements. Also, an array gives the ability to design a surface with an engineered force gradient, by using different coax geometries, such that the particles could be directed to a certain position on the sample. The results shown in Figure 5.4(c,d) demonstrates that the forces of a coax in an array are only slightly reduced in magnitude compared to the single coaxes in (a,b). In case of the arrays the forces are normalized to 100 mW of transmitted power through a single coax.

Lastly we investigate the trapping potential for different aperture diameters and channel widths. Figure 5.6(a) shows the transmission spectra for channel widths of 75 nm (no metal core) to 0 nm (no channel) for a coaxial aperture with a 75 nm outer radius. We observe that for channel widths smaller than ~35 nm the transmission significantly decreases. Also, the transmission peaks shift and split for decreasing dielectric wall width. Both observations are a result of the changing mode index, which is very sensitive to the dielectric wall thickness (see Chapter 3). Figure 5.6(b)

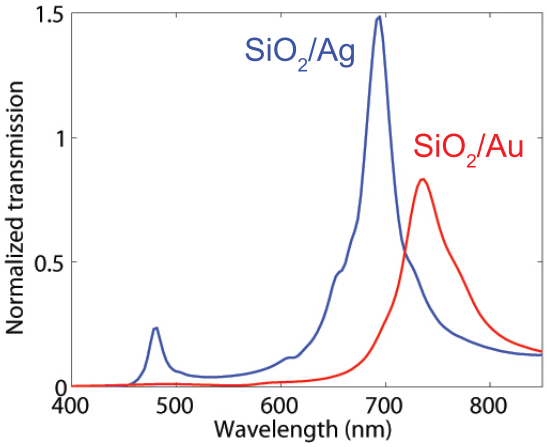

Figure 5.5: Simulated transmission spectra of a single aperture SiO_2 in an Ag (blue line) or Au (red line) slab. The aperture consists of a 150 nm long channel, and has an inner and outer diameter of 120 nm and 170 nm respectively. The transmission was normalized to the area of the coax (πr^2, with r the outer radius of the coax).

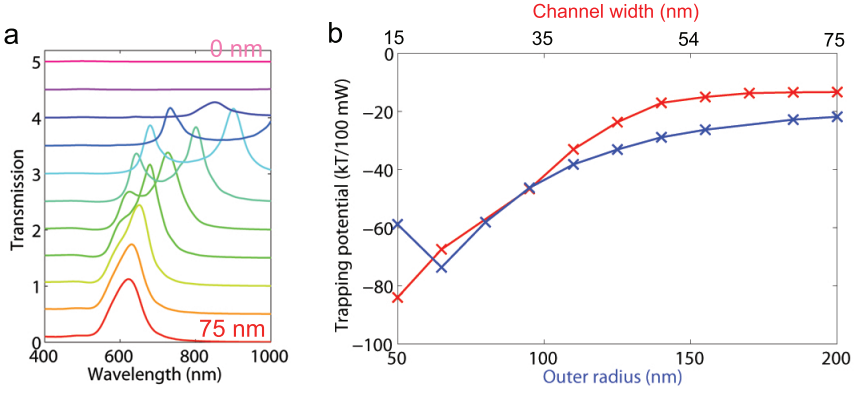

Figure 5.6: (a) Simulated transmission spectra for single coaxial SiO_2 apertures embedded in gold, for different dielectric wall widths from 65 nm (red), to 0 nm (pink). The aperture outer radius was 75 nm. The transmission is normalized to the area of the coax and offset for clarity. (b) Trapping potential as a function of channel width (red) and outer radius (blue) of the apertures. The outer diameter was fixed at 75 nm for the varying channel widths. For the varying outer diameter the channel width was fixed at 25 nm.

shows the trends of varying channel widths and outer radius of the apertures on the trapping potential. Since apertures with a channel width smaller than 15 nm have a very low transmission, we only consider larger apertures. We observe a deeper potential well for smaller widths, which is the result of increasing field confinement. For the outer radius we observe a minimum for a radius of ~70 nm. A larger radius results in less confined fields, resulting in a larger potential. However, a too small aperture results in distortion of the fields since the fields above the channels start to overlap through the aperture center. This results in a reduced trapping force, and thus potential.

5.4 Method to measure optical forces

In the remainder of this chapter we will discuss how we can experimentally measure optical forces using an AFM, and show the first measurements on a single coax and a coaxial array. Figure 5.7 shows a sketch of the setup. The sample is excited from the bottom side with a supercontinuum laser source, which is focused with a 50x objective on the sample. The transmitted light induces optical forces, which can be measured with the tip of the AFM. A diode laser is reflected from the tip, of which the light is detected by a two quadrant photo detector. The position of the diode laser light on the photo diode determines the tip deflection, which can be directly translated into a force if the spring constant of the tip is known. In order to be able to measure small signals, the excitation laser light is chopped with a frequency of 1 kHz and the deflection signal is processed by a lock-in amplifier. The AFM is a commercial setup from Asylum Research, in which a filter was built to prevent interference of the force excitation light with the signal of the diode laser.

The measurements can be performed in either tapping mode or contact mode. The advantage of using contact mode is that it is less time consuming in case of measuring a surface map, since the surface topography is scanned first in contact mode, which is then used to keep the tip at constant distance above the surface to measure the force. The downside is, however, that a contact mode scan can only be performed using a tip with a small spring constant since a stiff tip would scratch the sample. Using a tip with small spring constant has the problem that it is strongly attracted by the adsorbed water layer on the surface. This strongly limits the minimum height at which the forces can be measured. Therefore, we use the tapping mode, where a stiffer tip can be used. In this method the tip is approached to the surface for each position on the sample. From the deflection signal as function of sample height the position of the surface can be determined. A typical single-point measurement is shown in Figure 5.8. First, the sample is approached to the tip (red line). Since the tip is not interacting with the surface at large distances, the deflection signal is constant. At a certain point, about 10 nm in this case, the deflection signal suddenly drops. At this position the tip is snapped into the adsorbed water layer on the surface. Bringing the sample closer to the tip results in a reduced tip deflection, where at a certain point the deflection

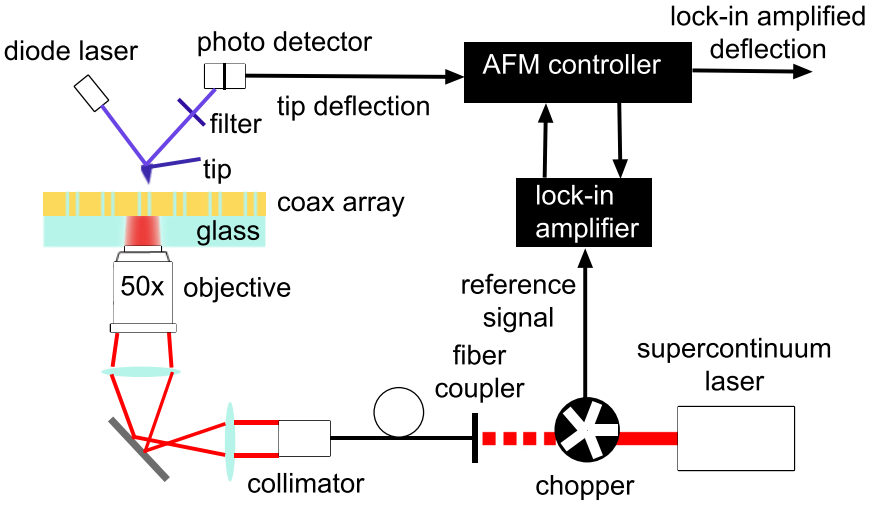

Figure 5.7: Sketch of the setup. The optical forces above the sample surface are measured with a conventional AFM where a supercontinuum laser is used to illuminate the sample from the bottom side. An optical filter is used to prevent interference of the diode laser with the excitation beam. The deflection signal is processed by a lock-in amplifier in order to be able to measure small signals.

is equal to the deflection in the region where the tip was not interacting with the sample. This point is defined as the surface of the sample. Decreasing the distance between the tip and the sample further results in a deflection of the tip in the opposite direction. Next, we move the sample away from the tip (blue line). For small distances between the sample and the tip, the trace and retrace signals overlap, but the retrace signal still interacts with the sample at longer tip-sample distances than was the case for approaching the sample. The reason is that the tip has to overcome a large energy barrier to be released from the water on the surface. This happens at about 25 nm, where the tip suddenly releases and the deflection restores to zero. In case of the force measurements, the tip can now be parked at a certain position above the surface to measure the optical forces. This position is labeled as the dwell position in Figure 5.8.

5.5 Measuring optical forces on single coaxial apertures

Here, we discuss the first optical force measurements on coaxial apertures. For these measurement we used single apertures with a relatively large diameter (~400

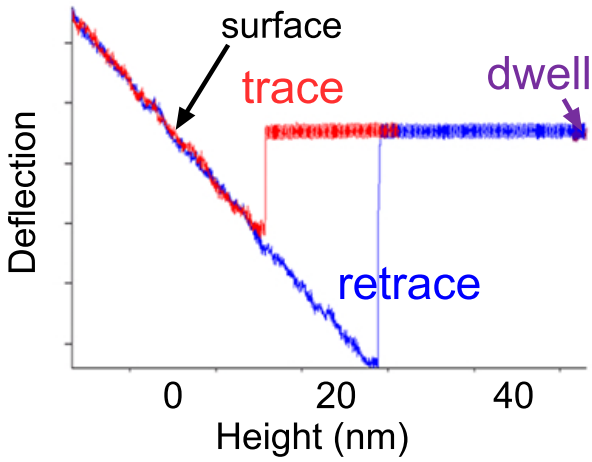

Figure 5.8: AFM measurement used to determine the position of the sample surface. The red line is measured while the sample is moved towards the tip, the blue line for increasing tip-sample spacing. At the position indicated by the purple arrow the tip is parked at constant distance for a set time. During this time the optical force can be measured. The surface is defined at height=0.

nm), consisting of air rings in gold. These structures are chosen because of their relatively simple fabrication process, which only involves gold evaporation on a glass substrate followed by milling the rings in the metal using a FIB. Since gold is milled much faster then glass with the FIB, the substrate acts as an etch stop. Therefore, the length of the aperture channels is very well controlled. SEM images of these structures are shown in Figure 5.9. Due to the milling process the aperture channels are slightly tapered. The tapering enhances the trapping forces, compared to apertures with a channel width as measured from the top part, due to the increased confinement of the fields [81].

Figure 5.10(a) shows the forces measured at a constant height of the sample, using a Si cantilever with a spring constant of ~2nN/nm. The position of the sample surface was first determined using the method shown in Figure 5.8, after which the force was measured during the dwell time. During the dwell time the laser light was switched on and of several times. The measurements were performed using two different excitation wavelengths: λ = 750 nm, which is at the transmission peak, and λ = 620 nm, off resonance. We observe two interesting trends in Figure 5.10(a): first, the force is clearly higher if the excitation laser is on, and the signal is reproducible if the light is switched on and off. Second, the forces excited at the peak wavelength of the transmission clearly have a larger magnitude then the forces excited off resonance.

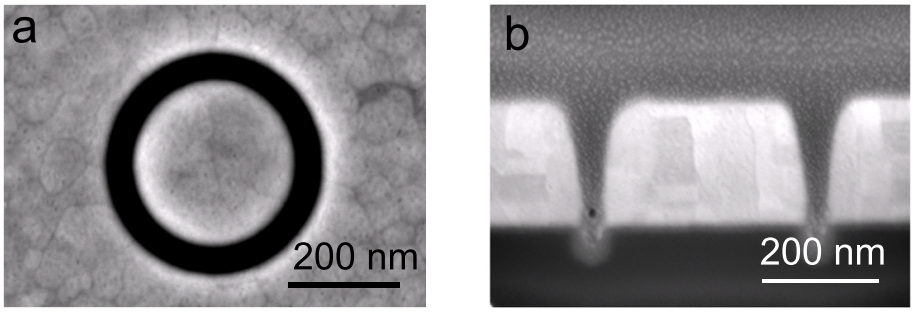

Figure 5.9: SEM images of the fabricated single apertures. (a) Shows a top view and (b) a cross section of a vacuum aperture embedded in gold, where Pt was evaporated to make a better cross section. The outer diameter of the aperture is 400 nm.

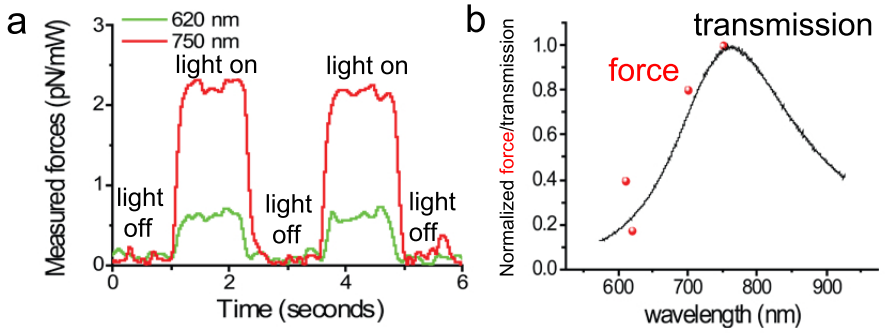

Figure 5.10: Force measurements on single coaxial apertures using an AFM. (a) The tip is positioned at a constant height above a coaxial aperture. The laser is switched on and off several times while the optical force is measured as function of time. (b) Measured force for different wavelengths, together with the measured transmission spectrum of the single aperture. Both the transmission spectrum and the forces are normalized to their maximum.

Figure 5.10(b) shows the measured force, normalized to the maximum measured force, measured at four different wavelengths. We also plot the measured normalized transmission of the measured coaxial aperture. We observe very good agreement with the trends in the force with respect to the transmission spectrum.

Although the trends in the measured forces are in good agreement with the simulations, the absolute measured values are significantly (about ten times) larger than the simulated values. A possible explanation is that heating of both the tip and the sample plays a significant role if laser powers of several mW are used. This will be subject for further research.

5.6 Towards measuring optical forces on coaxial aperture arrays

As discussed in Section 5.3, the optical forces increase significantly if the diameter and channel width of the apertures is decreased. Here, we will show the first steps towards experimentally measuring the optical forces above a hexagonal array of coaxes in Ag with an outer diameter in the range of 100–200 nm and a channel width of 20–30 nm. Here, we use glass apertures instead of air. This would prevent particles or the tip to be attracted into the channels. Furthermore, the higher refractive index of glass enhances the optical forces.

5.6.1 Sample fabrication

Decreasing the ring diameter and wall width to the desired small sizes requires the use of electron beam lithography instead of FIB milling. We use the fabrication method as described in Chapter 2, where we use the negative high resolution resist hydrogen silsesquioxane (HSQ) to infill the channels; it has a refractive index very similar to SiO_2 [36].

We start the fabrication process by writing rings into the HSQ on a SiO_2 substrate with a 30 keV electron beam. The HSQ is developed by two 30 s dips into a 25% solution of tetramethyl ammonium hydroxide (TMAH) solution in water at 50°C, resulting in hollow cylinders of HSQ. Next, gold was evaporated using a technique where the excess of metal was shaved off using an argon ion beam after every 10–15 nm of metal deposition. Lastly the sample surface was polished and the rings were made optically accessible using the FIB under grazing angles. Figure 5.11 shows SEM images of a fabricated coaxial aperture array. We fabricated a variety of outer diameters (100–250 nm), dielectric ring width (15–30 nm) and pitch (200–500 nm).

Due to the FIB polishing step in the above described fabrication method, we have the difficulty that the sample thickness is difficult to determine without making a cross section, and thus destroying the sample. In order to get a feeling of the sample thickness we measured the transmission spectrum of the sample and compared that to the spectrum from FDTD simulations, where different sample thicknesses are simulated. For the simulations we used the experimentally measured aperture dimensions. Figure 5.12 shows the measured transmission spectrum, as well as the simulated spectrum that matches the experimental data best. We find a slab thickness of 150 nm, which is exactly the thickness we aimed for. The broadening observed in the experimental data can be explained by a gradient in the thickness of the aperture field. This is due to the polishing step, and can be in the order of several tens of nm. For comparison, we also show the simulated transmission spectra for a 12.5 nm thicker and thinner metamaterial slab in Figure 5.12.

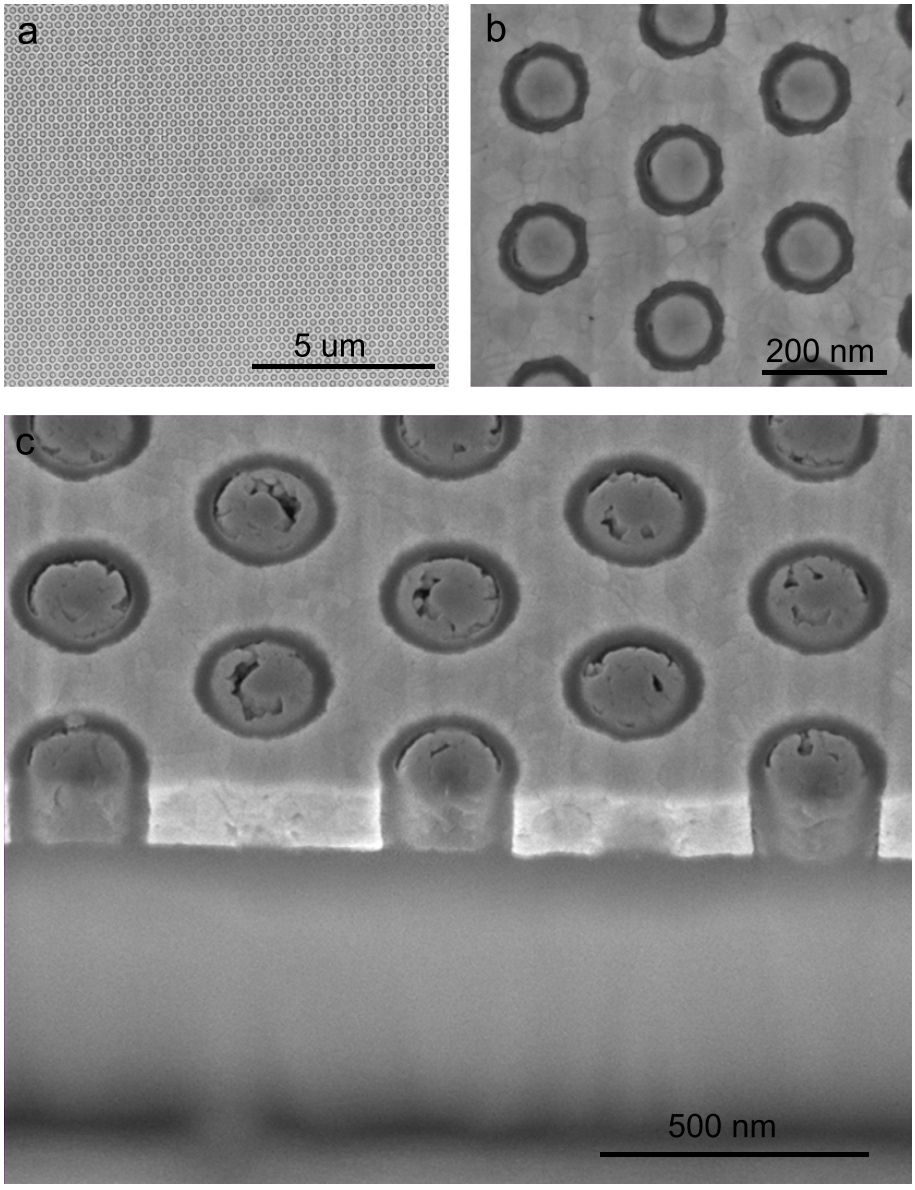

Figure 5.11: SEM images of the fabricated nanoaperture arrays, consisting of HSQ channels embedded in gold. (a,b) Top view and (c) cross section of the sample.

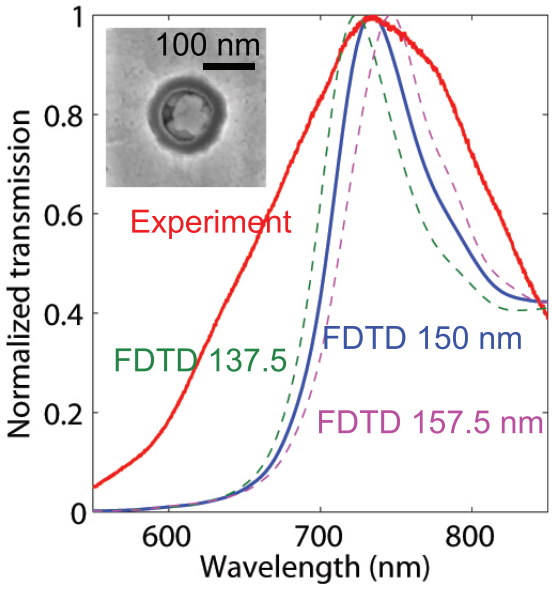

Figure 5.12: Normalized transmission spectra of a hexagonal array of coaxial apertures. The red line was experimentally measured, the other lines represent the spectra of simulated data for slab thicknesses of 137.5 (green dashed line), 157.5 (dashed purple line) and 150 nm (blue solid line). The inset shows a SEM image of the measured sample. The apertures have an inner diameter of 105 nm, an outer diameter of 155 nm and a pitch of 300 nm.

5.6.2 Optical forces on coaxial arrays

Before measuring optical forces on the experimentally fabricated aperture arrays we investigate the expected forces on a small partically numerically. Figure 5.13 shows the simulated electric field intensity and transverse components of the trapping forces using a coaxial array with dimensions as experimentally fabricated. We again observe that the particles will be trapped above the dielectric channels, where the electric field shows an intensity maximum. Also, the forces are in the same order of magnitude as the arrays considered in Section 5.3

In Figure 5.14 shows the measured deflection signal of the AFM tip for excitation wavelengths of $\lambda = 733$ nm, which is at the transmission maximum, and $\lambda = 580$ nm. As for the single arrays, we find a larger tip deflection in case of excitation at the transmission peak wavelength. However, to be able to extract the absolute value of the trapping forces it is crucial to understand thermal effects due to the excitation laser. This is subject of further research.

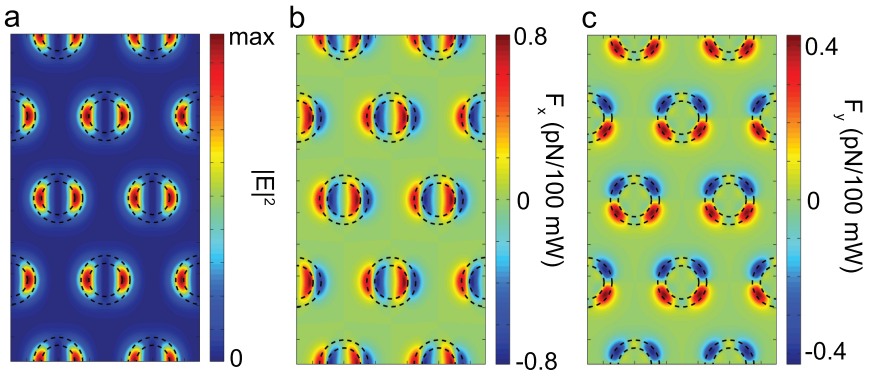

Figure 5.13: (a) Simulated normalized electric field intensity 20 nm from an array of coaxial apertures with dimensions as measured from the fabricated sample (105 and 155 nm inner and outer diameter, respectively, a 300 nm pitch and a slab thickness of 150 nm). (b,c) Transverse components of the optical forces exerted on a 10 nm dielectric particle with $n = 2$ 20 nm away from the apertures. All simulations are performed at the transmission peak wavelength ($\lambda = 733$ nm), and the forces are normalized to 100 mW of transmitted power. We used a plane wave under normal incidence, linearly polarized along the horizontal axis.

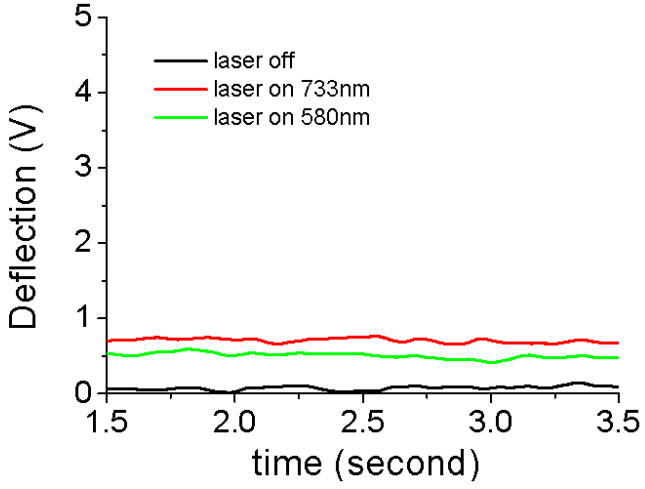

Figure 5.14: Deflection signal of a tip at a constant distance above a coaxial array as function of time. The sample is illuminated from the bottom side, with a wavelength of $\lambda = 733$ and 580 nm.

5.7 Conclusions

In this chapter we investigate the optical trapping forces and potentials for different dielectric cylinders in metal. We show that both apertures in Ag and Au lead to strong trapping forces, enabling stable particle trapping ($U_{xy} > 10kT$/100 mW) with a transmitted optical power of ~ 5.5 mW. Placing the apertures into a hexagonal array does not significantly disturb the optical trapping forces. Furthermore, we investigate the trends of the trapping potential on changing the aperture diameter and channel width. We find that the optimal channel width is a tradeoff between transmission through the channels and field confinement. The largest trapping forces are found for an outer radius of 50–70 nm. After designing the optimum aperture geometry we show the first steps towards experimentally measuring the optical trapping force with an AFM on both single apertures and hexagonal arrays. We fabricated a SiO_2/Au coaxial array with apertures of 155 nm outer diameter and a dielectric wall width of 25 nm. Numerically calculated maximum trapping forces are ~1 pN per 100 mW transmitted power per aperture for the fabricated apertures geometries. The measured forces show wavelength and power dependent trends which match the numerical results. The measured signal is about 10 times larger than the expected forces, suggesting that the measurements are significantly affected by thermal effects.

6

Magnetic and electric dipole modes in hollow Si nanocylinders

We propose a dielectric nanoresonator geometry consisting of hollow dielectric nanocylinders which support Mie-like resonances. We fabricate the hollow Si particles with an outer diameter of 108–251 nm on a Si substrate, and determine their resonant modes with cathodoluminescence (CL) spectroscopy and optical dark-field (DF) scattering measurements. Furthermore, we systematically investigate the scattering behavior as a function of wavelength and particle geometry numerically. We find that the additional design parameter as a result of the introduction of a center gap can be used to control the relative spectral spacing of the resonant modes, which enables additional control over the angular radiation pattern of the scatterers. Furthermore, the gap offers direct access to the enhanced magnetic dipole modal field in the center of the particle.

6.1 Introduction

High-index nanoscale dielectric particles have recently attracted attention because of their ability to strongly confine and scatter light [87, 88] with relatively low absorption losses, in a way that is highly tunable by the particle material and geometry [89]. The ability to concentrate, redirect and manipulate light at the nanoscale

provides the ability to couple and trap light in various applications. Nanoparticles are for example used in solar cells, where they efficiently absorb and preferentially scatter light into the cell [90–95]. Alternatively, dielectric nanoparticles can be used for sensors and photo detectors of which the wavelength and polarization sensitivity can be tuned by the particle geometry [96–98].

Previous work has demonstrated that such nanoscale high-index dielectric particles support magnetic dipole (MD) and electric dipole (ED) resonances in the visible spectral range [89, 99, 100]. Interference between different resonant modes can be used to engineer the angular radiation pattern [101–103], including the case of Kerker-type interference [104], where the scattered light is highly directional and the ratio of forward to backward scattering can be controlled [101–103]. Because of above mentioned properties, these particles can be used as dielectric building-blocks for low-loss metasurfaces [105]. The interference of the MD and ED mode can be controlled by tuning the relative spectral position of the two modes, which can be done by changing the aspect ratio of the scattering particles [100, 103].

Here, we introduce a nanoscale resonant scattering geometry that is composed of hollow dielectric nanocylinders. In this geometry the diameter of the gap provides an additional parameter to control the wavelength and spectral distance of the MD and ED resonant modes. Furthermore, the gap provides direct access to the enhanced magnetic field of the MD mode in the center of the particle, enabling studies of the effect of the magnetic LDOS on spontaneous emission from magnetic dipole emitters [30, 106, 107].

We systematically investigate the behavior of the MD and ED modes upon introducing a center gap into small dielectric Si scatterers. Careful examination of the field profiles inside the particles reveals that the MD mode is very robust when opening a 20–40 nm diameter gap in the center of a 100–150 nm diameter silicon cylinder. We experimentally study the resonant modes of hollow Si particles using cathodoluminescence (CL) spectroscopy and optical dark-field (DF) scattering. We numerically simulate the scattering spectra as a function of particle geometry. The results presented here pave the road towards designing scatterers with a highly tailored radiation pattern.

6.2 Optical modes in a solid dielectric nanoparticle

Before considering hollow scatterers, we will first briefly review the scattering modes in solid dielectric particles. It has been shown that small dielectric scatterers support resonant eigenmodes of which the fields are confined inside the particles, rather than on the surface, as in the case for metallic nanoparticles [89, 99, 108–111]. For spheres and infinitely long cylinders in a homogeneous medium these modes can be found from the analytical Mie solutions to Maxwell's equations [87, 112], whereas for other geometries no exact solutions can be found. These kind of resonances are also referred to as geometrical resonances.

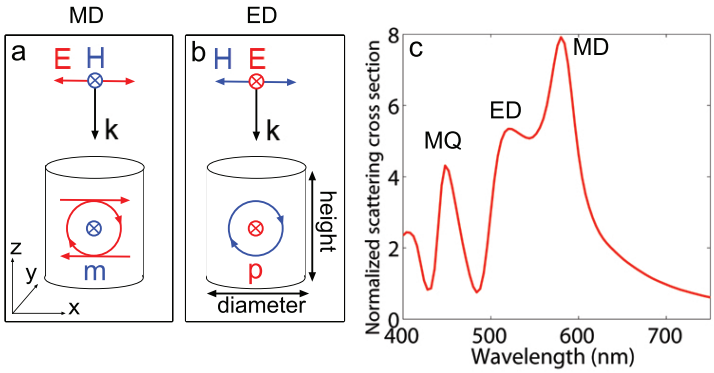

Figure 6.1: Sketch of the MD and ED modes inside a solid dielectric nanoparticle. (a) The MD mode is characterized by a magnetic dipole moment as result of an electrical displacement current loop, indicated by the red circle. (b) The ED mode is the result of collective polarization of the particle material, which induces a magnetic current loop, indicated by the blue circle. The polarization of the corresponding incident plane-wave is sketched above the structures. (c) Numerically simulated scattering cross section of a 100 nm tall Si cylinder with a 150 nm diameter in air. The particle is excited by a plane wave under normal incidence, as shown in (a) and (b).The MD, ED and magnetic quadrupole (MQ) modes are labeled.

The optical modes supported by small dielectric particles can be either magnetic or electric in nature, where the lowest order resonances are the magnetic and electric dipole (MD and ED) modes [89, 99, 100]. The MD mode is characterized by an electric displacement current loop inside the dielectric particle, which induces a magnetic dipole moment orthogonal to the current loop (Figure 6.1(a)). Since a current loop requires opposite orientation of the electric field in the top and the bottom of the particle, this MD mode can only exist in particles with sufficient retardation throughout the particle [89]. Typically, in case of Si particles, 50–100 nm particles are tall enough to couple to the opposing fields at top and bottom of the particle.

The ED mode originates from the collective polarization of the particle material in response to the external driving field. The oscillating ED induces a magnetic current loop. In this case however, the current loop can also extend outside the dielectric particle, enabling the ED mode to exist in particles which are too short to support a MD mode. The reason is that the magnetic permittivity $\mu = 1$ in both the cylinder material and the vacuum surrounding the cylinder. Figure 6.1(b) shows a sketch of the ED mode together with the plane wave that can couple to this mode. High index dielectric particles with a spherical geometry have a well defined modal hierarchy, where the ED mode is found slightly blue shifted with respect to the MD mode [100]. In other geometries the relative position of the two modes can be tuned

by the aspect ratio, which can even be designed such that the modes cross and the ED mode is found at longer wavelengths than the MD mode [103]. Introducing a gap in the center of the resonators results in an additional degree of freedom to design the spectral separation of the MD and ED mode resonances. A typical scattering spectrum of a cylindrical scatterer in air, extracted from a numerical simulation, is shown in Figure 6.1(c). The peak on the red side of the spectrum represents the MD mode position. The ED mode appears as a shoulder on the blue side of this peak. The peak at $\lambda = 450$ nm is characterized as a magnetic quadrupole (MQ) mode [89].

In the remainder of this Chapter, we focus on particles and substrates composed of Si, because of its high refractive index (and thus large mode confinement), relatively low absorption losses in the visible and near-IR, and well-established fabrication processes (see Chapter 2). A cylindrical particle shape is chosen because such a geometry can scatter light effectively [89], can be readily fabricated using electron beam lithography (EBL) and dry etching techniques and the resonant wavelengths can be tuned by changing the aspect ratio. We consider particles which are taller than 100 nm to be sure that the MD mode is effectively supported. Only the lowest order magnetic (MD) and electric (ED) modes are considered in the remainder of this chapter. Since the field profiles of the first order electric mode in cylinders with a gap do not represent an ED mode (see Section 6.6), we refer to this mode as a 'distributed electric (DE) mode'.

6.3 Sample fabrication

We fabricated a sample with different coax geometries on top of a Si substrate using electron beam lithography (EBL) and reactive ion etching (RIE). First we spincoat a thin layer of the negative tone high resolution resist HSQ, for which we use a 1:2 solution of HSQ fox-12:MIBK. Next, circles with the desired outer diameters are written with a 30 keV EBL system using a 10 μm aperture. The gap widths are controlled by changing the dose of the electron beam in the 250–1000 μC/cm^2 range, where an increased dose results in a thicker cylinder wall. After e-beam exposure, the HSQ is developed by dipping the sample two times for 30 seconds in a 25% TMAH solution at 50°C and dried in a critical point dryer, resulting in HSQ cylinders on top of a Si substrate.

Next, the HSQ patterns are transferred into the substrate using an HBr-based RIE, which is known for its anisotropy and high selectivity for Si (for details see Chapter 2). After etching the samples are dipped in a 1% HF solution for 10 minutes to remove the remainders of the HSQ mask. This process results in hollow Si cylinders on a Si substrate, with a varying inner diameter in the range of 20–235 nm and outer diameter in the range of 80–250 nm. Figure 6.2 shows SEM images of the smallest and largest coaxes. Both particles clearly show a cylindrical shape, with only minor tapering due to the highly anisotropic RIE process.

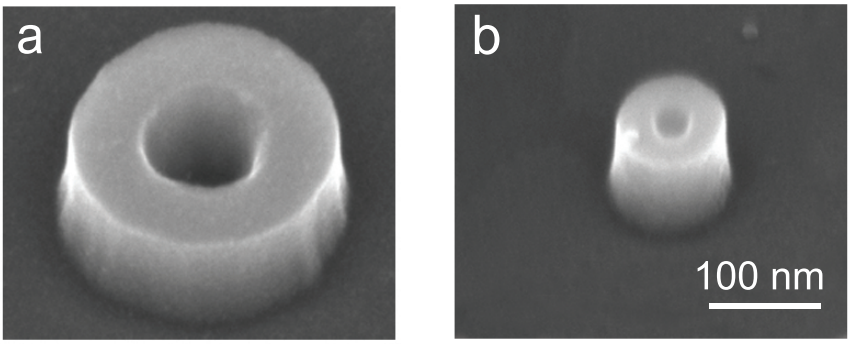

Figure 6.2: SEM images of the (a) largest and (b) smallest Si particle on a Si substrate measured in the CL experiments. The smallest particle has an inner and outer diameter of 20 and 108 nm, and the largest particle of 76 and 251 nm respectively. The scale is the same in both figures.

6.4 Cathodoluminescence spectroscopy

Next, we study the optical scattering spectra of the fabricated cylinders using CL imaging spectroscopy. In CL, a 30 keV electron beam inside an SEM is used to locally excite the sample with a very high spatial resolution. The electric field generated by the electron beam passing through the nanoparticles coherently excites resonant modes supported by the Si nanocylinders. Since CL couples to the out-of-plane component of electric fields, the excitation efficiency is sensitive to the out-of-plane component of the local density of optical states [63, 64]. The excited modes radiate into the far field, and the light is collected by a parabolic mirror placed between the sample and the electron column and directed to a spectrometer. A sketch of the setup is shown in Figure 6.3.

In the experiment the electron beam is raster-scanned in steps of 5 nm over a single cylinder and the spectrum for each pixel is collected. At the same time the secondary electron signal is collected, such that we can match the obtained radiation spectrum with the excitation position on the sample. After correcting for the background, which is measured on an unpatterned Si surface, and the system response, we spatially average the spectrum over all positions of a single ring (including the center area). All spectra are then normalized to their maximum value.

Figure 6.4(a) shows the excitation as function of position on the sample at λ = 500 nm for a coaxial cylinder with an outer diameter of 170 nm and an inner diameter of 71 nm. The corresponding secondary electron image, which was taken simultaneously with the excitation map, is shown in (b). We observe a bright CL ring matching with the outer circumference of the Si ring, and a dark region in the

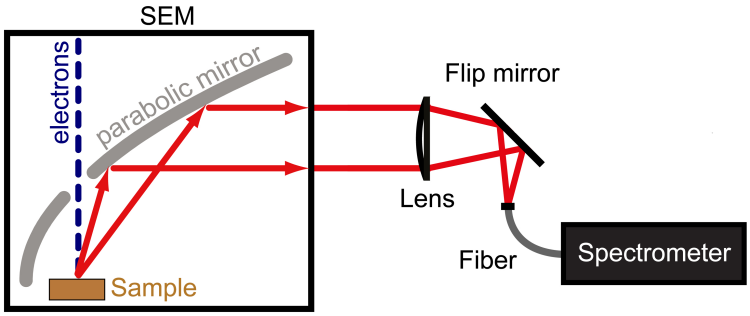

Figure 6.3: Sketch of the setup used for the CL measurements. The sample is excited using a 30 keV electron beam inside a conventional SEM. The emitted light is collected by a parabolic mirror placed between the sample and the electron column and focused on an optical fiber which guides the signal to a spectrometer.

center, at the position of the gap. This pattern is representative for all measured wavelengths and cylinders. The center is dark because the vacuum in the gap is not polarizable by the electron beam. Experimentally measured CL spectra for 122 nm tall particles are shown in (c), where the outer diameter of the ring is systematically increased from 108 to 251 nm. Corresponding SEM images of the smallest and largest measured rings are shown in Figure 6.2(a,b). For all geometries we find clear peaks in the visible part of the spectrum. First, we observe a broad peak on the red side of the spectrum, which red shifts, broadens and decreases in intensity for increasing particle size. Second, we find two sharper peaks at shorter wavelengths, which also red shift and decrease in intensity for larger particle sizes. The red shift for these smaller peaks is less pronounced than for the broad resonance.

We use Finite-Difference Time-Domain (FDTD) simulations to obtain insight into the trends observed in Figure 6.4(c) (see Section 6.5 for details about the simulation setup). Figure 6.4(d) shows the simulated scattering spectra, where the modes are excited with a plane wave under normal incidence and the scattering in all directions is collected. As in the experiments, we find a broad resonance on the red side of the spectrum which shifts to longer wavelengths and decreases in intensity for increasing particle size. For small particle sizes we observe a shoulder on the blue side of the broad resonance, and for larger particles a sharp peak which red shifts at the blue side of the broad resonance. Both the shapes of the observed peaks and trends as function of particle size of the experiments are thus well reproduced by the simulations. Since the simulations match the experiments very well we will investigate the nature of the resonances and the trends as a function of particle dimensions by considering the mode profiles extracted from the simulations in the next sections.

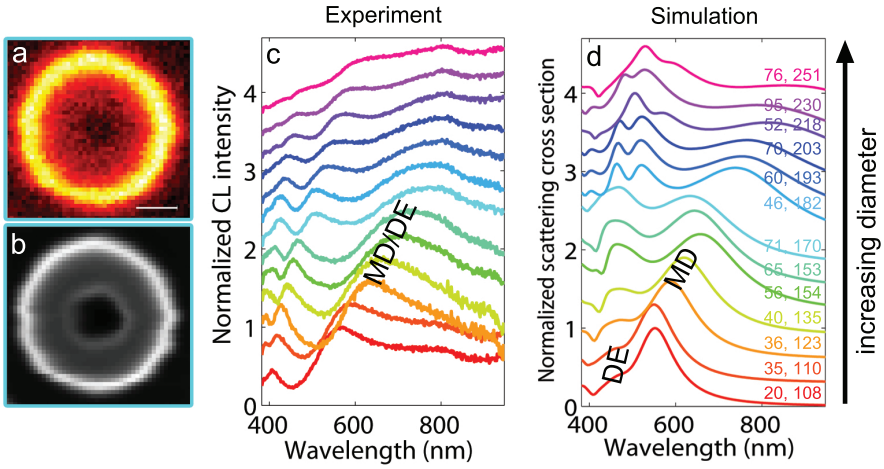

Figure 6.4: CL measurements and FDTD simulations for different cylinder sizes. (a) CL excitation map of a single Si particle with an outer diameter of 170 and an inner diameter of 71 nm at $\lambda = 500$ nm. (b) Secondary electron image taken simultaneously with the CL excitation map. (c) Spatially averaged CL spectra of a Si cylinder with a height of 122 nm, for 13 different coax geometries. The particle inner and outer diameters for each spectrum is indicated by the numbers in (d), where the first number denotes the inner and the second the outer diameter, respectively. (d) FDTD simulation results of the resonant spectra in the visible, excited with a plane wave under normal incidence, using experimentally measured particle dimensions. All spectra are normalized to their maximum value, and vertically offset for clarity.

6.5 FDTD simulation setup

To resolve both the resonance wavelength and the nature of the resonant modes we use Finite-Difference Time-Domain (FDTD) simulations [65]. Depending on which modes we want to excite, the particle is illuminated with a broad-band (400–750 nm) plane wave under normal incidence or at 90° incidence (by rotating the particle around the y-axis). Perfectly matching layers are used at the boundaries to prevent any unphysical backscattering from the simulation box boundaries. A refined mesh is used over the region of the structures with a mesh size of 1–2.5 nm, depending on the dimensions of the cylinder. For the optical constants of Si we use the values determined by Palik [60]; the refractive index of the surroundings is set to 1.

A broad-band total-field scattering-field source is used to excite the sample. Power transmission monitors surrounding the particle selectively measure the power of the scattered light. The normalized scattering cross section Q_{scat} can be calculated from the scattered power, defined as the scattering cross section as measured by the power monitors divided by the area enclosed by the outer

diameter of the particle. The normalization factor is thus insensitive to the size of the air gap inside the particles. The nature of the modes is resolved by using field monitors both inside and outside the particle to detect the electric and magnetic field intensities and associated current loops.

6.6 Modes in Si coaxes surrounded by air

In this section we numerically study the resonances supported by coaxial Si nanoparticles by considering a completely filled cylinder in which we introduce a gap with systematically increasing diameter. Here, we only consider in-plane modes of hollow cylinders in air, which are excited with a plane wave under normal incidence, as shown in the configuration in Figure 6.1.

6.6.1 Simulated scattering cross section

Figure 6.5(a) shows the simulated normalized scattering cross section as function of wavelength for a Si cylinder in air, with a 150 nm outer diameter and a height of 100 nm. The gap width is increased from 0 to 150 nm in steps of 10 nm. Spectra for the case of no gap (solid particle) and gap widths of 40 and 120 nm are shown in Figure 6.5(b), where we find the ED resonance as a shoulder on the blue side of the MD resonance. For larger gap sizes the spectral distance between the two resonances decrease. Clearly, the peak intensities decrease for larger gap sizes.

As the gap inside the solid cylinders is opened, the resonant peaks gradually blue shift as result of the lower effective index experienced by the field inside the particle. The relative spectral position of both modes also changes with gap size. The shifting of the ED mode seems to saturate at a wavelength of ~400 nm and an inner diameter of about 100 nm, whereas the MD mode continues to shift to shorter wavelengths for increasing gap width in the entire diameter range. This behavior is explained in Section 6.6.2. The resonance amplitude decreases gradually for larger gap widths, which is most pronounced for the MD resonance. This is a result of the reduced refractive index contrast as result of the reduced effective index of the particle.

6.6.2 Electric and magnetic field profiles

Next, we resolve the nature of the different modes inside hollow cylindrical Si particles in more detail by exploring their electric and magnetic field profiles. Figure 6.6 shows the time-averaged electric and magnetic field intensities in the xz and yz plane, as defined in Figure 6.1, at the resonance wavelengths for the two lowest order modes, for the same three geometries as considered in Figure 6.5(b). The electric (in case of the MD mode) and magnetic (for the ED mode) field lines are plotted as well in order to identify the corresponding current loops.

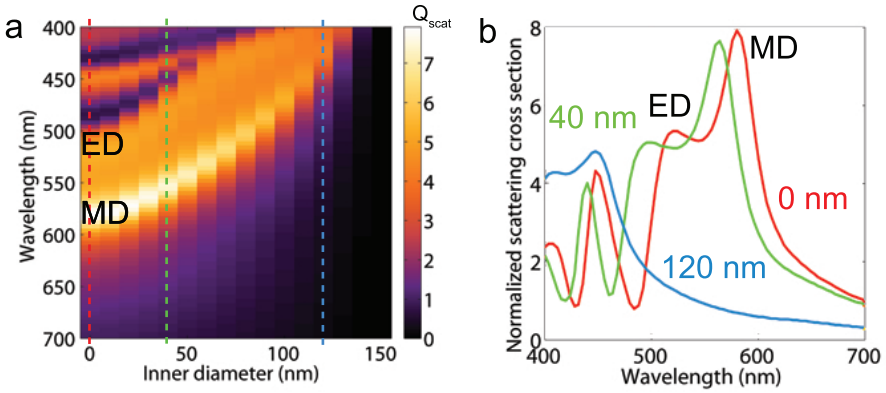

Figure 6.5: Normalized scattering cross section (Q_{scat}) of a 150 nm diameter and 100 nm tall Si cylinder in air as function of wavelength and gap width in the visible wavelength range. The modes were excited with a horizontally polarized plane wave at normal incidence. In (a) the gap (inner) diameter is systematically increased from 0 (no gap) to 150 nm (no wall) in steps of 10 nm. In (b) we plot the scattering cross section as function of wavelength for three different gap sizes (0 (red), 40 (green) and 120 nm (blue)). The MD and ED modes of the particle without a gap are indicated in the spectrum. The cross sections in (b) are indicated by the dashed lines with corresponding color in (a).

First we consider the MD mode of a solid cylinder without gap (a,b). We find the electric displacement current loop characteristic for the MD mode (a) and the associated enhanced magnetic field intensity in the center of the current loop (b) for the most red shifted peak in Figure 6.5(b). Next, we investigate the fields inside the cylinders with a 40 nm diameter gap in the center (c,d). Again we find a clear electric current loop (c) with an enhanced magnetic field at the center of the current loop (d). Although the nature of the mode is still that of a MD mode, we notice several characteristic differences compared to the fields of the particles without a gap; first, the current loop is slightly deformed at the Si/air interfaces resulting in a slightly elongated shape of the magnetic field hot spot. Second, the maximum intensity of the magnetic field is about half the intensity of the enhanced field inside the particle with no gap, as can be seen from the intensity bars in Figure 6.6. This is attributed to the weaker field confinement due to the lower effective refractive index of a particle with a gap.

Interestingly, if we increase the gap size even more (e,f) we can still clearly distinguish an electric current loop (e) which indicates that the electric displacement current loop can bridge a gap as large as 120 nm (the remaining Si wall thickness is just 15 nm). Considering the intensity scale bar in (f) however, we observe that the associated magnetic field intensity is only a small fraction of the enhancement observed in (b), due to the further reduced effective index of the coax.

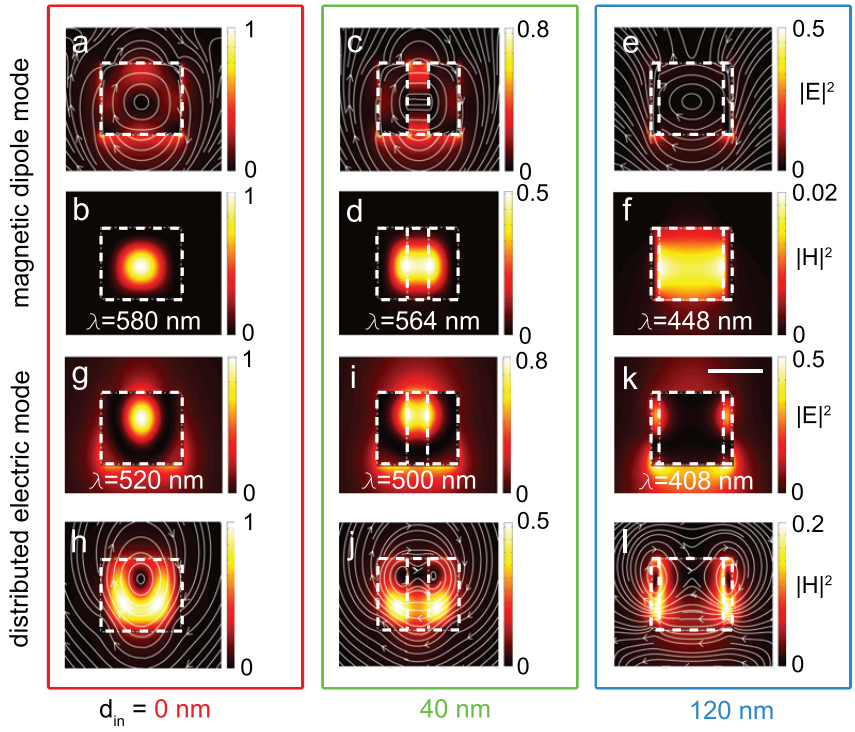

Figure 6.6: Simulated electric and magnetic field profiles inside a Si nanocylinder in air. The normalized field profiles ($|E|^2$ and $|H|^2$) are plotted as cross sections through the center of the particles in the xz (parallel to the electric component of the driving field) (a-f) and yz (parallel to the magnetic component of the driving field) (h-l) planes for three different gap widths, 0, 40 and 120 nm, for the same dimensions as simulated in Figure 6.5 at the wavelengths where the first two maxima in the scattering cross section are found. The peak on the red side of the spectrum is labeled the magnetic dipole, whereas the peak on the blue side of the MD is labeled as DE mode. The lines inside the field plots indicate the electric or magnetic field lines, enabling the recognition of the displacement current loops. All field intensities are normalized to the field intensities found for a solid cylinder without gap. The particle boundaries are plotted as white dashed lines. The scale bar in (k) represents 100 nm.

Next, we consider the ED mode. For the particle without gap we find an enhanced electric field intensity (g) with a magnetic current loop around its center (h) as expected for the ED mode [89]. If we open the gap to 40 nm (i,j), we find two intensity maxima closely spaced next to each other inside the Si ring walls. The magnetic field lines have two centers located at the positions of the electric field maximum. This indicates a coupled electric mode, where the electric field is distributed over both sides of the cylinder walls. For the case where the gap is opened more (k,l), the electric field hot spots are further distributed over the particle walls. In this case the two electric field intensity maxima are so far apart that the electric fields only weakly overlap and no clear dipolar field profile can be recognized. A similar, hybridized, mode is described in two closely spaced dielectric nanoparticles [113]. We will refer to this mode with 'distributed electric (DE) mode' in the remainder of this chapter.

If we now again consider Figure 6.5, we can understand why the DE mode does not shift with the same trends as the MD mode upon changing the inner diameter. Upon opening the gap the mode intensity is decreased less for the DE mode, because most of the electric field remains in the high index material of the particle. In case of the MD mode the electric current loop does extend into the gap of the particle, and is thus less confined due to a lower effective index. The magnetic field is insensitive to the field position with respect to the particle since the magnetic permeability $\mu = 1$ both inside and outside the particle. The saturation of the frequency shift upon changing the gap width of the DE mode, can be explained by the coupling of the two electric hot spots observed in the cylinder walls. For small gap sizes they strongly couple due to their small spacing. In this region the resonance wavelength of this mode is strongly dependent on gap size. At a certain distance, there is a transition from a strongly coupled regime to a weakly coupled regime. In the latter case the coupling is less dependent on the distance between the electrical hot spots, resulting in a saturation of the resonant wavelength shift.

6.7 Influence of a Si substrate on the optical modes

The experimental data in Figure 6.4 show significantly broader peaks than in simulated spectra discussed in Section 6.6. This is caused by the influence of the Si substrate, which is not considered in the simulation. Simulations of the scattering cross section for Si cylinders with the same dimensions as the particles discussed in Figure 6.5 and 6.6, but now on a Si substrate are shown in Figure 6.7. As can be seen for the particle without gap (red line in (b)) the addition of a substrate results in a spectral broadening of the resonances, which causes the MD and ED modes to spectrally overlap, in agreement with the experiment. The broadening is attributed to leakage of the field into the substrate, resulting into increased radiation losses and thereby lower quality factor of the resonant modes [93]. The broadening and spectral overlapping of the ED and MD mode can be tuned by choosing a different refractive index substrate (not shown here). Furthermore, we observe a red shift of

the MD resonance, which is due to the fact that a large fraction of the near-field of the resonant particle is now in the high index substrate.

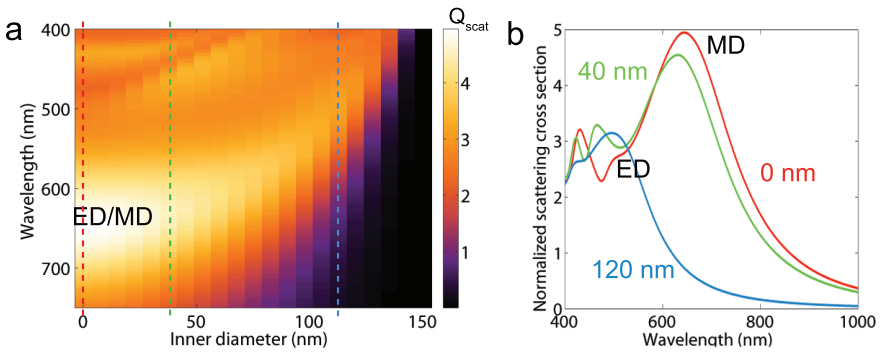

Figure 6.7: Simulated normalized scattering cross section (Q_{scat}) of a 150 nm diameter and 100 nm tall Si cylinder on a Si substrate, as function of wavelength and gap width in the visible wavelength range. The modes were excited with a horizontally polarized plane wave at normal incidence. In (a) the gap (inner) diameter is systematically increased from 0 (no gap) to 150 nm (no wall) in steps of 10 nm. In (b) we plot the scattering cross section as function of wavelength for three different gap sizes (0 (red), 40 (green) and 120 nm (blue)). The peaks indicating the MD and ED resonances for the particle without gap are labeled. The geometries of the spectra in (b) are indicated by the dashed lines with corresponding color in (a).

To demonstrate this, Figure 6.8 shows the fields inside the Si coaxes on a Si substrate, similar to Figure 6.6. Like for the particle in air, we observe an electric displacement current loop with a magnetic field intensity hot spot for the MD mode, and a magnetic current loopt with an enhanced magnetic field intensity for the ED mode, as in Figure 6.6. However, the MD current loops are slightly distorted. For the MD mode the current loops are shifted downwards, in agreement with the spectral broadening of the MD mode due to the extension of the mode profile into the substrate, thereby increasing the resonance linewidth. As a result, the magnetic field hot spot is also shifted into the substrate. This is important when designing an experiment where one would like to use the enhanced magnetic field intensity inside the accessible gap. Unlike for the MD mode, the high field intensity regions of the DE mode are not shifted downwards. The reason is that the in-plane DE mode is less confined in the vertical direction since the magnetic current loop can extend outside the cylinder, regardless of the substrate.

We can now label the modes of the measured resonance peaks in the CL spectra (Figure 6.4(c)). Since CL can excite both the electric current loop of the MD mode and the horizontally polarized DE mode [110], as both modes have out-of-plane electric field components, we identify these modes as the broad peak on the red side of the spectrum. Due to the presence of the substrate, the MD and DE mode

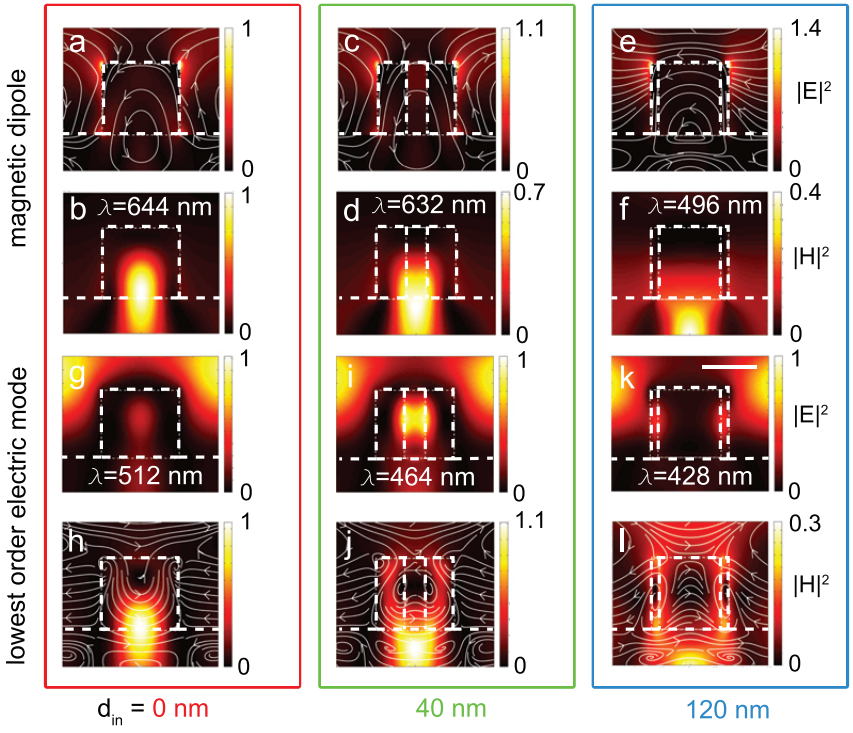

Figure 6.8: Simulated electric and magnetic field profiles inside a Si nanocylinder on a Si substrate. The normalized field profiles ($|E|^2$ and $|H|^2$) are plotted as cross sections through the center of the particles in the xz (parallel to the electric component of the driving field) and yz (parallel to the magnetic component of the driving field) for three different gap widths, for the same dimensions as simulated in Figure 6.7 at the wavelengths where the first two maxima in the scattering cross section are found. The lines inside the field plots show the electric or magnetic field lines, enabling the recognition of the displacement current loops. All field intensities are normalized to the field intensities found for a solid cylinder without a gap. The particle boundaries and substrate surface are plotted as white dashed lines. The scale bar (in k) represents 100 nm.

broaden and overlap. The small peaks on the blue side of the spectra are attributed to higher order modes.

6.8 Dark field spectroscopy

To demonstrate the same resonant behavior under plane wave excitation, rather than electron beam irradiation, we performed DF scattering spectroscopy. The sample is excited under oblique incidence using a 50× 0.8 NA dark-field objective and a halogen lamp, and the light scattered to the top is collected by the objective. As a reference, a Lambertian isotropic scatterer is used. The measured spectra of hollow cylinders with outer diameters in the range of 138–163 nm are shown in Figure 6.9(c). The measured cylinders have almost equal gap sizes.

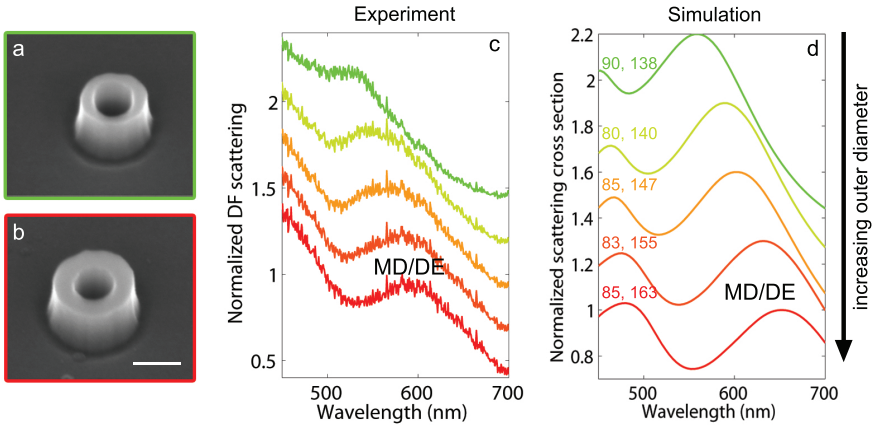

Figure 6.9: DF measurements and FDTD simulations for hollow Si cylinders with different sizes. SEM images of (a) the largest and (b) smallest measured Si particle on a Si substrate. The scale bar represents 100 nm. (c) DF scattering spectra of a Si nanoparticle for 5 different coax geometries. The corresponding inner and outer diameters are given by the numbers indicated in (d), the first number denotes the inner and the second the outer diameter. The cylinders have a height of 138 nm. (d) FDTD simulations of the scattering spectra in the visible spectral range, excited with a plane wave under normal incidence of a coaxial Si particle on a Si substrate. Experimentally measured values for the particle geometries were used for the simulations. All spectra are normalized to the maximum peak value of the MD mode, and vertically offset for clarity.

Similar to Figure 6.4(c), we find a broad resonance peak which red shifts with increased particle size, which is attributed to a decreased effective index of the particle. Figure 6.9(d) shows the simulated scattering cross section for the same sample geometries. The simulations show the same trend as the measurements upon changing the outer diameter, but we observe that the simulated spectra are

red shifted compared to the measured spectra. We attribute this to small tapering of the particles, resulting in a larger diameter on the bottom of the particles. For the simulations we used the dimensions measured on the bottom side of the cylinders.

6.9 Designing optical modes by controlling particle dimensions

The results of the previous sections show that small hollow Si cylinders support both magnetic and electric resonant modes, which can be excited experimentally with both plane waves and an electron beam. In the this section, we will control several design parameters systematically in order to further understand the trends observed in the CL and DF measurements. Furthermore, the results of this section can be used to design experiments for which it is important to control the relative or absolute wavelength of the MD and DE resonant modes.

6.9.1 Optical modes as function of outer diameter with constant gap width

Here, we explore the behavior of the resonant modes upon changing the outer diameter of the resonators, while keeping the gap size constant. Figure 6.10(a) shows the normalized scattering cross section of a 100 nm tall Si particle in air as function of wavelength and outer diameter, while keeping the gap width at a constant value of 40 nm. As expected for geometric resonances, we find a red shift for both the MD and DE mode and higher order modes shifting into the visible spectral range for increasing outer diameters [88]. For increasing particle diameters the spectral separation of the MD and DE mode decreases, overlap, and ultimately these modes cross at infra-red wavelengths outside the investigated wavelength range [103].

6.9.2 MD and ED modes as function of particle height

In Figure 6.10(b) we explore the scattering cross section as function of the height of the hollow Si cylinders in air. We find similar trends as for the solid particles, where both the MD and ED modes are red shifted, the peak intensity is increased, and higher order modes are supported by the resonators upon increased particle height [89]. The red shift is explained by the fact that a larger fraction of the electric displacement current loop can fit inside the high dielectric Si particle for increasing particle height. As seen in Figure 6.10(b) the red shift starts to saturate for particles taller then ~200 nm, which is the result of the current loop now fully fitting inside the particle. If the particle is too short (<50 nm), the current loop does not fit and no MD mode is observed. Since the MD and DE modes do not shift according to the same trends, changing the height and/or outer diameter of the cylinders, enables

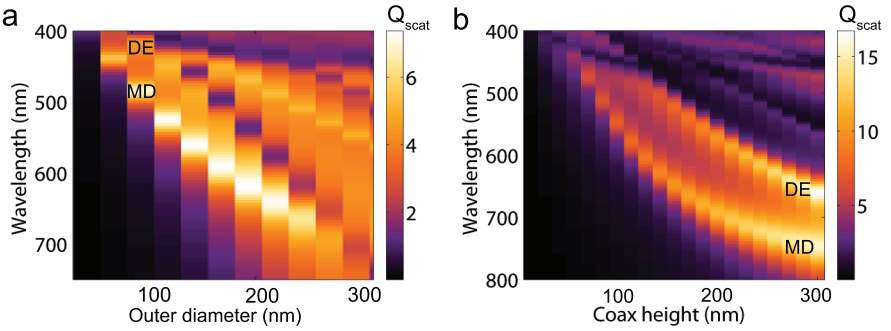

Figure 6.10: Simulated normalized scattering cross section as function of wavelength for different cylinder geometries in air. The rings are excited with a plane wave under normal incidence. In (a) the outer diameter is systematically increased from 40 nm to 300 nm while keeping the height and inner diameter constant at 100 and 40 nm respectively. In (b) the height is systematically increased from 10 to 300 nm while keeping the inner and outer diameter constant at 40 and 150 nm respectively.

control over the spectral distance between the two dipole modes. The increased scattering cross section for increasing coax height is due to the increased volume of the particle, which increases the polarizability.

6.9.3 MD and ED modes as function of outer diameter with constant wall thickness

In Section 6.9.1 we systematically increased the outer diameter while keeping the gap width constant. This results in similar trends as increasing the diameter for solid cylindrical particles without a gap. In this section we explore the modal behavior upon changing the outer diameter while keeping the wall thickness (defined as the outer radius minus the inner radius) at a constant value of 40 nm. The corresponding scattering cross section as function of wavelength and outer diameter is shown in Figure 6.11 where we observe several noticeable trends. For relatively small outer diameters (<150 nm) we observe a red shift of the MD mode for increased outer diameter, which is a result of the reduced confinement due to the larger cavity diameter. Interestingly, it seems that the MD and DE mode cross at an outer diameter of ~320 nm. Careful investigation of the mode profiles (f,g), however, shows that the field profiles at the two resonances present for a 500 nm outer diameter cylinder do not resemble the MD profile as studied before (Figure 6.6(a-f)). Instead, we find a mode profile that represents the DE mode in (f), while the mode profile shown in (g) shows a higher order electric mode, with two displacement current loops in each Si wall. Considering the magnetic field profiles for a cylinder with a diameter where the modes cross (e), we find the profile of a DE

mode.

Since neither of the resonances in Figure 6.11(f,g) are identified as a MD mode, it suggests that this mode cannot exist for large diameter sizes, and we should thus be able to find a transition range where the MD mode dissapears. Indeed, by looking at three closely spaced diameters (b,c,d) we see a gradual deformation of the displacement current loop, until the electric field lines do not form a closed loop and the MD mode disappears. This happens at a particle diameter of ~250 nm, corresponding to a gap width of about ~170 nm.

6.10 Lowest order out-of-plane electric and magnetic modes

For completeness, we also consider the vertically oriented dipolar modes. Figure 6.12 shows the scattering cross section of a Si cylinder in air excited with a plane wave of which the electric field is oriented along the axis of the particle. We observe two resonances, where the resonance on the red side of the spectrum is broader than the one on the blue side. Both resonances blue shift with increasing gap width. The mode on the red side of the spectrum shifts exactly the same way as in Figure 6.5, indicating that this is the in-plane magnetic dipole which can be driven by both a vertically and horizontally polarized plane wave under normal incidence. Indeed, plotting the field profiles inside the particle (not shown here) reveals that this is the in-plane MD. We note that this mode can also be driven in the CL experiments, since the electron beam can couple to the out-of-plane component of this mode.

The nature of the peak on the blue side of the MD resonance is revealed by plotting the corresponding field profiles at the resonant wavelength in the xy plane, as shown in Figure 6.12(b,c). We observe a magnetic current loop and enhanced electric field in the center, indicating an DE oriented along the long axis of the particle.

In Figure 6.13 we explore the scattering behavior upon excitation with a plane wave with the magnetic field oriented along the long axis of the particle (see inset in Figure 6.13(a)). For this polarization we cannot excite the in-plane MD modes as discussed in the former sections. Indeed we find that the resonance on the red part of the spectrum behaves differently upon changing the inner diameter than the MD resonance discussed in Figure 6.5. Investigating the field profiles (b,c) of this mode reveals that this mode is a vertically oriented MD dipole mode, with the displacement current loop in the xy-plane. In Figure 6.13 (a) we see that opening the gap the first 50 nm does not significantly change the MD resonance wavelength. This is explained by the fact that the electric field is mainly positioned on the outer part of the ring, as seen in (b). Opening the gap further does result in distortion of the electric field, and therefore a shift in resonance wavelength. We note that with

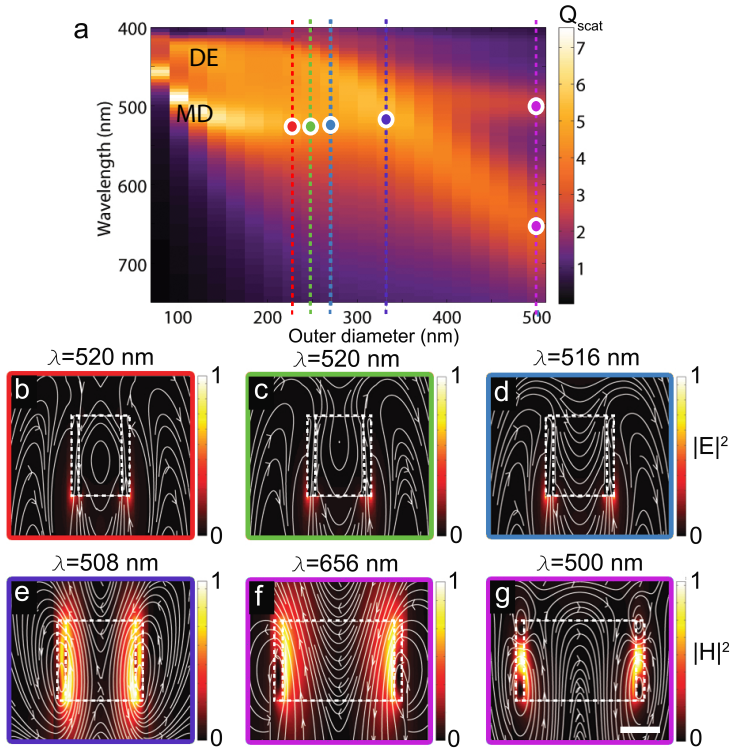

Figure 6.11: Simulated normalized scattering cross section (Q_{scat}) and corresponding mode profiles of a 150 nm diameter Si cylinder on a Si substrate, having a height of 100 nm and a wall thickness of 40 nm as function of wavelength and outer diameter in the visible wavelength range. The modes were excited with a horizontally polarized plane wave at normal incidence. In (a) the outer diameter is systematically increased from 0 (no gap) to 500 nm in steps of 10 nm. (b-d) Show the electric fields with the corresponding magnetic field lines in the xz-plane through the center of the particles, for the wavelengths and outer diameters indicated by the red, green and blue dots in (a), representing an outer diameter of 227, 248 and 269 nm, respectively. (e-g) Show the magnetic field intensity and corresponding electric field lines on resonance are plotted in the yz-plane through the center of the particle, for outer diameters of 332 (crossing point) and 500 nm. The colors of the dashed lines drawn in (a) indicate the geometries of the plotted fields in (b-g). The scale bar in (g) represents 150 nm.

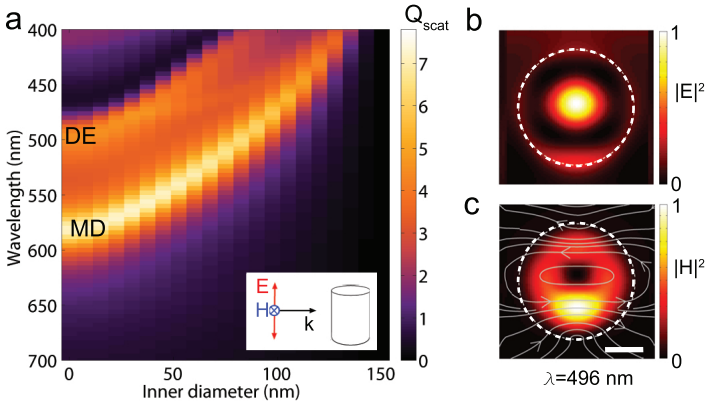

Figure 6.12: Simulated normalized scattering cross section (Q_{scat}) of a 150 nm diameter and 100 nm tall Si cylinder in air, as function of wavelength and gap width in the visible wavelength range. The modes were excited with a vertically polarized plane wave (with the E-field along the long axis of the particle), as seen in the inset of (a). The normalized electric (b) and magnetic (c) field intensity profiles for a solid particle with no gap with the corresponding electric field lines are shown for the xy-plane in the center of the particle on resonance, where the particle contour is plotted as white dashed lines. The field intensities are normalized to its maximum values. The scale bar in (c) represents 50 nm.

oblique incident angles as used in the DF scattering experiment, this out-of-plane MD mode may be excited. However, the excitation efficiency is much lower than for the in-plane MD mode [113].

On the blue side of the MD in Figure 6.13 we observe an in-plane DE mode which has the same scattering behavior as in Figure 6.5, as confirmed by investigating the field profiles (not shown here).

6.11 Designing a scatterer to enhance the MD transition in Eu^{3+}

Since we explored all lowest order magnetic and electric resonances which can be excited inside small cylindrical scatterers in the previous sections, we will use this information to design the optimal scatterer geometry in order to interact with the MD transition of an emitter. We use Eu^{3+} as an example, which has a MD transition at $\lambda = 590$ nm. From Figure 6.5 we realized that opening the gap results in a blue shift of the MD mode, however it also results in a reduced magnetic field intensity. Therefore we will consider a gap size which is as small as possible, but large enough to fabricate and to successfully place a nanoparticle inside. We found that a gap size diameter of ~40 nm is feasible to fabricate reproducibly, so we assume this value

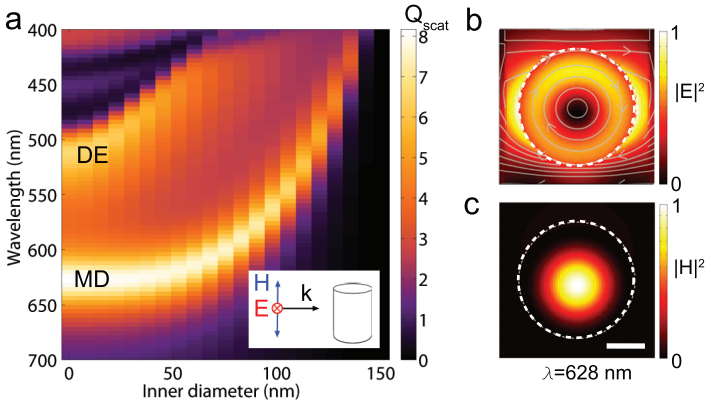

Figure 6.13: Simulated normalized scattering cross section (Q_{scat}) of a 150 nm diameter, 100 nm tall Si cylinder in air, as function of wavelength and gap width in the visible wavelength range. The modes were excited with a vertically polarized plane wave (with the H-field along the long axis of the particle), as seen in the inset of (a). The electric (b) and magnetic (c) field intensity profiles at $\lambda = 628$ nm, for a particle without gap with the corresponding electric field lines are shown for the xy-plane in the center of the particle, where the particle contour is plotted as white dashed lines and the fields are normalized to the maximum. The scale bar represents 50 nm.

for the inner diameter. From Figure 6.10(a) we conclude that an outer diameter in the 100–200 nm range results in the strongest scattering amplitudes, but particles with a diameter larger than ~150 nm have a resonance wavelength which is too far red shifted. Furthermore, increasing the height (Figure 6.10(b)) results in a red shift of the MD resonance as well as an increased scattering strength. Lastly, we need to take into account the red shift of the resonances due to the influence of a substrate, which is in the order of $\lambda = 50$ nm in the considered geometry range. Taking all these factors into account, for an optimal interaction of the MD mode of the scatterer with the MD transition in Eu^{3+}, we propose a Si particle on a Si substrate with an inner diameter of ~40 nm, an outer diameter of 100–150 nm and a particle height of 100–150 nm (depending on the used outer diameter). The measured spectrum of the second smallest particle in the CL experiment shown in Figure 6.4 is for a particle very close to these dimensions, indeed showing a resonance wavelength of $\lambda = 590$ nm.

6.12 Conclusions

We systematically explored the geometrical optical resonances supported by hollow Si nanocylinders. We show that introducing a gap in the center of a 100–250 nm outer diameter silicon cylinder results in only small deviations from the well known

ED and MD geometrical resonances of solid cylinders, where the nature of the MD mode is preserved up to gap widths as large as 190 nm for a wall thickness of just 40 nm. The resonant modes are measured using CL spectroscopy and DF scattering spectroscopy. Using numerical simulations, we show how the resonant wavelength can be controlled by changing the outer diameter, height and gap size of the particles. We find that the gap size can be used as additional parameter to tune the relative spectral spacing between the ED and MD modes. Furthermore, we show that the introduction of a Si substrate significantly broadens the resonances and influences the position of the magnetic field intensity hotspot of the MD mode. We investigate the trends upon changing the cylinder geometry with CL spectroscopy, DF scattering measurements and FDTD simulations. Systematic variation of the geometry of the scatterers shows that the resonances can be designed such that the MD or DE mode matches the MD transition in Eu^{3+}.

References

[1] T. H. Maiman, *Stimulated Optical Radiation in Ruby*, Nature **187**, 493 (1960).

[2] E. Abbe, *Beiträge zur Theorie des Mikroskops und der mikroskopischen Wahrnehmung*, Archiv für mikroskopische Anatomie **9**, 413 (1873).

[3] D. A. B. Miller, *Optics for low-energy communication inside digital processors: quantum detectors, sources, and modulators as efficient impedance converters*, Optics Letters **14**, 146 (1989).

[4] R. Maas, J. Parsons, N. Engheta, and A. Polman, *Experimental realization of an epsilon-near-zero metamaterial at visible wavelengths*, Nature Photon **7**, 907 (2013).

[5] V. G. Veselago, *The electrodynamics of substances with simultaneously negative values of ϵ and μ*, Soviet Physics Uspekhi **10**, 509 (1968).

[6] J. B. Pendry, *Negative Refraction Makes a Perfect Lens*, Physical Review Letters **85**, 3966 (2000).

[7] J. B. Pendry, D. Schurig, and D. R. Smith, *Controlling Electromagnetic Fields*, Science **312**, 1780 (2006).

[8] B. Edwards, A. Alù, M. G. Silveirinha, and N. Engheta, *Experimental Verification of Plasmonic Cloaking at Microwave Frequencies with Metamaterials*, Physical Review Letters **103**, 153901 (2009).

[9] H. Chen, C. T. Chan, and P. Sheng, *Transformation optics and metamaterials*, Nature Materials **9**, 387 (2010).

[10] R. A. Shelby, D. R. Smith, and S. Schultz, *Experimental Verification of a Negative Index of Refraction*, Science **292**, 77 (2001).

[11] J. Valentine, S. Zhang, T. Zentgraf, E. Ulin-Avila, D. A. Genov, G. Bartal, and X. Zhang, *Three-dimensional optical metamaterial with a negative refractive index*, Nature **455**, 376 (2008).

[12] G. Dolling, M. Wegener, C. M. Soukoulis, and S. Linden, *Negative-index metamaterial at 780 nm wavelength*, Optics Letters **32**, 53 (2007).

[13] C. Rockstuhl, T. Zentgraf, H. Guo, N. Liu, C. Etrich, I. Loa, K. Syassen, J. Kuhl, F. Lederer, and H. Giessen, *Resonances of split-ring resonator metamaterials in the near infrared*, Applied Physics B **84**, 219 (2006).

[14] N. Liu, H. Guo, L. Fu, S. Kaiser, H. Schweizer, and H. Giessen, *Three-dimensional photonic metamaterials at optical frequencies*, Nature Materials **7**, 31 (2008).

[15] C. M. Soukoulis, S. Linden, and M. Wegener, *Negative Refractive Index at Optical Wavelengths*, Science **315**, 47 (2007).

[16] D. Pines, *Collective Energy Losses in Solids*, Reviews of Modern Physics **28**, 184 (1956).

[17] R. H. Ritchie, *Plasma Losses by Fast Electrons in Thin Films*, Physical Review **106**, 874 (1957).

[18] J. J. Hopfield, *Theory of the Contribution of Excitons to the Complex Dielectric Constant of Crystals*, Physical Review **112**, 1555 (1958).

[19] R. H. Ritchie, E. T. Arakawa, J. J. Cowan, and R. N. Hamm, *Surface-Plasmon Resonance Effect in Grating Diffraction*, Physical Review Letters **21**, 1530 (1968).

[20] U. Kreibig and P. Zacharias, *Surface plasma resonances in small spherical silver and gold particles*, Zeitschrift für Physik **231**, 128 (1970).

[21] S. L. Cunningham, A. A. Maradudin, and R. F. Wallis, *Effect of a charge layer on the surface-plasmon-polariton dispersion curve*, Physical Review B **10**, 3342 (1974).

[22] A. Otto, *Excitation of nonradiative surface plasma waves in silver by the method of frustrated total reflection*, Zeitschrift für Physik **216**, 398 (1968).

[23] W. L. Barnes, A. Dereux, and T. W. Ebbesen, *Surface plasmon subwavelength optics*, Nature **424**, 824 (2003).

[24] P. Tournois and V. Laude, *Negative group velocities in metal-film optical waveguides*, Optics Communications **137**, 41 (1997).

[25] E. N. Economou, *Surface Plasmons in Thin Films*, Physical Review **182**, 539 (1969).

[26] H. Raether, *Surface Plasmons on Smooth and Rough Surfaces and on Gratings*, Springer-Verlag, Berlin, 1988.

[27] J. A. Dionne, L. A. Sweatlock, H. A. Atwater, and A. Polman, *Planar metal plasmon waveguides: frequency-dependent dispersion, propagation, localization, and loss beyond the free electron model*, Physical Review B **72**, 075405 (2005).

[28] J. A. Dionne, L. A. Sweatlock, H. A. Atwater, and A. Polman, *Plasmon slot waveguides: Towards chip-scale propagation with subwavelength-scale localization*, Physical Review B **73**, 035407 (2006).

[29] A. Lagendijk and B. A. van Tiggelen, *Resonant multiple scattering of light*, Physics Reports **270**, 143 (1996).

[30] R. Zia, M. D. Selker, P. B. Catrysse, and M. L. Brongersma, *Geometries and materials for subwavelength surface plasmon modes*, Journal of the Optical Society of America A **21**, 2442 (2004).

[31] E. Verhagen, R. de Waele, L. Kuipers, and A. Polman, *Three-Dimensional Negative Index of Refraction at Optical Frequencies by Coupling Plasmonic Waveguides*, Physical Review Letters **105**, 223901 (2010).

[32] R. de Waele, S. P. Burgos, H. A. Atwater, and A. Polman, *Negative refractive index in coaxial plasmon waveguides*, Optics Express **18**, 12770 (2010).

[33] S. P. Burgos, R. de Waele, A. Polman, and H. A. Atwater, *A single-layer wide-angle negative-index metamaterial at visible frequencies*, Nature Materials **9**, 407 (2010).

[34] R. Maas, E. Verhagen, J. Parsons, and A. Polman, *Negative Refractive Index and Higher-Order Harmonics in Layered Metallodielectric Optical Metamaterials*, ACS Photonics **1**, 670 (2014).

[35] J. A. Dionne, E. Verhagen, A. Polman, and H. A. Atwater, *Are negative index materials achievable with surface plasmon waveguides? A case study of three plasmonic geometries*, Optics Express **16**, 19001 (2008).

[36] M. Peuker, M. H. Lim, H. I. Smith, R. Morton, A. K. van Langen-Suurling, J. Romijn, E. W. J. M. van der Drift, and F. C. M. J. M. van Delft, *Hydrogen SilsesQuioxane, a high-resolution negative tone e-beam resist, investigated for its applicability in photon-based lithographies*, Microelectronic Engineering **61-62**, 803 (2002).

[37] N. Yahya, *Carbon and Oxide Nanostructures: Synthesis, Characterisation and*

Applications, Springer, 2010.

[38] A. E. Grigorescu and C. W. Hagen, *Resists for sub-20-nm electron beam lithography with a focus on HSQ: state of the art*, Nanotechnology **20**, 292001 (2009).

[39] C. L. Frye and W. T. Collins, *Oligomeric silsesquioxanes, (HSiO3/2)n*, Journal of the American Chemical Society **92**, 5586 (1970).

[40] S. Choi, N. Jin, V. Kumar, I. Adesida, and M. Shannon, *Effects of developer temperature on electron-beam-exposed hydrogen silsesquioxane resist for ultradense silicon nanowire fabrication*, Journal of Vacuum Science & Technology B **25**, 2085 (2007).

[41] F. C. M. J. M. van Delft, *Delay-time and aging effects on contrast and sensitivity of hydrogen silsesquioxane*, Journal of Vacuum Science & Technology B **20**, 2932 (2002).

[42] Y. Chen, H. Yang, and Z. Cui, *Effects of developing conditions on the contrast and sensitivity of hydrogen silsesquioxane*, Microelectronic Engineering **83**, 1119 (2006).

[43] F. Fruleux-Cornu, J. Penaud, E. Dubois, M. François, and M. Muller, *An optimal high contrast e-beam lithography process for the patterning of dense fin networks*, Materials Science and Engineering: C **26**, 893 (2006).

[44] Y. Georgiev, W. Henschel, A. Fuchs, and H. Kurz, *Surface roughness of hydrogen silsesquioxane as a negative tone electron beam resist*, Vacuum **77**, 117 (2005).

[45] N. Clark, A. Vanderslice, R. Grove, and R. R. Krchnavek, *Time-dependent exposure dose of hydrogen silsesquioxane when used as a negative electron-beam resist*, Journal of Vacuum Science & Technology B **24**, 3073 (2006).

[46] H. F. Winters and J. W. Coburn, *Surface science aspects of etching reactions*, Surface Science Reports **14**, 162 (1992).

[47] Z. Cui, *Nanofabrication: Principles, Capabilities, and Limits*, Springer Science, 2008.

[48] R. Legtenberg, H. Jansen, M. de Boer, and M. Elwenspoek, *Anisotropic Reactive Ion Etching of Silicon Using SF_6 / O_2 / CHF_3 Gas Mixtures*, Journal of The Electrochemical Society **142**, 2020 (1995).

[49] S. Grigoropoulos, E. Gogolides, A. D. Tserepi, and A. G. Nassiopoulos, *Highly anisotropic silicon reactive ion etching for nanofabrication using mixtures of SF_6/CHF_3 gases*, Journal of Vacuum Science & Technology B **15**, 640 (1997).

[50] E. Gogolides, S. Grigoropoulos, and A. G. Nassiopoulos, *Highly anisotropic room-temperature sub-half-micron Si reactive ion etching using fluorine only containing gases*, Microelectronic Engineering **27**, 449 (1995).

[51] V. Gianneta, A. Olziersky, and A. Nassiopoulou, *Si nanopatterning by reactive ion etching through an on-chip self-assembled porous anodic alumina mask*, Nanoscale Research Letters **8**, 71 (2013).

[52] H. Jansen, H. Gardeniers, M. d. Boer, M. Elwenspoek, and J. Fluitman, *A survey on the reactive ion etching of silicon in microtechnology*, Journal of Micromechanics and Microengineering **6**, 14 (1996).

[53] R. d´Agostino and D. L. Flamm, *Plasma etching of Si and SiO_2 in SF_6–O_2 mixtures*, Journal of Applied Physics **52**, 162 (1981).

[54] V. M. Donnelly and A. Kornblit, *Plasma etching: Yesterday, today, and tomorrow*, Journal of Vacuum Science & Technology A **31**, 050825 (2013).

[55] D. L. Olynick, J. A. Liddle, and I. W. Rangelow, *Profile evolution of Cr masked features undergoing HBr-inductively coupled plasma etching for use in 25 nm silicon nanoimprint templates*, Journal of Vacuum Science & Technology B **23**, 2073 (2005).

[56] Walker, Z. H., Ogryzlo, and E. A., *Rate constants for the etching of intrinsic and doped polycrystalline silicon by bromine atoms*, volume 69, American Institute of Physics,

Melville, NY, ETATS-UNIS, 1991.

[57] D. L. Olynick, J. A. Liddle, B. D. Harteneck, S. Cabrini, and I. W. Rangelow, *Nanoscale pattern transfer for templates, NEMS, and nano-optics*, volume 6462, pages 64620J–64620J–8, 10.1117/12.705033.

[58] S. Bouchoule, G. Patriarche, S. Guilet, L. Gatilova, L. Largeau, and P. Chabert, *Sidewall passivation assisted by a silicon coverplate during Cl_2–H_2 and HBr inductively coupled plasma etching of InP for photonic devices*, Journal of Vacuum Science & Technology B **26**, 666 (2008).

[59] R. Sainidou and F. J. Garcia de Abajo, *Plasmon guided modes in nanoparticle metamaterials*, Optics Express **16**, 4499 (2008).

[60] E. Palik, *Handbook of Optical Constants of Solids*, Academic, 1985.

[61] P. B. Johnson and R. W. Christy, *Optical Constants of the Noble Metals*, Physical Review B **6**, 4370 (1972).

[62] S. Foteinopoulou, E. N. Economou, and C. M. Soukoulis, *Refraction in Media with a Negative Refractive Index*, Physical Review Letters **90**, 107402 (2003).

[63] F. J. García de Abajo, *Optical excitations in electron microscopy*, Reviews of Modern Physics **82**, 209 (2010).

[64] R. Sapienza, T. Coenen, J. Renger, M. Kuttge, N. F. van Hulst, and A. Polman, *Deep-subwavelength imaging of the modal dispersion of light*, Nature Materials **11**, 781 (2012).

[65] *Lumerical Solutions, Inc.*

[66] T. Paul, C. Menzel, W. Śmigaj, C. Rockstuhl, P. Lalanne, and F. Lederer, *Reflection and transmission of light at periodic layered metamaterial films*, Physical Review B **84**, 115142 (2011).

[67] E. J. R. Vesseur, F. J. García de Abajo, and A. Polman, *Modal Decomposition of Surface–Plasmon Whispering Gallery Resonators*, Nano Letters **9**, 3147 (2009).

[68] E. J. R. Vesseur, F. J. G. de Abajo, and A. Polman, *Broadband Purcell enhancement in plasmonic ring cavities*, Physical Review B **82**, 165419 (2010).

[69] T. Xu, A. Agrawal, M. Abashin, K. J. Chau, and H. J. Lezec, *All-angle negative refraction and active flat lensing of ultraviolet light*, Nature **497**, 470 (2013).

[70] A. Ashkin, J. M. Dziedzic, J. E. Bjorkholm, and S. Chu, *Observation of a single-beam gradient force optical trap for dielectric particles*, Optics Letters **11**, 288 (1986).

[71] K. Dholakia, P. Reece, and M. Gu, *Optical micromanipulation*, Chemical Society Reviews **37**, 42 (2008).

[72] A. Ashkin and J. Dziedzic, *Optical trapping and manipulation of viruses and bacteria*, Science **235**, 1517 (1987).

[73] P. J. Reece, W. J. Toe, F. Wang, S. Paiman, Q. Gao, H. H. Tan, and C. Jagadish, *Characterization of Semiconductor Nanowires Using Optical Tweezers*, Nano Letters **11**, 2375 (2011).

[74] C. W. Twombly, J. S. Evans, and I. I. Smalyukh, *Optical manipulation of self-aligned graphene flakes in liquid crystals*, Optics Express **21**, 1324 (2013).

[75] P. W. Smith, A. Ashkin, and W. J. Tomlinson, *Four-wave mixing in an artificial Kerr medium*, Optics Letters **6**, 284 (1981).

[76] M. T. Woodside, W. M. Behnke-Parks, K. Larizadeh, K. Travers, D. Herschlag, and S. M. Block, *Nanomechanical measurements of the sequence-dependent folding landscapes of single nucleic acid hairpins*, Proceedings of the National Academy of Sciences **103**, 6190 (2006).

[77] J.-D. Kim and Y.-G. Lee, *Trapping of a single DNA molecule using nanoplasmonic*

structures for biosensor applications, Biomedical Optics Express **5**, 2471 (2014).

[78] A. Kotnala and R. Gordon, *Quantification of High-Efficiency Trapping of Nanoparticles in a Double Nanohole Optical Tweezer*, Nano Letters **14**, 853 (2014).

[79] J. Sancho-Parramon and S. Bosch, *Optical forces induced by metal nanoparticle clusters*, Applied Physics A **115**, 393 (2014).

[80] N. M. Hameed, A. El Eter, T. Grosjean, and F. I. Baida, *Stand-Alone Three-Dimensional Optical Tweezers Based on Fibred Bowtie Nanoaperture*, Photonics Journal, IEEE **6**, 1 (2014).

[81] A. A. E. Saleh and J. A. Dionne, *Toward Efficient Optical Trapping of Sub-10-nm Particles with Coaxial Plasmonic Apertures*, Nano Letters **12**, 5581 (2012).

[82] M. Dienerowitz, M. Mazilu, and K. Dholakia, *Optical manipulation of nanoparticles: a review*, Journal of Nanophotonics **2**, 021875 (2008).

[83] J. D. Jackson, *Classical Electrodynamics, 3rd Ed.*, John Wiley & Sons, Inc., 1999.

[84] Y. Harada and T. Asakura, *Radiation forces on a dielectric sphere in the Rayleigh scattering regime*, Optics Communications **124**, 529 (1996).

[85] L. Novotny, R. X. Bian, and X. S. Xie, *Theory of Nanometric Optical Tweezers*, Physical Review Letters **79**, 645 (1997).

[86] A. H. J. Yang, T. Lerdsuchatawanich, and D. Erickson, *Forces and Transport Velocities for a Particle in a Slot Waveguide*, Nano Letters **9**, 1182 (2009).

[87] C. F. Bohren and D. R. Huffman, *Absorption and Scattering of Light by Small Particles*, Wiley-VCH Verlag GmbH, 1983.

[88] J. A. Schuller and M. L. Brongersma, *General properties of dielectric optical antennas*, Optics Express **17**, 24084 (2009).

[89] J. van de Groep and A. Polman, *Designing dielectric resonators on substrates: Combining magnetic and electric resonances*, Optics Express **21**, 26285 (2013).

[90] J. Grandidier, D. M. Callahan, J. N. Munday, and H. A. Atwater, *Light Absorption Enhancement in Thin-Film Solar Cells Using Whispering Gallery Modes in Dielectric Nanospheres*, Advanced Materials **23**, 1272 (2011).

[91] A. Raman, Z. Yu, and S. Fan, *Dielectric nanostructures for broadband light trapping in organic solar cells*, Optics Express **19**, 19015 (2011).

[92] S. A. Mann, R. R. Grote, R. M. Osgood, and J. A. Schuller, *Dielectric particle and void resonators for thin film solar cell textures*, Optics Express **19**, 25729 (2011).

[93] P. Spinelli, M. A. Verschuuren, and A. Polman, *Broadband omnidirectional antireflection coating based on subwavelength surface Mie resonators*, Nature Communications **3**, 692 (2012).

[94] A. P. Vasudev, J. A. Schuller, and M. L. Brongersma, *Nanophotonic light trapping with patterned transparent conductive oxides*, Optics Express **20**, A385 (2012).

[95] C. van Lare, F. Lenzmann, M. A. Verschuuren, and A. Polman, *Dielectric Scattering Patterns for Efficient Light Trapping in Thin-Film Solar Cells*, Nano Letters **15**, 4846 (2015).

[96] L. Cao, J. S. White, J.-S. Park, J. A. Schuller, B. M. Clemens, and M. L. Brongersma, *Engineering light absorption in semiconductor nanowire devices*, Nature Materials **8**, 643 (2009).

[97] L. Cao, J.-S. Park, P. Fan, B. Clemens, and M. L. Brongersma, *Resonant Germanium Nanoantenna Photodetectors*, Nano Letters **10**, 1229 (2010).

[98] R. Yan, J.-H. Park, Y. Choi, C.-J. Heo, S.-M. Yang, L. P. Lee, and P. Yang, *Nanowire-based single-cell endoscopy*, Nature Nano **7**, 191 (2012).

[99] A. García-Etxarri, R. Gómez-Medina, L. S. Froufe-Pérez, C. López, L. Chantada,

F. Scheffold, J. Aizpurua, M. Nieto-Vesperinas, and J. J. Sáenz, *Strong magnetic response of submicron Silicon particles in the infrared*, Optics Express **19**, 4815 (2011).

[100] A. B. Evlyukhin, C. Reinhardt, A. Seidel, B. S. Luk´yanchuk, and B. N. Chichkov, *Optical response features of Si-nanoparticle arrays*, Physical Review B **82**, 045404 (2010).

[101] Y. H. Fu, A. I. Kuznetsov, A. E. Miroshnichenko, Y. F. Yu, and B. Luk´yanchuk, *Directional visible light scattering by silicon nanoparticles*, Nature Communications **4**, 1527 (2013).

[102] S. Person, M. Jain, Z. Lapin, J. J. Sáenz, G. Wicks, and L. Novotny, *Demonstration of Zero Optical Backscattering from Single Nanoparticles*, Nano Letters **13**, 1806 (2013).

[103] I. Staude, A. E. Miroshnichenko, M. Decker, N. T. Fofang, S. Liu, E. Gonzales, J. Dominguez, T. S. Luk, D. N. Neshev, I. Brener, and Y. Kivshar, *Tailoring Directional Scattering through Magnetic and Electric Resonances in Subwavelength Silicon Nanodisks*, ACS Nano **7**, 7824 (2013).

[104] M. Kerker, D. S. Wang, and C. L. Giles, *Electromagnetic scattering by magnetic spheres*, Journal of the Optical Society of America **73**, 765 (1983).

[105] P. P. Iyer, N. A. Butakov, and J. A. Schuller, *Reconfigurable Semiconductor Phased-Array Metasurfaces*, ACS Photonics **2**, 1077 (2015).

[106] S. Karaveli and R. Zia, *Strong enhancement of magnetic dipole emission in a multilevel electronic system*, Optics Letters **35**, 3318 (2010).

[107] B. Rolly, B. Bebey, S. Bidault, B. Stout, and N. Bonod, *Promoting magnetic dipolar transition in trivalent lanthanide ions with lossless Mie resonances*, Physical Review B **85**, 245432 (2012).

[108] A. B. Evlyukhin, S. M. Novikov, U. Zywietz, R. L. Eriksen, C. Reinhardt, S. I. Bozhevolnyi, and B. N. Chichkov, *Demonstration of Magnetic Dipole Resonances of Dielectric Nanospheres in the Visible Region*, Nano Letters **12**, 3749 (2012).

[109] A. I. Kuznetsov, A. E. Miroshnichenko, Y. H. Fu, J. Zhang, and B. Luk´yanchuk, *Magnetic light*, Scientific Reports **2**, 492 (2012).

[110] T. Coenen, J. van de Groep, and A. Polman, *Resonant Modes of Single Silicon Nanocavities Excited by Electron Irradiation*, ACS Nano **7**, 1689 (2013).

[111] L. Huang, Y. Yu, and L. Cao, *General Modal Properties of Optical Resonances in Subwavelength Nonspherical Dielectric Structures*, Nano Letters **13**, 3559 (2013).

[112] G. Mie, *Beiträge zur Optik trüber Medien, speziell kolloidaler Metallösungen*, Annalen der Physik **330**, 377 (1908).

[113] U. Zywietz, M. K. Schmidt, A. B. Evlyukhin, C. Reinhardt, J. Aizpurua, and B. N. Chichkov, *Electromagnetic Resonances of Silicon Nanoparticle Dimers in the Visible*, ACS Photonics **2**, 913 (2015).

Summary

Optical metamaterials are materials built from sub-wavelength building blocks, and can be designed to have effective optical properties that are not found in natural materials. A much-studied class of metamaterials uses small noble-metal resonant structures as building blocks, which have a magneto-electric response. These metal structures, however, suffer from high Ohmic losses near the metal plasma frequency and only work for a limited bandwidth. Furthermore, operation in the visible or UV spectral range requires scaling down of the structures to dimensions which are impossible to experimentally realize using todays available fabrication techniques.

In this thesis, we consider a different approach, that circumvents these limitations, in which the effective refractive index of the metamaterial is controlled by the coupling of surface plasmon polaritons (SPPs) on thin metal-dielectric-metal (MDM) waveguides. In particular, we consider a polarization-independent geometry consisting of a hexagonal array of dielectric coaxial waveguides, embedded in metal. The dispersion of the metamaterial can be controlled by tuning the geometry of the individual coaxes and designing the coupling with neighboring coaxial waveguides. In this thesis we describe the fabrication process and determine the optical properties of such a three-dimensional coaxial plasmonic metamaterial.

In Chapter 2, we describe the many-step fabrication process of the coaxial metamaterial in full detail. The fabrication process is a combination of electron beam lithography, reactive ion etching, metal infilling and polishing of the surface using a focused ion beam. We demonstrate successful fabrication of Si and hydrogen silsesquioxane (HSQ) hollow cylinders embedded in either silver or gold. We realize cylinders with an outer diameter in the range of 100 nm to 1 μm, and various dielectric channel widths, of which the smallest was ~7 nm.

In Chapter 3 we explore the optical properties of the coaxial metamaterial, both theoretically and experimentally. We calculate the dispersion of a single coaxial plasmonic waveguide for different material and geometry choices, and we find that the dispersion is particularly sensitive to the dielectric channel width. With these

insights we design an optimal geometry for which a negative mode index can be achieved, consisting of Si cylinders with an outer diameter of 150–200 nm and a dielectric channel thickness of 10–30 nm, embedded in Ag. Furthermore, we study the coupling of the coaxial waveguides placed inside a hexagonal array. We find that the transmission spectrum changes at a ring-to-ring distance smaller than 75 nm, while the dispersion is significantly altered for distances smaller than 50 nm. To support our theoretical findings, we measure the Fabry-Pérot resonances inside a 100 nm thick metamaterial slab with cathodoluminescence spectroscopy.

In Chapter 4 we perform interferometry measurements on a coaxial metamaterial in the visible spectral range. We show that both the measured and numerically simulated data are consistent with a negative mode index in the range of λ =440–500 nm. Furthermore, we experimentally demonstrate that the metamaterial has a polarization independent optical response.

Chapter 5 demonstrates how the plasmonic coaxial structures can be used as nano-apertures to trap small particles. The strong confinement of light inside the coaxial structures results in large optical trapping forces and geometrically confined potential wells in the near fields of the coaxial apertures. We numerically investigate how the optical forces are influenced by the geometry of the apertures, and find that 10 nm diameter dielectric particles with $n = 2$ can be stably trapped at the surface of the apertures, using a transmitted power of only ~6 mW. Furthermore, we show that the trapping forces are very similar if Au is used instead of Ag. Arranging single apertures in a hexagonal array with a center-to-center distance of 300 nm leads to similar trapping characteristics as for single coaxes. We describe how the optical forces can be measured using an AFM, and demonstrate the first experimental results.

We investigate the geometrical resonances supported by hollow Si cylinders in Chapter 6. We show that introducing a gap in the center of a 100–250 nm outer diameter silicon cylinder results in relatively small deviations from the well known electric dipole (ED) and magnetic dipole (MD) resonances of solid cylinders. The nature of the MD mode is preserved up to gap widths as large as 190 nm for a wall thickness of just 40 nm. We fabricate hollow nanocylinders with an outer diameter in the range of 108–251 nm using electron beam lithography and reactive ion etching, and measure their cathodoluminescence and dark field scattering spectra. Furthermore, we systematically explore the trends of the scattering cross-section numerically by changing the cylinder geometry. The gap provides an interesting additional parameter to further tune the resonant wavelengths and the radiation pattern in the far field. We find good agreement between theory and experiment.

Overall, this thesis provides insight in the optical properties of coaxial plasmonic metamaterials, both theoretically and experimentally. We show that this metamaterial can be designed to have a negative refractive index in the visible spectral range and explore the use of coaxial plasmonic structures as optical traps for nanoscale particles.

Samenvatting

Optische metamaterialen zijn kunstmatige materialen opgebouwd uit elementen die typisch kleiner zijn dan de golflengte van licht. Deze materialen kunnen optische eigenschappen bezitten die niet bestaan in natuurlijke materialen. Vaak worden metamaterialen gemaakt uit bouwelementen bestaande uit kleine, resonante structuren van edelmetaal die interactie kunnen hebben met de electrische en magnetische componenten van licht. Voor toepassingen in het zichtbare gebied hebben deze metamaterialen echter een aantal beperkingen. Ten eerste worden ze in dit golflengtebereik gekenmerkt door hoge verliezen, en ten tweede is het bijna onmogelijk om deze resonante structuren te fabriceren op de vereiste nanometer schaal.

In dit proefschrift beschouwen we een alternatief metamateriaalontwerp, een zogenaamd plasmonisch metamateriaal, dat bestaat uit ultra-dunne lagen van afwisselend metaal en dielectrisch materiaal. De effectieve brekingsindex wordt in dit metamateriaal bepaald door de koppeling van oppervlaktegolven (plasmonen) die propageren op de grensvlakken van het metaal en dielectrisch materiaal. In dit proefschrift bestuderen we de optische eigenschappen van een driedimensionale geometrie die polarizatie-onafhankelijk is. Deze bestaat uit holle Si cylinders die zijn gerangschikt in een hexogenaal rooster, ingebed in metaal. De dispersie van dit metamateriaal kan worden gecontroleerd door de geometrie en de koppeling tussen de coaxiale lichtgeleiders aan te passen. In dit proefschrift laten we zien hoe dit metamateriaal kan worden gemaakt en bepalen we de optische eigenschappen.

In Hoofdstuk 2 beschrijven we het fabricageproces van het coaxiale metamateriaal in detail. Het proces is een combinatie van electronenbundellithografie, plasma-etsen, metaalinvulling en het polijsten van het oppervlak met een ionenbundel. We demonstreren hoe dit metamateriaal succesvol gerealiseerd kan worden met cylinders bestaande uit Si of waterstof silsesquioxane (HSQ), verzonken in goud of zilver. We hebben cylinders gemaakt met een buitendiameter variërend van 100 nm tot 1 μm en verschillende dielectrische kanaalbreedtes, de kleinste was slechts ~7 nm.

In Hoofdstuk 3 onderzoeken we de optische eigenschappen van het metamateriaal, zowel experimenteel als theoretisch. We berekenen de dispersie van een enkele plasmonische coaxiale lichtgeleider, waarbij de materialen en de dimensies worden gevarieerd. Hieruit concluderen we dat de dispersie met name erg gevoelig is voor de dielectrische kanaalbreedte. Met de verkregen inzichten ontwerpen we een geometrie die een negative mode index kan hebben. Deze geometrie bestaat uit Si cylinders met een buitendiameter van 150–200 nm en een kanaalbreedte van 10–30 nm en is verzonken in Ag. Ook bestuderen we koppeling tussen de coaxiale lichtgeleiders die in een hexagonaal rooster zijn gerangschikt. Hierbij vinden we dat het transmissiespectrum verandert voor ring-tot-ring-afstanden van minder dan 75 nm, terwijl de dispersie significant gaat afwijken voor afstanden kleiner dan 50 nm. Om deze bevindingen te ondersteunen, meten we de Fabry-Pérot resonanties in een 100 nm dik metamateriaal met cathodoluminiscentiespectroscopie.

Hoofdstuk 4 beschrijft optische interferometriemetingen op een coaxiaal plasmonisch metamateriaal in het zichtbare spectrale gebied. We laten zien dat zowel de gemeten als gesimuleerde data consistent zijn met een negatieve mode-index in het golflengtegebied λ =440–500 nm. Ook bewijzen we experimenteel dat het metamateriaal zich polarizatie-onafhankelijk gedraagt.

Hoofdstuk 5 laat zien hoe de plasmonische-nanoaperturen in het metamateriaal gebruikt kunnen worden om door middel van de lichtkracht kleine deeltjes vast te houden. De opsluiting van het licht in het kleine gebied binnen in de coaxen resulteert in grote optische krachten en geometrisch kleine potentiaalputten in het nabije-veld van de aperturen. We onderzoeken numeriek hoe de optische krachten afhankelijk zijn van de coaxgeometrie en vinden dat nanodeeltjes met een diameter van 10 nm en een brekingsindex van $n = 2$ stabiel kunnen worden vastgehouden met een laserpower van slechts ~6 mW. Ook laten we zien dat de optische krachten nauwelijks veranderen als Au gebruikt wordt in plaats van Ag. Het plaatsen van de aperturen in een rooster heeft ook slechts een kleine invloed op de lichtkracht. We beschrijven hoe de optische krachten kunnen worden gemeten met een AFM, en laten de eerste experimentele resultaten zien.

In Hoofdstuk 6 bestuderen we de geometrische resonanties van holle Si cylinders. We laten zien dat het introduceren van een gat in het midden van een Si cylinder met een buitendiameter van 100–250 nm slechts een kleine invloed heeft op de electrische dipool (ED) en magnetische dipool (MD) modes zoals die bekend zijn in Si cylinders zonder gat. We vinden dat de MD mode kan bestaan tot een gatdiameter van 190 nm, wat overeenkomt met een Si wanddikte van slechts 40 nm. We fabriceren holle nanocylinders met een buitendiameter van 108–251 nm, waarbij we gebruik maken van electronenbundellithografie en plasma-etsen. Het spectrum van de gefabriceerde deeltjes is gemeten met cathodoluminescentie- en donkereveldspectroscopie. Verder onderzoeken we op systematische wijze de trends van de verstrooiingsdoorsnede voor verschillende cylindergeometrieën. De gatgrootte is een interessante aanvullende parameter waarmee de resonantiespectra, en het stralingspatroon in het verre veld, kunnen worden gecontroleerd. We

vinden goede overeenkomsten tussen theorie en de experimenten.

Samenvattend geeft dit proefschrift inzicht in de optische eigenschappen van coaxiale plasmonische metamaterialen op een experimentele en theoretische wijze. We laten zien dat dit metamateriaal zo kan worden ontworpen dat het een negative brekingsindex heeft. We exploreren het gebruik van de plasmonische structuren als optisch pincet waarmee nanoschaaldeeltjes kunnen worden gevangen.

List of publications

This thesis is based on the following publications:

- *Fabrication process of a coaxial plasmonic metamaterial*, M. A. van de Haar, and A. Polman, submitted. **(Chapter 2)**
- *Surface plasmon polariton modes in coaxial metal-dielectric-metal waveguides*, M. A. van de Haar, B. J. M. Brenny, R. Maas, and A. Polman, submitted. **(Chapter 3)**
- *Experimental realization of a polarization-independent ultraviolet/visible coaxial plasmonic metamaterial*, M. A. van de Haar, R. Maas, H, Schokker, and A. Polman, Nano Letters **14**, 6356 (2014), ACS Editors' Choice. **(Chapter 4)**
- *Controlling magnetic and electric dipole modes in hollow silicon nanocylinders*, M. A. van de Haar, J. van de Groep, B. J. M. Brenny, and A. Polman, submitted. **(Chapter 6)**

Other publications by the author:

- *Isochoric ideality in jammed random packings of non-spherical granular matter*, A. V. Kyrylyuk, M. A. van de Haar, L. Rossi, A. Wouterse, A. P. . Philipse, Soft Matter **7**, 1671 (2008).
- *Ubiquity of optical activity in planar metamaterial scatterers*, I. Šersić, M.A. van de Haar, F. Bernal Arango and A.F. Koenderink, Physical Review Letters **108**, 223903 (2012).

Acknowledgements

De afgelopen vier jaar heb ik ontzettend veel geleerd op wetenschappelijk en persoonlijk vlak, wat uiteindelijk tot dit proefschrift heeft geleid. Graag wil ik iedereen bedanken die hieraan heeft bijgedragen. Een aantal mensen hiervan wil ik graag hieronder in het bijzonder noemen.

Albert, graag wil ik je bedanken voor je begeleiding de afgelopen jaren. Mede door jouw enthousiaste en heldere manier van presenteren heb je me tijdens mijn studie in Utrecht geinteresseerd voor de nanofotonica. Ik weet nog dat ik tijdens het eerste college over metamaterialen al zo gefascineerd was door de onwerkelijke eigenschappen ervan dat ik meteen hoopte dat, mocht ik een promotie-onderzoek gaan doen, dit het onderwerp zou zijn. Ik ben heel blij dat je me de kans hebt gegeven hier vier jaar aan te werken. Bovendien ben ik je dankbaar dat je altijd met veel aandacht en precizie de stukken hebt gelezen en verbeterd die ik geschreven heb. Dit heeft zeker een enorme verbetering van de kwaliteit opgeleverd en ik heb er veel van geleerd.

I have always enjoyed working in the Photonic Materials group due to the unique combination of a great atmosphere and a very high productivity. I would like to thank all the (former) group members for their help, discussions and good times. Toon, Piero, Mark, Jorik, Lourens, Phillip and Verena, it was great to share an office with you. Thanks for being my klaagmuur during (especially) the last part of the writing process. I should specifically mention Jorik for that, it was very bonding to finalize our theses during the same period. Ik wil je ook graag bedanken voor al je nuttige commentaar en hulp. Hopelijk word je snel professor. Mark, ik hoop dat je het leuk vond alle verhalen over Berta te horen en samen je Nederlands te oefenen. Ruben, ik heb altijd met veel plezier samen aan de metamaterialen gewerkt. Bedankt voor al je hulp. Benjamin, bedankt voor je CL-hulp en al je aanbiedingen voor eten. Vooral als ik tot laat aan het werk was, was het heel fijn dat ik altijd je voorraadla mocht plunderen. Claire and Bonna, it was great to get to know you better when we shared a hotel room during our trips. Rutger, James, Hugo, Julia, Bas, Philip and Theresa thanks for all the useful discussions during group meetings or any other time. Since the Photonic Materials group is part of

the Center of Nanophotonics, I would like to thank everyone from the Center of Nanophotonics for their input.

Tijdens mijn promotie heb ik een tijd lang min of meer in de cleanroom gewoond. Uiteindelijk ben ik weer naar buiten gekomen met hele mooie structuren, maar dat is natuurlijk niet vanzelf gegaan. Graag wil ik iedereen van het Amsterdam Nanocenter bedanken voor alle hulp en technische ondersteuning. Hans, Dimitry, Andries, Johan, Peter en Gijs, bedankt dat jullie altijd meteen kwamen helpen als ik weer eens een probleem had (veroorzaakt). Ik heb altijd met veel plezier in de cleanroom gewerkt en daar hebben jullie zeker een bijdrage aan gehad.

Chapter 5 of this thesis is the result of a collaboration with the group of Jennifer Dionne from Stanford. Jen, Amr and Yang, thank you for the good collaboration. I especially enjoyed my time at Stanford. Thanks for making me feel very welcome.

Natuurlijk is het doel van een promotie-onderzoek om aan het eind een mooie thesis als resultaat te hebben. Echter, ik denk dat een grote bijdrage daarvan te danken is aan mensen die niet op wetenschappelijk, maar op sociaal gebied er voor hebben gezorgd dat ik op AMOLF een goede tijd heb gehad. Hinke, het was altijd gezellig om lekker over paarden te praten en de facebookpagina van Mark of BB vol te spammen. Ik hoop dat zij het net zo leuk vonden. Marko Kamp, ik vond het altijd leuk samen koffie te drinken en lekker over het uitlijnen van lasers te praten. Het schept echt een band dat we op dezelfde dag begonnen zijn op Amolf. Sorry dat je soms tweede keus was. Frans, ook met jou was het altijd leuk om koffie te drinken of even te praten. Ik vind het jammer dat je van Amolf weg bent. Freddy, al sinds onze studie hebben we veel samengewerkt. Dit was zo bonding dat we nog steeds veel contact hebben en regelmatig roddelupdates naar elkaar sturen. Helaas sta je niet bij de wetenschappelijke hulp omdat het project dat we samen hebben gedaan heeft gefaald. Ik hoop dat je snel professor wordt, niet alleen omdat je beloofd hebt me dan een baan aan te bieden waarbij ik mag paardrijden wanneer ik wil, maar ook omdat u best promising bent. Graag wil ik ook de electronica en software afdeling bedanken dat jullie me getolereerd hebben tijdens jullie zeer exclusieve lunchwandelingen en koffiepauzes. Hopelijk heeft Ronald jullie hier niet teveel voor bedreigd.

Een groot deel van mijn tijd op Amolf ben ik fanatiek geweest als lid van de personeelsvereniging. Ik vond het erg leuk om na te denken over leuke activiteiten en ze samen te organiseren. Bedankt voor de samenwerking.

Ook buiten Amolf heb ik veel ondersteuning gehad van verschillende mensen. Graag wil ik Annemarie en Gelske noemen, er is geen betere manier om bij te komen van de werkweek dan met elkaar paard te rijden op Ameland! Ik kijk altijd heel erg uit naar alles wat we samen plannen. Ik hoop dat nu het proefschrift af is we weer vaker leuke dingen kunnen doen.

Tijdens mijn studie en promotie heb ik ook altijd veel steun gehad van mijn ouders en broertjes Joris en Sander. Ik vind het leuk dat jullie altijd geinteresseerd

zijn in het onderzoek wat ik doe, ik hoop dat ik het enigszins heb kunnen uitleggen. Joris, mocht je ook gaan promoveren dan hoop ik dat ik ook in jouw dankwoord kom. Ik kijk er naar uit om een doctor dokter als broertje te hebben. Sander, ik vond het leuk dat je ook op Amolf was voor je stages. Een beetje leven in de brouwerij kan nooit kwaad.

Als laatste wil ik graag mijn lieve vriend Ronald bedanken. Bedankt voor je steun in vooral het laatste deel van mijn promotie toen ik het erg druk had. Het was fijn dat ik toch elke dag wat te eten had als ik laat thuis kwam. Ik kijk er naar uit samen nog veel leuke dingen te doen!

About the author

Marie Anne van de Haar was born in Amsterdam, The Netherlands, on January 19, 1988. After receiving her high school diploma from the Christelijk College Groevenbeek in Ermelo in 2006, she studied chemistry and Physics at Utrecht University. She graduated cum laude in 2011, with a thesis on Eu-doped CdSe quantum dots, supervised by prof. dr. Andries Meijerink. After a four-month internship on measuring the optical response of split-ring resonators in the Resonant Nanophotonics group of prof. dr. Femius Koenderink at the FOM Institute AMOLF in Amsterdam, she started as PhD student in the Photonic Materials group of prof. dr. Albert Polman at AMOLF in 2011, of which the results are shown in this thesis. During her PhD, she spent 1 month at Stanford University in the group of prof. dr. Jennifer Dionne, working on optical trapping measurements. In her free time, Marie Anne enjoys horseback riding at the beach of Ameland or on her horse Berta.

The work described in this thesis was performed at the FOM-Institute AMOLF, Science Park 104, 1098 XG Amsterdam, The Netherlands.